

12-2014

The Role of Quantum Dot Size on the Performance of Intermediate Band Solar Cells

Najla Alnami
University of Arkansas, Fayetteville

Follow this and additional works at: <https://scholarworks.uark.edu/etd>



Part of the [Electrical and Electronics Commons](#), [Power and Energy Commons](#), and the [Quantum Physics Commons](#)

Citation

Alnami, N. (2014). The Role of Quantum Dot Size on the Performance of Intermediate Band Solar Cells. *Graduate Theses and Dissertations* Retrieved from <https://scholarworks.uark.edu/etd/2040>

This Thesis is brought to you for free and open access by ScholarWorks@UARK. It has been accepted for inclusion in Graduate Theses and Dissertations by an authorized administrator of ScholarWorks@UARK. For more information, please contact scholar@uark.edu.

The Role of Quantum Dot Size on the Performance of Intermediate Band Solar Cells

The Role of Quantum Dot Size on the Performance of Intermediate Band Solar Cells

A thesis submitted in partial fulfillment
of the requirements for the degree of
Master of Science in Microelectronics-Photonics

By

Najla Alnami
University of Jazan
Bachelor of Science in Physics, 2008

December 2014
University of Arkansas

This thesis is approved for recommendation to the Graduate Council.

Dr. Gregory Salamo
Thesis Director

Dr. Shui-Qing Yu
Committee Member

Dr. Morgan Ware
Committee Member

Dr. Vasyi Kunets
Ex-Officio Member

Prof. Ken Vickers
Ex-Officio Member

The following signatories attest that all software used in this thesis was legally licensed for use by Najla Alnami for research purposes and publication.

Ms. Najla Alnami, Student

Dr. Gregory Salamo, Thesis Director

This thesis was submitted to <http://www.turnitin.com> for plagiarism review by the TurnItIn company's software. The signatories have examined the report on this thesis that was returned by TurnItIn and attest that, in their opinion, the items highlighted by the software are incidental to common usage and are not plagiarized material.

Dr. Rick Wise, Program Director

Dr. Gregory Salamo, Thesis Director

Abstract

The goal of this thesis is to understand possible mechanisms for the reported decrease of the open circuit voltage and solar cell efficiency in quantum dot (QD) intermediate band solar cells (IBSCs). More specifically, the effect of indium arsenide (InAs) QD height on the open circuit voltage and solar cell efficiency was studied in a systematic way. To explore this effect in QD solar cells, several solar cells (SCs) were grown with varying InAs QD heights. All experimental characteristics of the QD solar cells were compared to a reference structure without QDs. All samples were grown by Molecular Beam Epitaxy (MBE), and self-assembled InAs QDs were formed using the Stranski-Krastanov (SK) growth method. Using a QD truncation technique, the height of the QDs was accurately varied between 2 nm and 5 nm, while maintaining both lateral size and areal density of the QDs. The intermediate band (IB) of each solar cell was constructed from 10 layers of InAs QDs of the same size and density.

All samples were fabricated as solar cell devices using standard optical photolithography, for electrical characterization and solar cell efficiency studies. Optical and structural characterization was done for all samples. The following characterizations were performed: Transmission Electron Microscopy (TEM), Low Temperature Photoluminescence (PL), Power Dependent PL, External Quantum Efficiency (EQE), Temperature Dependent Solar Power Conversion Efficiency, and Current-Voltage measurements. The efficiency measurements demonstrate the critical role of QD size on the performance of QD IBSCs. The EQE measurement indicates a change in the position of the band edge, due to carrier confinement, consistent with a QD size variation as verified by TEM and PL. Measurements demonstrate that the EQE in the NIR range of the spectrum is enhanced in the QD IBSCs devices due to light absorption by the QDs. This work also demonstrates that open circuit voltage (V_{oc}) decreases

with an increase of the QD height, which leads to significant degradation of the solar cell conversion efficiency for QD sizes above 3 nm. In addition, for samples with QD heights of 4 nm and above, the EQE spectra in the GaAs region decreases, indicating a loss of photocurrent, most likely due to traps introduced by the large QDs. These experimental results suggest that the open circuit voltage in QD IBSCs degrades with the increase of QD height as a result of (i) a decrease of the effective band gap of the absorber media and (ii) enhanced Shockley-Read-Hall recombination in the presence of traps in the solar cell space charge region.

Acknowledgments

First, I wish to express profound gratitude to my God for giving me life and a curious mind that longs to explore and discover new and deeper truths. It is He who precisely orchestrated each step leading to my accomplishment of this feat, as well as the timely (often uncanny) appearance of each individual who supported me along this journey.

I extend a heartfelt thanks to my parents, my mother Mrs. Badriah Khawajy and my father Mr. Ahmed Alnami Alsaied, for their constant prayers and meditation on my behalf. Making them proud was my primary inspiration for attending graduate school in America as preparation for becoming a teaching faculty member at Jazan University.

I gratefully acknowledge my devoted husband, Mr. Mahfod Alnami, and my young children, Amnah Alnami and Yazan Alnami, who moved with me many thousands of miles for this extended adventure in a foreign country. They have shown patience and support beyond comprehension during a demanding sojourn when I was often away from home attempting to accomplish my work on the university campus—sometimes for 35 hours continuously. I fondly remember my husband calling me daily to inquire about my progress and habitually staying awake the entire night to make sure I arrived home safely. My children would constantly ask and wait, anxious for the time when I would return home. This, in turn, motivated me to work harder and faster so that I might see them before they fell asleep.

I wish to express my special thanks to Dr. Gregory Salamo, my distinguished research advisor, who taught me Physics comprehension on a deep level, often via one-on-one discussion. I am so thankful to him for giving me the opportunity to work with all the great facilities he developed. Thank you Dr. Salamo for all of your encouragements and motivations to work hard

and thoroughly on research. Dr. Gregory Salamo, you have perpetually bolstered my confidence and urged me to dig deeper and push harder to reach my goal. *“You are smart! You can do this in short order!”* he would say.

My special thanks goes to Dr. Vasyl Kunets, my research mentor, for patiently training me to operate sophisticated laboratory equipment in order to best perform my research experiments. Dr. Kunets gave me a better grasp on the underlying principles of physics required for this research and to master data analysis. Furthermore, he expanded my comfort zone with fabrication and electrical characterization, and personally helped refine my presentation skills.

I am deeply grateful to my program director, Professor Ken Vickers, for accepting me into the Microelectronics-Photonics program. On several occasions, he reserved precious time to listen intently to problems I was experiencing. He worked with me each time to resolve the issue at hand, spurring my determination to surpass my personal best. *“Be strong. Project your ideas out loud. Say them LOUDLY!”* he would say. Also, I am thankful for the new Micro EP program director, Dr. Rick Wise, who spent time editing this thesis and giving comments and suggestions. I am also grateful to Renee Hearon, our devoted department secretary, who has always been diligent about informing me of any deadlines and documentation submissions needed for MicroEP.

My appreciation goes out to my devoted colleagues, Yusuke Hirono, Sabina Koukourinkova, Colin Furrow, and Xian Hu, who gave me invaluable assistance in training me to operate complex equipment and who joined together with me in many riveting discussions.

Many thanks to Dr. Vitaliy Dorogan, Dr. Yuriy Mazur and Dr. Morgan Ware for helping me in making PL measurements. Similarly, thanks to Xian Hu and Dr. Mourad Benamara, who assisted in TEM measurement.

I'd like to thank each of my faithful committee members who eagerly joined in the research: Dr. Gregory Salamo, Dr. Morgan Ware, Dr. Vasyl Kunets, and Dr. Fisher Yu. The collective efforts and collaboration of all the aforementioned speaks to each individual's passion for our work and their desire to see me succeed.

Thanks to all the men and women who work so hard to help the students, faculty, and employees at the University of Arkansas and its students achieve success. I was away from my home country for three years fulfilling my dream to conduct scientific research in unrivaled facilities, like those available at the University of Arkansas. The opportunities available to me while working on my degree in the Institute for Nano Science and Engineering exceeded my highest expectations. In addition, I was fortunate to experience interaction with eminent program faculty and peers across diverse majors, with whom I enjoyed compelling communication due to their desire to exchange knowledge.

Finally, I find it difficult to express adequate thanks to the faculty and members of Jazan University and the King Abdullah Scholarship program, my program sponsor, for providing the generous financial support that allowed me to face the challenges of this endeavor and see this dream come to fruition. I am forever grateful.

Dedication

I dedicate this dissertation to my parents, Ahmed Alnami and Badriah Khawajy, to my husband, Mahfod Alnami, to my children, Amnah Alnami and Yazan Alnami, and to my brothers and sisters. I appreciate their respect and acceptance of my decision in becoming a scientist and studying in the U.S.A., far away from my country. Also, I appreciate their continuous support.

Table of Contents

Chapter 1:	Introduction.....	1
Chapter 2:	Theoretical Background.....	6
2.1.	Brief Introduction to Semiconductor Physics	6
2.1.1.	Semiconductor Materials	6
2.1.2.	Fermi-Dirac Distribution (E_F).....	9
2.1.3.	Generation and Recombination.....	11
2.1.4.	p-n Junction.....	13
2.2.	Photovoltaics.....	15
2.2.1.	The Solar Spectrum.....	15
2.2.2.	Basic Principle of Solar Cells	16
2.2.3.	Limits of Photovoltaic Conversion-Efficiency	18
2.2.4.	Strategies to Increase Efficiency.....	21
2.3.	Intermediate Band Solar Cell (IBSC)	21
2.3.1.	High Efficiency Conversion Limit.....	21
2.3.2.	The Basic Concept of IBSC	23
2.4.	IBSC Devices.....	24
2.4.1.	IBSC Material Selection	24
2.4.2.	IBSC Materials.....	27
2.4.3.	Current QD IBSCs Performance.....	28
2.4.4.	Suggestions for IBSCs improvement.....	29
Chapter 3:	Experimental Techniques.....	31
3.1.	Growth of QD IBSC devices	31

3.1.1.	Molecular Beam Epitaxy (MBE)	31
3.1.2.	QD Fabrication.....	33
3.2.	Fabrication of QD IBSC device	38
3.2.1.	Optical Photolithography	38
3.2.2.	Metal-Semiconductor Contacts.....	39
3.2.3.	Fabrication Details	41
3.3.	Characterization	47
3.3.1.	Material and Structural Characterization	47
3.3.2.	Optical Characterization	51
3.3.3.	Solar Cell Efficiency Studies	53
3.3.4.	Electrical Characterization.....	61
Chapter 4:	Results and Discussion	64
4.1.	Material and Structural Characterization (Cross-Sectional TEM).....	64
4.2.	Optical Characterization	67
4.3.	Efficiency Studies	74
4.3.1.	External Quantum Efficiency (EQE)	74
4.3.2.	Solar Cell Efficiency.....	87
Chapter 5:	Conclusion and Future Work	98
References	101
Appendix A:	Description of Research for Popular Publication.....	109
Appendix B:	Executive Summary of Newly Created Intellectual Property	111
Appendix C:	Potential Patent and Commercialization Aspects of Listed Intellectual Property Items.....	112

C.1 Patentability of Intellectual Property	112
C.2 Commercialization Prospects	113
C.3 Possible Prior Disclosure of IP	113
Appendix D: Broader Impact of Research	114
D.1 Applicability of Research Methods to Other Problems	114
D.2 Impact of Research Results on U.S. and Global Society	114
D.3 Impact of Research Results on the Environment	114
Appendix E: Microsoft Project for MS MicroEP Degree Plan	115
Appendix F: Identification of All Software Used in Research and Thesis Generation	124
Appendix G: All Publications Published, Submitted and Planned	126

List of Figures

Figure 1. Efficiency versus cost for three generations of solar cells [4].....	2
Figure 2. A schematic graph showing I_{sc} increase and V_{oc} decrease in the IBSCs compared to reference p-i-n SCs.	4
Figure 3. A schematic of energy bands of metal, semiconductor, and insulator [18].	7
Figure 4. A schematic diagram of direct and indirect semiconductors [23].	9
Figure 5. A schematic diagram of Fermi level position in n-type and p-type materials.....	10
Figure 6. A schematic of Shockley-Read-Hall (SRH), Radiative, and Auger recombination mechanisms.....	13
Figure 7. p-n junction in thermal equilibrium and under illumination.	14
Figure 8. The solar spectra irradiance of AM0, AM1.5g and 1.5 d [28].	16
Figure 9. A schematic diagram of a solar cell (bulb photo [30])......	17
Figure 10. The maximum theoretical efficiencies under AM 1.5 illumination versus bandgap energy [31]......	18
Figure 11. Solar efficiency conversion factors: shading, reflectance, and absorber layer limited thickness.....	19
Figure 12. Thermalization and energy loss in solar cells.....	20
Figure 13. Efficiency limit for an intermediate band solar cell, a two terminal-tandem solar cell, and a single gap solar cell [37].	22
Figure 14. A schematic band diagram of IBSC. E_g is the fundamental bandgap, E_L and E_H the sub-bandgaps, adopted from [42].	24
Figure 15. A schematic diagram of MBE chamber.	31
Figure 16. Riber 32P MBE chamber at the University of Arkansas Nano Facility.....	32

Figure 17. A schematic diagram of QD formation using SK Growth method.	34
Figure 18. The QD IBSC solar cell and the p-i-n reference solar structures.	35
Figure 19. The process of quantum dot truncation.	37
Figure 20. (a) The metal-semiconductor contact in thermal equilibrium. (b) Ohmic metal-semiconductor contact with positive voltage at the metal, adopted from [21].	40
Figure 21. An SEM image for a typical solar cell structure.	41
Figure 22. A schematic diagrams illustrating detailed photolithography processes used for solar cell structure fabrication.	46
Figure 23. A schematic diagram of the AFM tapping mode operation [72].	49
Figure 24. FEI Titan 80-300TEM instrument used in this research.	50
Figure 25. A schematic diagram of the experimental setup for PL measurement, modified from [79].	52
Figure 26. The ideal external quantum efficiency curve and the mechanisms behind EQE reduction [84].	54
Figure 27. A schematic diagram of the optical setup of the EQE system.	55
Figure 28. QEX10 Quantum Efficiency Measurement System, Inc.	57
Figure 29. A schematic graph of solar I-V characteristics, showing diode dark current and the increase of diode current under illumination.	59
Figure 30. A schematic diagram of the solar efficiency measurement setup.	60
Figure 31. The PV Measurements Small Area Solar Simulator.	61
Figure 32. Current-Voltage measurement setup.	63
Figure 33. a) TEM image of a single InAs quantum dot for sample SF7 (7 nm GaAs cap) b) TEM image of the entire QD IBSC growth structure QDs.	64

Figure 34. TEM image of sample SF5 with 5 nm coverage showing the 10 layers of QDs.	65
Figure 35. TEM images for (a) SF2 sample with 2 nm coverage, (b) SF3 sample with 3 nm coverage, (c) SF4 sample with 4 nm coverage, (d) SF5 sample with 5 nm coverage, and (e) SF7 sample with 7 nm coverage.....	66
Figure 36. Normalized PL spectra of 2 nm, 3 nm, 4 nm, 5nm, and 7 nm GaAs cap QD IBSCs samples.....	68
Figure 37. PL spectra for different excitation intensities measured at 10 K for sample SF2.	70
Figure 38. PL spectra for different excitation intensities measured at 10 K for sample SF3.	70
Figure 39. PL spectra for different excitation intensities measured at 10 K for sample SF4.	71
Figure 40. PL spectra for different excitation intensities measured at 10 K for sample SF5.	71
Figure 41. PL spectra for different excitation intensities measured at 10 K for sample SF7.	72
Figure 42. PL spectra of 2 nm, 3 nm , 4 nm, 5nm, and 7 nm GaAs cap QD IBSCs samples at low power intensity of 1 mW/cm ²	73
Figure 43. EQE versus incident photon energy for all samples.....	74
Figure 44. The decrease of EQE spectra in the GaAs region, indicating a loss of photocurrent at photon energy = 1.8 eV.....	76
Figure 45. EQE spectrum measured at 300 K (the black line) and the first derivative analysis for sample SF2 (the red line).	77
Figure 46. EQE spectrum measured at 300 K (the black line) and the first derivative analysis for sample SF3 (the red line).	78
Figure 47. EQE spectrum measured at 300 K (the black line) and the first derivative analysis for sample SF4 (the red line).	79

Figure 48. EQE spectrum measured at 300 K (the black line) and the first derivative analysis for sample SF5 (the red line).	80
Figure 49. EQE spectrum measured at 300 K (the black line) and the first derivative analysis for sample SF7 (the red line).	81
Figure 50. Calculated GaAs band gap and experimental data of GaAs band gap for the reference (SF0), smallest QD (SF2), and largest QD (SF5) samples plotted as a function of temperature (81-300 K).	85
Figure 51. Current-Voltage measurements of all samples under illumination of AM1.5 standard (100mW/cm ²) at 300 K.	88
Figure 52. Open circuit voltage and efficiency as a function of QD height for all samples at 300 K.	89
Figure 53. Efficiency as a function of temperature for all samples.	92
Figure 54. Open circuit voltage and short circuit current as a function of temperature for reference, 3 nm QD, 4 nm QD samples.	92

List of Table

Table 1. Materials used to fabricate IB. Modified from [16].....	27
Table 2. Detailed steps for fabrication of the solar cell device.....	44
Table 3. Summary of the AFM probe parameters.	49
Table 4. Targeted and achieved quantum dot heights.....	67
Table 5. Energies measured for the emission of PL representing QD excited states for all the QD samples.....	82
Table 6. Energies measured for the optical transition in EQE representing QD excited states for all the QD samples.....	82
Table 7. Spacing between the energies measured for the emission of PL representing QD excited states for all the QD samples.	83
Table 8. Spacing between the optical transitions of the EQE of photon energies below 1.33 eV, representing QD excited states, for all the QD samples.	83
Table 9. Parameters used in the GaAs and InAs bandgap at variable temperatures using Varshni model.....	85
Table 10. The open circuit voltage (V_{oc}), short circuit current (I_{sc}), solar cell maximum power (P_{max}) values, filling factor (FF), and efficiency at variable temperatures for the reference sample (SF0).	93
Table 11. The open circuit voltage (V_{oc}), short circuit current (I_{sc}), solar cell maximum power (P_{max}) values, filling factor (FF), and efficiency at variable temperatures for the 2.5 nm sample (SF2).	93

Table 12. The open circuit voltage (V_{oc}), short circuit current (I_{sc}), solar cell maximum power (P_{max}) values, filling factor (FF), and efficiency at variable temperatures for the 3.1 nm sample (SF3).	94
Table 13. The open circuit voltage (V_{oc}), short circuit current (I_{sc}), solar cell maximum power (P_{max}) values, filling factor (FF), and efficiency at variable temperatures for the 4.3 nm sample (SF4).	94
Table 14. The open circuit voltage (V_{oc}), short circuit current (I_{sc}), solar cell maximum power (P_{max}) values, filling factor (FF), and efficiency at variable temperatures for the 5.1 nm sample (SF5).	95
Table 15. The open circuit voltage (V_{oc}), short circuit current (I_{sc}), solar cell maximum power (P_{max}) values, filling factor (FF), and efficiency at variable temperatures for the 5.3 nm sample (SF7).	95
Table 16 Intermediate band solar cell experimental recorders of the efficiency and open circuit voltage compared with the results of this research.	96

List of Symbols

A_{cell}	Solar Cell Active Area
E	Energy
E_f	Fermi Level
eV	Electron Volt
FF	Filling Factor
f	Probability of Finding Electrons
h	Planck Constant
I_{sc}	Short Circuit Current
I_{max}	Maximum Generated Current
I_{test}	Current of the Tested Solar Cell
I_{cal}	Current of the Calibrated Silicon Photodiode
J_d	Dark Current Density
J_0	Saturation Current Density
J_L	Current Density under illumination
\vec{k}	Wave Vector
k	Boltzmann's Constant
n	Ideality Factor
η	Solar Cell Efficiency

P_{out}	Maximum Power of the Solar Cell
P_{in}	Incident Power on the Solar Cell
QE_{test}	Quantum Efficiency of the Tested Solar Cell
QE_{cal}	Quantum Efficiency of the Calibrated Silicon Photodiode
R_s	Series Resistance
T	Temperature
V_{oc}	Open Circuit Voltage
V_{max}	Maximum Generated Voltage
V_t	Thermal Voltage
v	Velocity

List of Abbreviations and Acronyms

2D	Two Dimensional
3D	Three Dimensional
AFM	Atomic Force Microscopy
Al	Aluminum
AlGaAs	Aluminum Gallium Arsenide
AM	Air Mass
AM1.5 d	Air Mass 1.5 Direct
AM1.5 g	Air Mass 1.5 Global
As	Arsenic
Au	Gold
AuZn	Gold Zinc
AuGe	Gold Germanium
Be	Beryllium
BSF	Back Surface Field
CB	Conduction Band
CdTe	Cadmium Telluride
CuGaS ₂	Copper Gallium Sulfide
Cr	Chromium

E_G	Band Gap Energy
E_H	Energy between the Valence Band and Intermediate Band
E_L	Energy between the Intermediate Band and Conduction Band
EQE	External Quantum Efficiency
e-h	Electron-Hole
Fe	Iron
Ga	Gallium
Ge	Germanium
GaAs	Gallium Arsenide
GaN	Gallium nitride
GaP	Gallium phosphide
GaSb	Gallium antimonide
GR	Generation-Recombination
HMA	Highly Mismatched Semiconductors Alloys
HCl	Hydrochloric Acid
IBSC	Intermediate Band Solar Cell
IB	Intermediate Band
IQE	Internal Quantum Efficiency
I-V	Current-Voltage

In	Indium
InAs	Indium Arsenide
InGaAs	Indium Gallium Arsenide
IPA	Isopropyl Alcohol
K	Kelvin
MBE	Molecular Beam Epitaxy
ML	Monolayer
Mn	Manganese
Ni	Nickel
P	Phosphorus
Pt	Platinum
PL	Photoluminescence
QD	Quantum Dot
QE	Quantum Efficiency
QFL	Quasi Fermi Level
RHEED	Reflection High Energy Electron Diffraction
SEM	Scanning Electron Microscopy
SC	Solar Cell
Si	Silicon

Sn	Tin
SK	Stranski-Krastanov
SRH	Shockley-Read-Hall Recombination
TEM	Transmission Electron Microscopy
Ti	Titanium
UHV	Ultra-High Vacuum
UV	Ultraviolet
VB	Valance Band
V	Volts
X-TEM	Cross-Sectional Transmission Electron Microscopy

Chapter 1: Introduction

Today, solar radiation is widely considered to be a virtually inexhaustible source of energy among the scientific community. The worldwide daily commercial and industrial consumption from conventional energy sources (hydro-electric, nuclear, etc.) is dwarfed by the total daily output of solar radiation. This makes solar energy one of the most promising of the non-conventional energy sources. Solar energy has been harnessed for countless practical applications, such as: photo-voltaic cells, water heating systems, solar air conditioning, food dryers, and even automobiles. Hypothetically, properly harnessed solar energy could supply all present and future energy needs of the entire world on a continuous basis.

However, for solar cells, the conversion efficiency needs to be enhanced in order to be competitive with conventional energy sources. Developing a commercially viable solar cell (SC) system with improved performance is essential to being a cost-effective alternative to today's conventional technologies for particular applications. Currently, the solar cell community is aiming to increase the solar cell efficiency, while preserving the economic cost. Achieving the first goal of increasing the efficiency of the solar cells contributes to the second goal of lowering the cost of solar cells. The higher the solar cell efficiency, the smaller the area required to generate a certain power, thereby lowering the cost required. Solar cells with efficiencies of 30 percent or higher can considerably reduce solar cell costs by lowering the price per watt. To have a cost-effective solar cell, improvement of the solar efficiency should exceed the Shockley-Queisser single-band gap solar cell efficiency limit [1], [2], [3]. Such improvement can be achieved through the use of advanced third generation solar cells which are promising solar cells for increased efficiency and lower cost (Figure 1) [4].

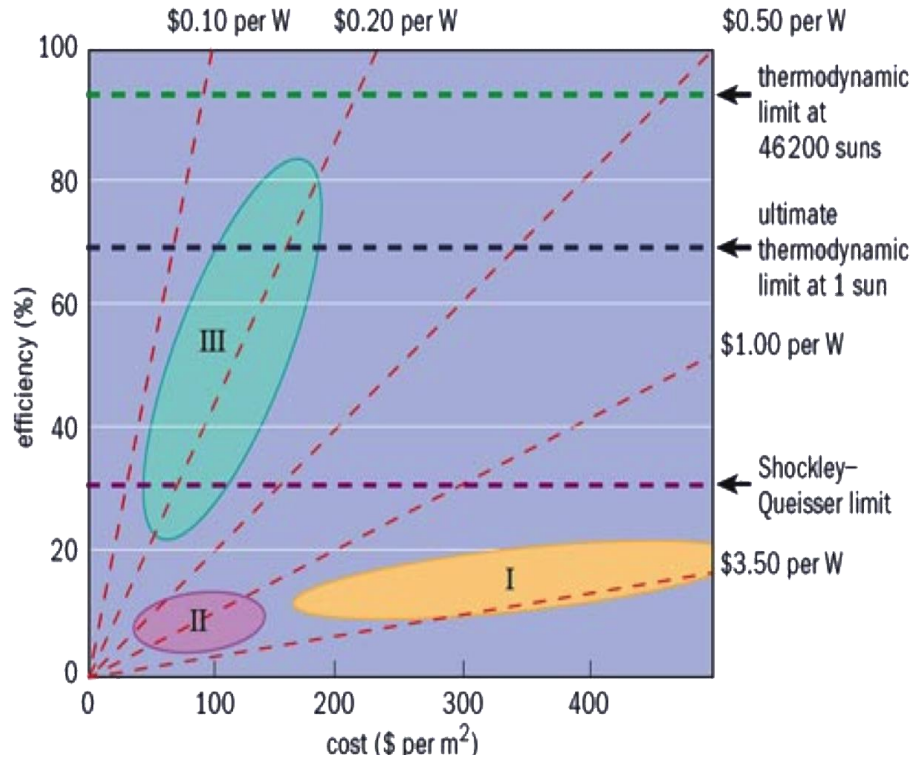


Figure 1. Efficiency versus cost for three generations of solar cells [4].

Even though theoretical calculations have shown high efficiencies for the third generation solar cells, in practice, many limitations affect the efficiency-conversion of the solar cell devices. One of the main limitations is that low energy photons cannot excite charge carriers to the conduction band (CB) of the material. Thus, these photons do not contribute to the photocurrent of the device. To address this and similar issues, the prospect of using advanced methods (third generation SC), such as an intermediate band or up/down conversion have been proposed, thus allowing for idealized systems including lossless contacts and optimal absorption [5], [6], [1].

Introducing an intermediate band in the middle of the solar cell structure is considered a promising way of increasing the efficiency of solar cell devices. Intermediate band solar cells (IBSCs) allow two additional transitions for photons that have energies less than the energy of the material band gap. This helps in absorbing more light and generating more current.

Contributing to solar efficiency enhancements, intermediate band solar cells are a comparatively novel solar cell concept that has a maximum efficiency conversion that is considerably higher than that of conventional single band gap solar cells. It has been proven by theoretical studies that the efficiency limit of a quantum dot intermediate band solar cell is over 63%, while the conventional p-i-n junction solar cell has a 41% efficiency limit [8]. To implement the concept of the intermediate band (IB), the construction of several quantum dot (QD) layers in the middle of the solar cell device has been suggested. Quantum dots are considered one of the most important structures to be implemented as an intermediate band for high efficiency intermediate band solar cells. The nature of the three-dimensional quantum confinement is the reason why the QDs are candidates for high efficiency [7], [8], [9], [10].

Quantum dot intermediate band solar cells are considered an excellent material system for space applications. The primary power source for satellites is solar energy and, historically, space applications have pioneered many solar-cell technologies. For space applications, many different structures for solar cells have been developed. However, higher standards of efficiency, weight, lifetime, and reliability must be achieved for the next generation of solar cells for spacecraft applications. The development of novel nanomaterials and thin film technologies might address these issues. Due to concentrated irradiation of solar panels by alpha-particles, gamma-photons, protons, electrons, and neutrons, there is significant degradation in the solar cell efficiency over time. This degradation in the efficiency of solar cells is mainly caused by a degradation of the short circuit current and loss of transparency in the solar cell protective glass coating. Therefore, increasing the short circuit current for such applications is essential. Quantum dot intermediate band solar cells show a significant increase in the short circuit current,

which has been found to be suitable for space applications, even though so far the solar efficiency for this type of solar cell is insufficient [11], [12], [13].

At present, the advent of a more advanced intermediate band, such as InAs quantum dots, is promising and may lead to very economical prototypes in solar energy systems. Specifically, theoretical calculations suggest that quantum dot intermediate band solar cell efficiency can exceed the single junction solar cell. However, experimental efforts to fabricate QD intermediate band solar cells result in a degradation of the device characteristics as compared to reference p-i-n GaAs solar cells. The primary reason of the QD intermediate band solar cell's efficiency degradation is found to be a reduction in open circuit voltage (V_{oc}) [9], [11]. Figure 2 shows the current-voltage characteristics under the Air Mass 1.5 (AM 1.5) irradiation illustrating the increase of the short circuit current and decrease of open circuit voltage, leading to a decrease of the solar cell conversion efficiency of a QD IBSC compared to a p-i-n solar cell.

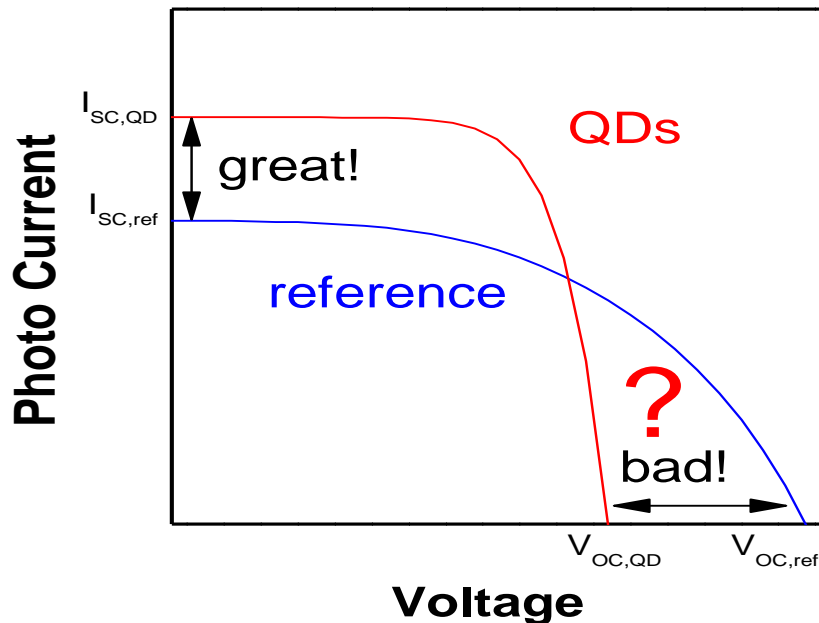


Figure 2. A schematic graph showing I_{sc} increase and V_{oc} decrease in the IBSCs compared to reference p-i-n SCs.

Many researchers are trying to study and understand the mechanisms which affect V_{oc} in IBSCs. Recently, it has been suggested that the open circuit voltage depends on quantum dot size in such a device [9], [14], [15], [16]. The goal of this work is to investigate, in a systematic way, the role of the quantum dot height on the performance of QD intermediate band solar cells. The objective is to understand the possible mechanisms of V_{oc} degradation, and thus, the decrease of conversion efficiency of IBSCs. To realize these goals experimentally: (1) the QD IBSCs were grown using molecular beam epitaxy; (2) QDs were grown using SK growth and QD heights were varied using the capped and annealed truncation technique; and, (3) different measurement techniques were applied to understand structural, optical and electrical properties of QD IBSCs.

Chapter 2: Theoretical Background

2.1. Brief Introduction to Semiconductor Physics

2.1.1. Semiconductor Materials

Semiconductors are comprised of a group of materials that have very unique properties because they have intermediate electrical conductivities between insulators and metals. The importance of having such a property is that the semiconductor material conductivities can be controlled by varying the optical excitation, impurity content, and temperature [17].

Semiconductor materials are in column IV and neighboring columns in the periodic table. There are elemental and compound semiconductors. The elemental semiconductors, group IV materials in the periodic table, have a single species of atoms such as silicon and germanium. Such materials are widely used in the development of transistors, diodes, rectifiers, and integrated circuits. The compound semiconductors are made up of a combination of group III and V atoms (or II and VI), such as GaAs and CdTe, and are widely used in light emitting diodes and high speed devices [17].

Important characteristics that distinguish semiconductors from metals and insulators are their band structure and energy gap, which are responsible for varying the electrical characteristics in numerous materials. The energy bands of metals either have to be partially filled or overlapped. On the other hand, in insulators, the valence bands and the empty conduction band are separated by a large band gap. Therefore, a negligible number of electronic excitations from the valence band to the conduction band occur due to the large band gap (10 eV). Semiconductors behave identically to insulators at 0 K; however, the band gap energy is different. The band gap of the semiconductors is smaller than that of insulators. Consequently,

thermal or optical excitation of electrons from the valence band to the conduction band is allowed in semiconductors due to the relatively small band gap [17]. A schematic of the energy bands of metals, semiconductors, and insulators is illustrated in Figure 3 [18].

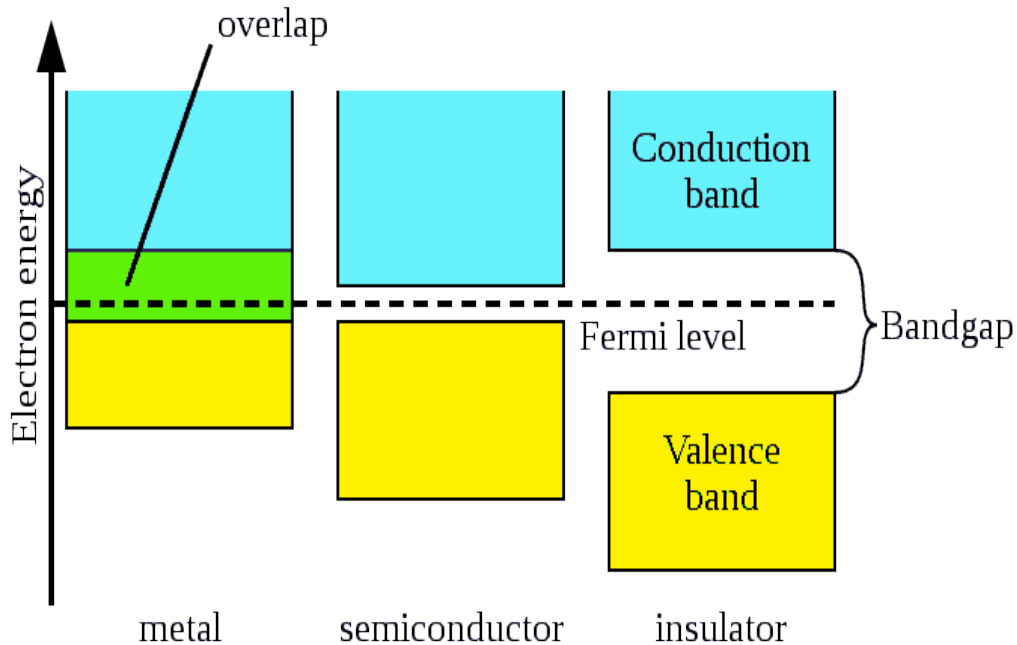


Figure 3. A schematic of energy bands of metal, semiconductor, and insulator [18].

2.1.1.1. Intrinsic Semiconductors

Intrinsic semiconductor materials have no lattice defects or impurities added to them that would change the carrier concentration in the crystal. At 0 K, the valence band is full of electrons, while the conduction band is empty. Therefore, there are no charge carriers in the conduction band at 0 K. On the other hand, at high temperature, the electrons in the valence band excite thermally to the conduction band, generating electron-hole pairs. The charge carriers created by these electron-hole pairs are considered the only charge carriers in the intrinsic semiconductor materials, and the concentration of the charge carriers in this case is called the intrinsic carrier concentration [17], [19].

There are two factors that can affect the number of carriers: the temperature and the band gap of the material. Materials with a large band gap have lower intrinsic carrier concentrations due to the difficulty of thermally exciting electrons from the valence band to the conduction band across the large band gap. However, the probability of exciting an electron from the valence band to the conduction band is increased at high temperature. Therefore, the intrinsic carrier concentration increases with temperature. Studying the factors that affect the intrinsic concentration is of vital importance for solar cell studies as this affects the material conductivity and, thereby, affects the solar cell conversion efficiency [19].

2.1.1.2. Extrinsic Semiconductors

Extrinsic semiconductor materials are semiconductors that have some impurities added to their crystal lattice to change the equilibrium carrier concentrations from the intrinsic carrier concentration. By adding some impurities to a crystal, it is possible to create some carriers in addition to the intrinsic carriers in semiconductors. Such a process can change the conductivity of semiconductors by allowing the crystal to have an excess of either holes or electrons. Externally varying the number of holes (p-type) and electrons (n-type) in semiconductors is called doping, and it is a very common technique [17], [20].

2.1.1.3. Direct and Indirect Semiconductor

In direct band gap semiconductors (such as Gallium Arsenide), the conduction band minimum and valence band maximum have the same wave vectors, \vec{k} . However, in indirect band gap semiconductors (such as silicon), the conduction band minimum and the valence band maximum have different wave vectors. An electron in a direct band gap semiconductor can transfer from the conduction band to the valence band without requiring any change in the wave vector. When this occurs, the electron transfers its full energy, which is equal to the difference

between the CB and the VB, as a photon of light. However, in indirect semiconductors, an electron needs to change its momentum (by changing its wave vector), thereby transferring energy to the lattice as heat, in order to make a transition from the CB to the VB [17], [21], [22]. A schematic diagram of direct and indirect semiconductors is shown in Figure 4 [23].

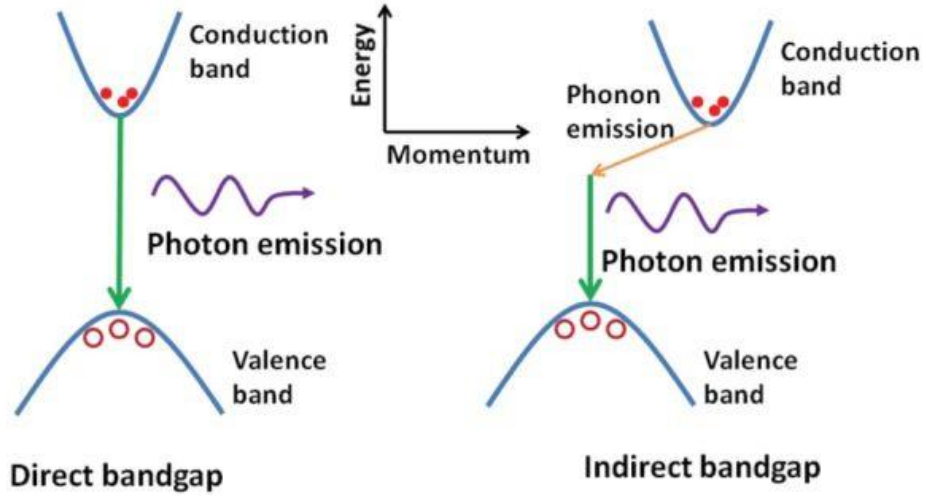


Figure 4. A schematic diagram of direct and indirect semiconductors [23].

2.1.2. Fermi-Dirac Distribution (E_F)

In solids, the probability of an electron occupying an energy state in thermal equilibrium is described by the Fermi-Dirac distribution. At thermal equilibrium, the electron distribution over allowed energy states is described by Equation 1.

$$f = \frac{1}{1 + e^{(E - E_f)/kT}} \quad (1)$$

where f is the probability of finding an electron with energy E , E_f is the Fermi level, k is Boltzmann's constant (8.62×10^{-5} eV/K), and T is temperature. Understanding the Fermi-Dirac distribution helps in understanding and analyzing the semiconductor material's behavior and

calculating the electron and hole concentrations. At high temperatures, the probability of occupying an allowed energy level by an electron is equal to 1/2 when the energy (E) is equal to the energy of the Fermi level. At 0 K, the allowed energy levels above the Fermi level are empty while the energy levels which are up to the Fermi level are occupied by electrons. However, there is a finite probability of electrons filling some of the states above the Fermi level at temperatures above 0 K [17], [21].

In intrinsic semiconductors, the Fermi level lies in the middle of the band gap between the conduction band and the valence band because the concentration of holes in the VB is equal to the concentration of electrons in the CB. In p-type semiconductor materials, the Fermi level lies below its intrinsic position because the hole concentration in the VB is higher than the electron concentration in the CB in these materials. Conversely, in n-type semiconductor materials, the Fermi level lies above its intrinsic position because the electron concentration in the CB is higher than the hole concentration in the VB [17], [21]. The position of Fermi levels of n-type and p-type semiconductor materials is illustrated in Figure 5.

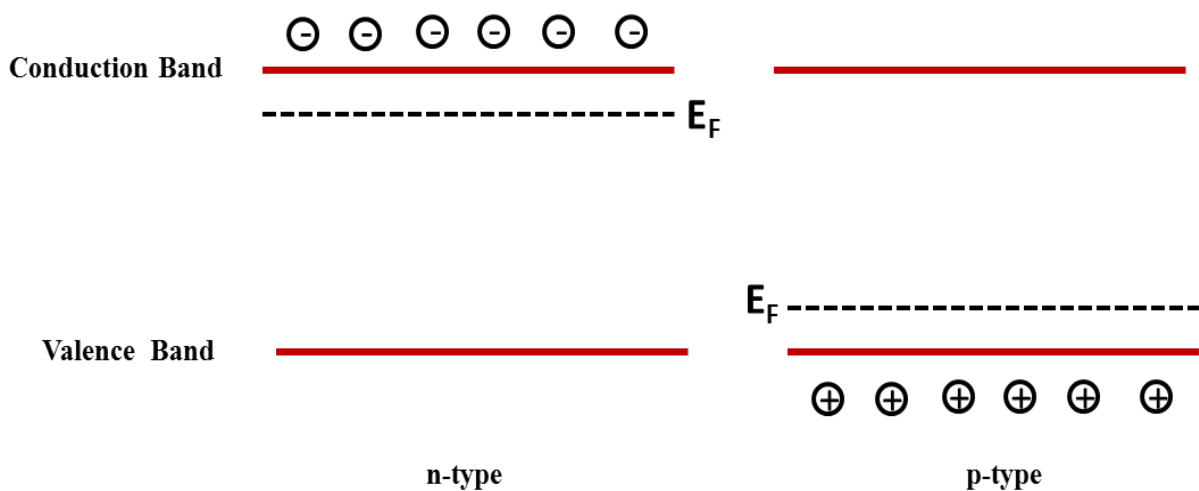


Figure 5. A schematic diagram of Fermi level position in n-type and p-type materials.

2.1.3. Generation and Recombination

Semiconductors consist of minority carriers and majority carriers. Even though the number of minority carriers is very small, the minority carriers have the opposite charge of the majority carriers. Therefore, minority carriers can yield some effects in addition to the majority carrier effects. Thus, determining the minority and majority carrier concentrations is important. Generation and recombination rates are very essential in determining the concentration of both types of carriers [21].

The generation of free electrons and holes is the process in which a given energy allows the excitation of an electron from the valence band to the conduction band and leaves a hole in the valence band, creating an electron-hole pair. When all the dopant atoms are ionized, no more free electrons and holes can be generated [21]. Recombination is the process in which energy is given back to the lattice by a free electron recombining with a hole in the same structure. This process leads to the annihilation of an electron-hole pair.

There are many factors that affect the recombination and generation rates. The recombination of an electron and hole is affected by the electron and hole concentrations. When the free electron concentration is high, there is a higher probability for a free electron and a hole to meet and recombine. The generation rate and recombination rate are related. At high temperatures, the generation of electrons and holes increases. Consequently, the recombination rate increases to the same level as the generation rate to limit the electron-hole concentrations to a certain level. In addition, the generation and recombination rates are equal in thermal equilibrium. At 0 K, the concentration of free electrons and holes is zero and, therefore, recombination and generation rates are also zero. However, the generation and recombination

rates increase rapidly with the increase of temperature, because the concentration of free electrons and holes increases [21].

The recombination process of electrons and holes happens as a result of several mechanisms. The four primary mechanisms that lead to electron-hole recombination are: Shockley-Read-Hall recombination (SRH), radiative recombination, non-radiative recombination, and Auger recombination. Defects in the semiconductor material can act as traps by forming an energy level in the forbidden band gap. The recombination of an electron and hole caused by a defect is called a Shockley-Read-Hall Recombination (SRH). The SRH recombination does not take place in pure materials that have no defects. Therefore, this mechanism can be avoided by growing pure materials without defects [24], [21], [25].

Differently, radiative recombination or band-to-band recombination, occurs when an electron emits its energy as a photon by leaving the conduction band and recombining with a hole in the valence band. Radiative recombination takes place in direct band gap semiconductors since the lowest energy transition between the conduction and valence band appears for the same wave vector. This type of recombination is considered the simplest mechanism to occur and the hardest type of recombination to avoid. Unlike radiative recombination, non-radiative recombination occurs in indirect semiconductors. The electron leaves the conduction band minimum (CB_{\min}), that has a different wave vector than the valence band maximum (VB_{\max}), thereby releasing its energy to the lattice phonons. In non-radiative recombination, both the momentum and energy of the electron change [21], [25].

The fourth recombination mechanism is called Auger recombination: a process in which an electron recombines with a hole in a band-to-band process and gives its energy to another electron. Highly doped regions have high carrier concentrations, which leads to an increase in

the carrier-carrier scattering mechanism. Therefore, when one electron crashes into another electron, one of the electrons transfers its energy to the other one. The electron that loses its energy is recombined with a minority carrier or trapped by a defect located in the band gap. To prevent this type of recombination, it is necessary to reduce the electron injection level in the material by lowering the applied electrical current [21], [25]. Figure 6 illustrates SRH, radiative, and Auger recombination mechanisms.

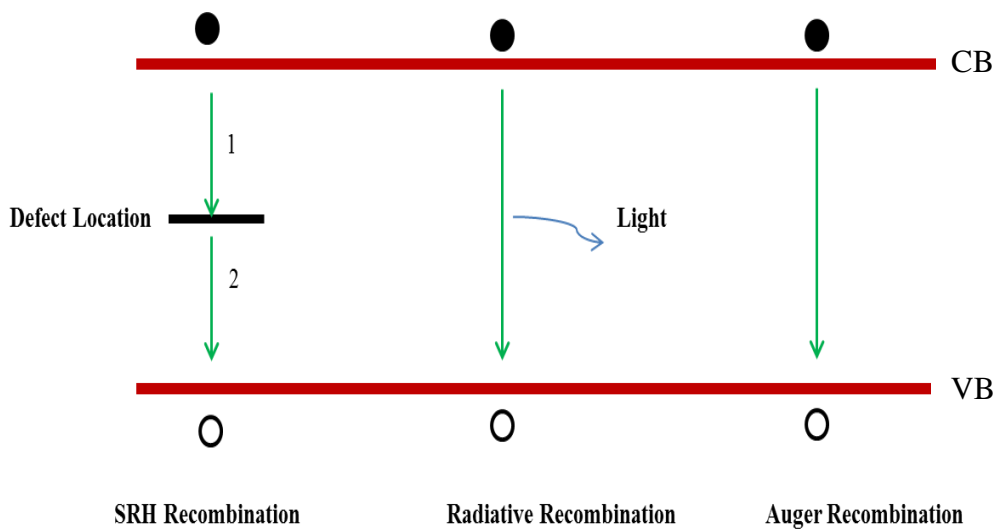


Figure 6. A schematic of Shockley-Read-Hall (SRH), Radiative, and Auger recombination mechanisms.

2.1.4. p-n Junction

A p-n junction is a combination of a p-type semiconductor, which has a majority of holes (example, GaAs doped with Be), with an n-type semiconductor, which has a majority of electrons (example, GaAs doped with Si). Since the amount of positive charges and negative charges is large compared to each other in the p-type region and n-type region respectively, a diffusion process starts to occur between the two regions. Positive and negative ions are generated in the place where the electrons and holes, respectively, transferred from during the

diffusion process, resulting in a built-in electric field at this space charge region (junction region). The built-in electric field then causes the positive and negative charges to return to the p-region and n-region respectively, toward the opposite direction of the diffusion. Since the diffusion and the built-in electric field have opposite directions, the flow of the electrons and holes will balance and reach stable equilibrium [26]. Figure 7 illustrates the diffusion process and the depletion region created by the built-in electric field.

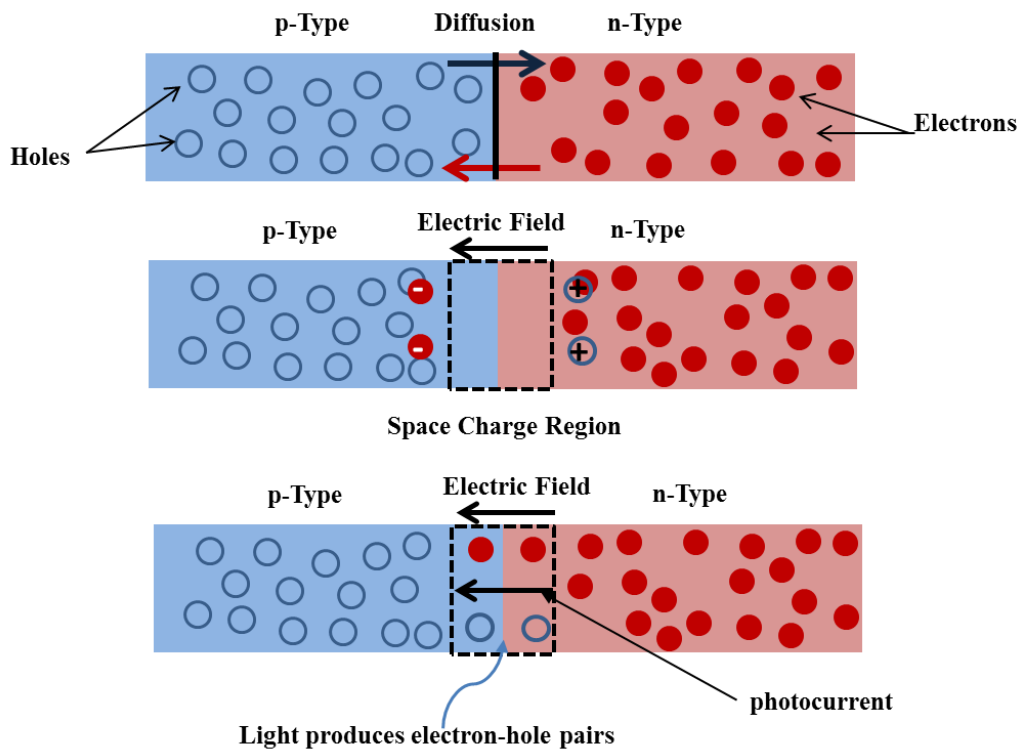


Figure 7. p-n junction in thermal equilibrium and under illumination.

Applying a voltage to the n or p region can affect the width of the space charge region, depending on the type and amount of voltage applied. Applying a positive voltage to the p-side and a negative voltage to the n-side (Forward Bias) results in a current flow in the opposite direction of the electric field, thereby narrowing the width of the space charge region. However, applying a negative voltage to the p-side and a positive voltage to the n-side (Reverse Bias)

results in a current flow in the same direction as the electric field, thereby widening the space charge region width [26].

2.2. Photovoltaics

2.2.1. The Solar Spectrum

The space solar spectrum can be approximated by black body radiation from a 5900 K source. Taking into account the distance between the sun and earth, the light that passes through the atmosphere is not fully contributing to the solar spectrum reaching the earth, due to the fact that gasses can result in absorbing, scattering, and reflecting some of the sunlight. To measure the effect of the absorption on the earth-reached-solar radiation, the air mass is measured using Equation 2.

$$\text{Air Mass} = \frac{1}{\cos \theta} \quad (2)$$

Where the angle θ is the incidence angle. The spectral distribution with an integrated power of 1366.1 W/m² is named air mass zero (AM 0), and this is considered to be a standard spectrum for space application. To compare the performance of solar cells, an air mass 1.5 (AM 1.5) global standard spectrum is used. This spectrum is normalized to a power density of 100 mW/cm². An air mass 1.5 global (AM 1.5 g) refers to the spectrum that takes into account the reflection and scattering in the atmosphere, while an air mass 1.5 direct (AM 1.5 d) refers to the spectrum which does not take the spectral content diffused component into account [2], [27], [28]. Figure 8 illustrates the solar spectra irradiance AM 0, AM1.5 g and 1.5 d [28].

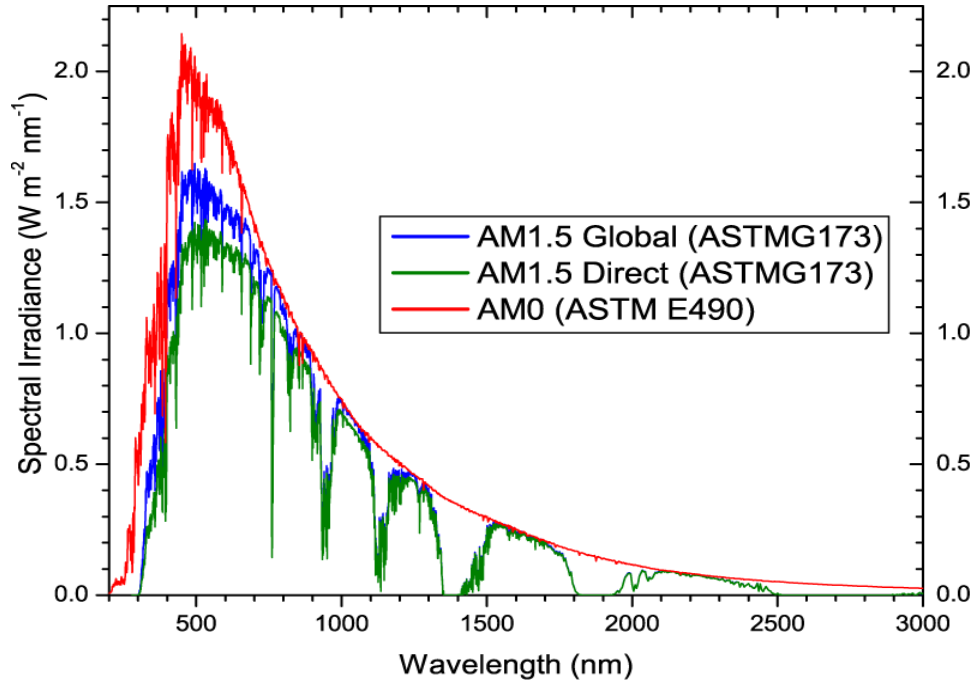


Figure 8. The solar spectra irradiance of AM0, AM1.5g and 1.5 d [28].

2.2.2. Basic Principle of Solar Cells

Solar cells can be defined as p-i-n device that convert a wide-range of the incoming spectrum from the sun into an electric current [29], [2]. A schematic diagram of a solar cell device is shown in Figure 9. When the sunlight hits the solar cell, the solar cell device captures photons from the solar spectrum by absorption. The process of absorbing photons transfers energy to electrons. The electrons with energy equal to or larger than the material band gap ($h\nu \geq E_g$) are then excited from the valance band to the conduction band, which results in the creation of electron-hole pairs. The built-in electric field in the p-i-n junction then causes the separation of the electrons and holes. The electric field in the depletion region moves the electrons and holes in opposite directions, resulting in a voltage that drives a current through an external circuit. Therefore, the solar power generated is the result of this voltage and current. The current that passes through the solar cell when $V = 0$ Volts is called the short-circuit current (I_{sc}).

However, the maximum voltage of the solar cell device takes place when the device is not connected to any circuit, meaning that it has a current equal to zero, and is known as the open circuit voltage (V_{oc}). The behavior of the solar cell can be characterized by I-V curves, where the short circuit current, open circuit voltage, maximum power, filling factor and solar efficiency can be extracted [2], [29]. A detailed description of how to calculate the solar efficiency is explained in Section 3.3.3.2

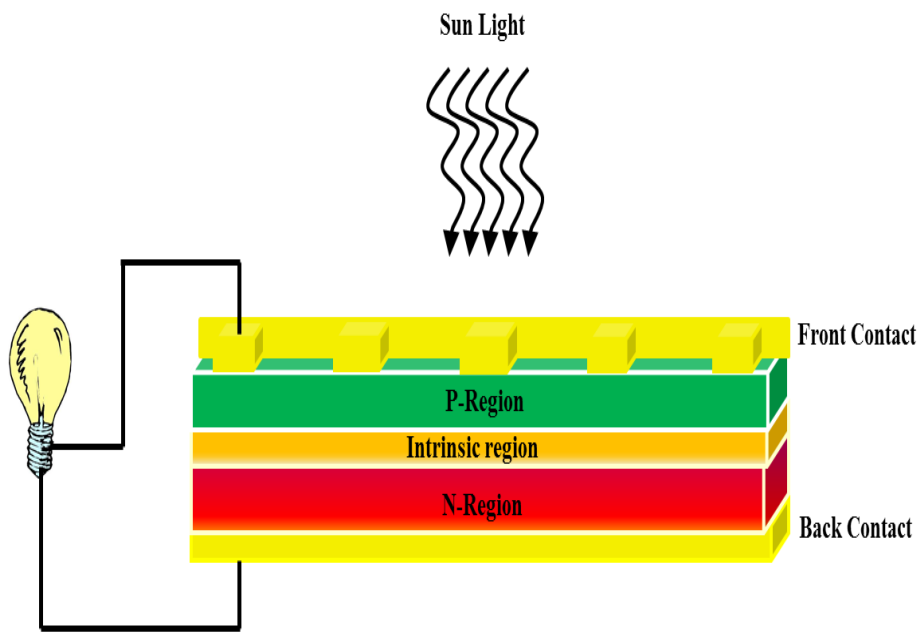


Figure 9. A schematic diagram of a solar cell (bulb photo [30]).

2.2.3. Limits of Photovoltaic Conversion-Efficiency

There are some limiting factors of solar conversion-efficiency that are worth mentioning. The first limiting factor is non-absorption of photons, which can be due to the band gap or reflectance restrictions. Photons that have less energy than the band gap of the semiconductor material in the solar cell absorbing layer cannot be absorbed. Thus, they are unable to generate an electron-hole pair that contributes to the solar efficiency. Therefore, choosing a material with an optimum band gap and good optical properties is very essential to increase the conversion efficiency of solar cells [5], [14]. Figure 10 [31] illustrates the maximum theoretical efficiency conversion of different materials with different band gaps under AM1.5 illumination.

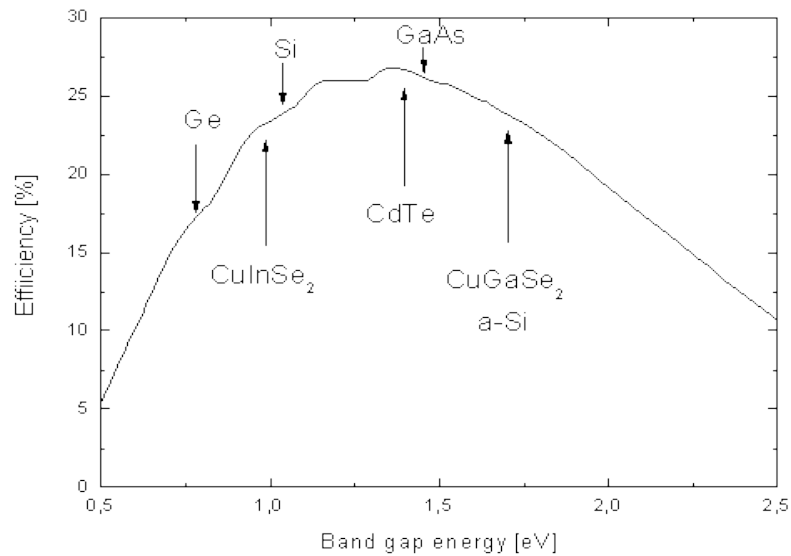


Figure 10. The maximum theoretical efficiencies under AM 1.5 illumination versus bandgap energy [31].

Also, incident light on solar cell surfaces can be reflected, absorbed or transmitted. In solar cells, the reflection of the incident light is one of the limiting factors of solar conversion-efficiency. The reflectance of incident light can happen at the interface of the solar cell and the

air. Reflectance can also occur between the solar cell individual layers, thereby affecting the total absorption of the incident light that can contribute to the solar cell efficiency [5].

The third factor limiting conversion efficiency is the limited thickness of the solar cell absorption layer. Even though all the layers in the solar cell structure are capable of absorbing some of the incident light, the solar cell structure is designed to have a specific absorption layer that can absorb the incident light and generate current. The absorption layer has a limited thickness that limits the absorption of the incident light, thus reducing the solar cell conversion-efficiency [5].

Shading losses can also contribute to solar efficiency reduction. In the fabrication process of solar cell devices, two different metal electrodes are created to make electrical contact with the n-type and p-type materials. In some solar cells, one of the electrodes will be placed on the top of the solar cell where the incident light hits the front surface of the solar cell device. The areas covered by the metal contacts on the front side of the solar cell reflect the incident light, thus reducing the effective active area of the device and decreasing the total solar conversion efficiency [5], see Figure 11.

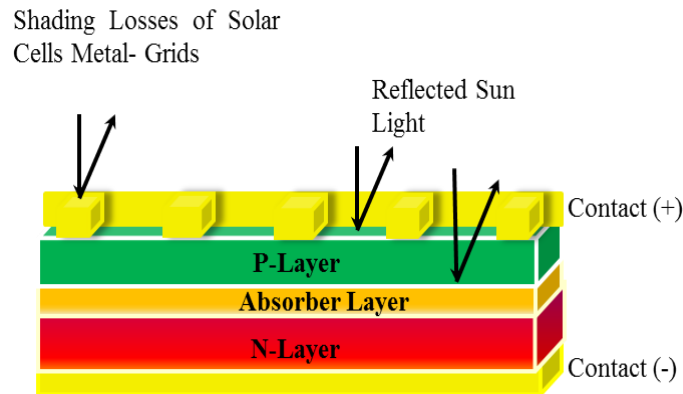


Figure 11. Solar efficiency conversion factors: shading, reflectance, and absorber layer limited thickness.

Moreover, the thermalization mechanism can negatively affect solar efficiencies. Carriers have the tendency to find lower energy states. Therefore, electrons excited to the conduction band tend to occupy the lowest energy level at the edge of the conduction band, see Figure 12. Similarly, the holes in the valence band tend to occupy the lowest energy level at the edge of the valence band. The process in which the carriers lose some of their energy as heat (transferred to the lattice) when they move to the edges of the conduction band and valence band is called thermalization. Energy loss caused by thermalization is considered one of the biggest contributing factors to the limitation of the solar conversion-efficiency [5].

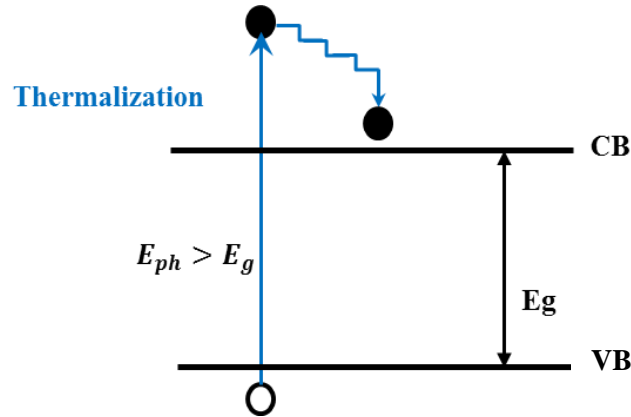


Figure 12. Thermalization and energy loss in solar cells.

Finally, the electron-hole recombination process is another reason for the solar efficiency limitation. Generating an electron-hole pair contributes to the external current and efficiency of the solar cell. In contrast, the recombination process has a negative effect on the total current supplied to an external circuit. Due to recombination mechanisms at the surface of the junction, at interfaces, and in the bulk, only some of the generated carriers will be collected by the metal electrodes of the solar cell device [5], [14].

2.2.4. Strategies to Increase Efficiency

The way to increase the efficiency of solar cells is by reducing the effect of the efficiency-conversion limiting factors, especially losses caused by non-absorbed photons and thermalization. There are several promising approaches that have been studied to increase solar cell efficiency, including: (1) increasing the exciton generation by enhancing carrier generation using a high energy photon to generate two electron- hole pairs, (2) collecting the photo-generated carriers before thermalization by slowing the cooling rate of photo-excited carriers and capturing these carriers before thermalization, leading to higher cell voltages (such an approach is attributed to the hot carrier cells), and (3) increasing the number of energy levels and enhancing photon absorption. Intermediate band solar cells and tandem solar cells are two examples of this approach. Implementing an intermediate band in the middle of a material band gap allows lower energy photons to be absorbed. Also, using a multi-junction structure can help to enhance the absorption in a wider range of the solar spectrum [14], [32], [1].

2.3. Intermediate Band Solar Cell (IBSC)

2.3.1. High Efficiency Conversion Limit

Nowadays, studying and optimizing the efficiency of the intermediate band solar cell, which is a new promising photovoltaic device, is of vital importance. The intermediate band solar cell efficiency is higher than the efficiency of the single band gap solar cell. Under maximum concentration, the solar efficiency limit of the intermediate band solar cell is 63%; however, the single band gap solar cell efficiency limit is 41% [33], [16], [34], [35], [36]. Figure 13 [37] illustrates the maximum theoretical efficiencies of intermediate band, tandem, and single gap solar cells.

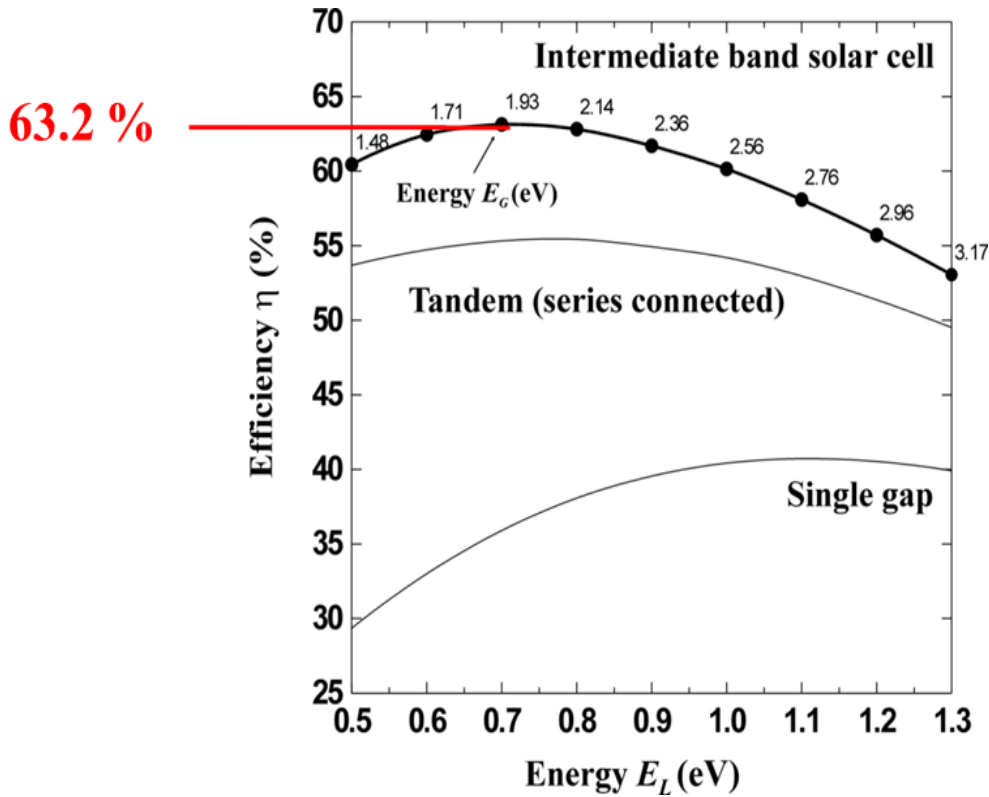


Figure 13. Efficiency limit for an intermediate band solar cell, a two terminal-tandem solar cell, and a single gap solar cell [37].

The promising increase in the efficiency of intermediate band solar cells (IBSCs) has been attracting the attention of many researchers who have been trying to optimize these devices and investigate solutions to some of the device's implementation, fabrication, and performance challenges. By generating more electron-hole (e-h) pairs through the absorption of lower energy photons, the creation of the intermediate band (IB) has the potential to increase the efficiency of the solar cell without further degradation in the open circuit voltage (V_{oc}). The current in the intermediate band solar cell increases via lower energy photon absorption and the open circuit voltage does not degrade due to having the intermediate band sandwiched between large bandgap semiconductor materials and due to the existence of three electronic bands [33], [38], [3].

2.3.2. The Basic Concept of IBSC

The concept of the intermediate band solar cell is based on adding an intermediate band (IB) between the conduction band (CB) and the valence band (VB) of a semiconductor. In other words, an IBSC can be simply implemented using an intermediate band material sandwiched between n-type and p-type doped semiconductor materials with two metallic Ohmic contacts: one positioned at the side of the n-type base and the other positioned in the p-type emitter. There are two processes of sub-bandgap photon absorption that occur in an intermediate band solar cell. The first process is that a photon excites an electron from the valence band to the intermediate band. Then, another photon excites an electron from the intermediate band to the conduction band. Therefore, the two-photon absorption process of sub-bandgap photons contributes to an additional photocurrent in the solar cell when adding an IB to the device, thus contributing to an increase in the efficiency of such solar cells [16], [10].

Figure 14 describes the basic concept of the intermediate band solar cell operation. The three possible mechanisms of photon absorption are identified by the vertical arrows '1', '2', and '3'. Those mechanisms can only happen when the intermediate band is partially filled with electrons, thereby having empty states in the IB to receive electrons from the valence band and send it to the conduction band. The theoretical 63% solar efficiency of the IBSC corresponds to optimized bandgaps with a transition energy between the valence band and the intermediate band of $E_L = 0.71$ eV, between the intermediate band and the conduction band of $E_H = 1.24$ eV, and between the valence and conduction band of $E_G = 1.95$ eV [10], [39], [40], [41]. Figure 14 shows the intermediate band solar cell energy diagram and the electronic excitation process.

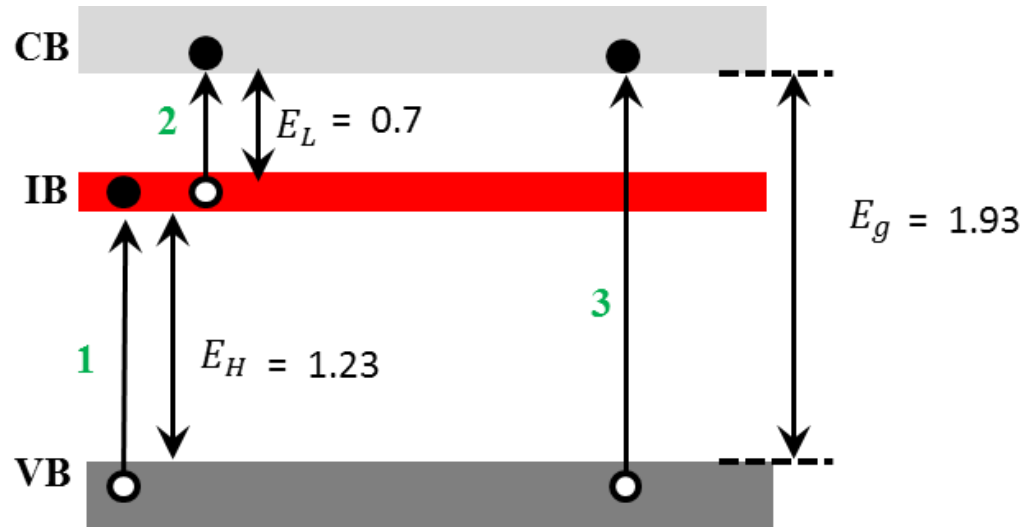


Figure 14. A schematic band diagram of IBSC. E_g is the fundamental bandgap, E_L and E_H the sub-bandgaps, adopted from [42].

2.4. IBSC Devices

2.4.1. IBSC Material Selection

2.4.1.1. III-V Compound Semiconductors and QDs for Solar Cells

III-V materials are popular and show the most successful results in PV applications. Currently, the highest efficiency solar cells are the multi-junction solar cells, which have been made of III-V compound semiconductors. These high efficiency solar cells made of III-V materials have been developed for space applications, such as satellites powered through concentrator systems and have the greatest potential for increased efficiency and performance. The high efficiency of these materials opens a huge potential market for compound semiconductors [29], [43]

Further advantages for solar cells are obtained when solar structures are grown on a GaAs substrate. Current solar cells have shown a 40.8% solar cell conversion efficiency through an

epitaxially grown lattice matched triple-junction solar cell containing a III-V compound semiconductor on a GaAs substrate [44], [45].

The band gaps of semiconductor materials determine their ability in responding to light. That is of vital importance to take into consideration when choosing the appropriate material for solar cell devices. The maximum energy conversion efficiency for solar cells produced using single semiconductor materials is achieved from materials that have a band gap ranging between 1.4 and 1.6 eV. GaAs is one of the most important materials in producing solar cell devices due to its band gap energy, 1.42 eV. Also, an important property of GaAs that results in high efficiency GaAs solar cells is having a direct band gap. That leads to the efficient conversion of photons to electron-hole pairs [46], [47], [29], [3].

Furthermore, GaAs solar cells are considered ideal for use in extreme conditions because they extended operating temperatures and high-energy efficiencies. Compared to other materials in real world conditions, GaAs is reliable under the influence of changing temperatures and extended illumination periods. Under one tenth of sun illumination, GaAs can operate close to its complete efficiency. GaAs is estimated to have 4% more power conversion efficiency than silicon. At high temperature, the energy output of GaAs continues to provide energy near its rated output, while silicon solar cell energy output drops by approximately 30% [46], [44], [43].

It is true that conventional GaAs solar cells are not suitable for mobile power systems since they are heavy and 10-100 times more expensive than other photovoltaic technologies. However, recently, GaAs solar cells have been developed to thin, new, flexible single-crystal solar cells. These cells can also be fabricated and manufactured with relatively affordable costs compared to the conventional cells by growing thin layers using a miniscule amount of gallium arsenide [43], [46].

GaAs is the leading photovoltaic technology for high reliability and performance. The efficiency of a single junction GaAs solar cell is getting close to the Shockly-Queisser limit. As an example, under AM 1.5 g solar illumination, NREL certified solar cell devices have been developed on flexible substrates for mobile power technology by Alta, with an efficiency of 28.8% and an open circuit voltage of 1.12 V [43], [48], [49].

In addition, quantum dots are a well-established and studied technology. Many studies have been done to understand the physics of quantum dots—small islands made up of a small band gap semiconductor material enclosed by a larger band gap semiconductor material. The low-dimensional quantum systems, like quantum dots, have great potential for building efficient electronic and/or optoelectronics devices such as solar cells [6].

2.4.1.2. GaAs and QDs for IBSCs

The implementation of the intermediate band solar cell was first reported in 2004 by fabricating a prototype of the quantum dot intermediate band. It was created using III-V materials, with GaAs as the barriers and InAs quantum dots to form the IB. Even though the band gap of GaAs is far from the theoretically proposed ‘optimum’ band gap for IBSCs, choosing GaAs as the bulk material and InAs as the intermediate band is considered an appropriate choice for the first IBSC implementation, due its ability to be synthesized with outstanding quality [50], [42], [10], [33].

Quantum dots have the ability to isolate the intermediate band from the CB and the VB, allowing the split of quasi Fermi levels (QFL) so that the carrier’s population is described by its QFL in each band, thereby, the relaxation of carriers in each band is much faster than the recombination. Also, by introducing multiple energy levels, quantum dot solar cells are capable of enhancing absorption of light and extending the absorption to the infrared range. The density

of quantum dots needs to be high so that the dots will be located close to each other, leading to an overlap of their electronic wave functions, enhancing the absorption coefficient of the solar cell [42], [39], [51].

Since GaAs and InAs have been well studied and characterized, and a lot of research has been done on the InAs/GaAs IBSCs, these materials were chosen to test the role of the quantum dot size on the IBSC.

2.4.2. IBSC Materials

The intermediate band solar cell concept has been implemented using different materials. The technologies studied for the purpose of fabricating high efficiency IBSC can be represented under three material categories: (1) nanostructures such as quantum dots and quantum wires (2) bulk semiconductor materials, (3) highly mismatched semiconductor alloys (HMA) [16].

Examples for the materials used to form the IBSC under these three groups are listed in Table 1.

IB Material	
Quantum Dots	In(Ga)As/Ga(N,P,Sb)As
	InAs/AlGaAs
	GaSb/GaAs
	GaAs/AlGaAs
Bulk	CuGaS ₂ :Sn,Fe
	GaAs:Ti
	CuInS ₂ :Sn
	GaN:Cr,Mn
HMA	ZnTe:O
	Ga(P,Sb)As:N

Table 1. Materials used to fabricate IB. Modified from [16].

2.4.3. Current QD IBSCs Performance

The existence of the IB in IBSCs has been proven experimentally. The two photon absorption (sub-band gap spectral response) from the valence band to the intermediate band and from the intermediate band to the conduction band using quantum dots in the implementation of the intermediate band principle has been measured. At low and room temperatures, the two step photon absorption in IBSC produced a photocurrent that is significantly higher than an identical GaAs reference cell (without an IB). Furthermore, the quantum efficiency of the sub-band gap has been increased by increasing the quantum dot layers. For n-type doped quantum dots, the short circuit current increased with the increase of doping, resulting in an improvement in the efficiency of the IBSC by 50% compared with a IBSC with the same structure but with undoped quantum dots. Moreover, in the structure of InAs/GaAs, it has been proven that increasing the density of quantum dots has improved the photon absorption between the intermediate band and the valence band [9], [51], [16], [52], [39], [42], [14].

However, the total efficiency of the fabricated QD intermediate band solar cells has not exceeded the reference sample efficiency due to degradation in the open circuit voltage of the device. At room temperature, the open circuit voltages of all the InAs/GaAs QD IBSC that have been reported are less than the open circuit voltages of the reference samples. In two cases, the open circuit voltage of the QD IBSC has been close to the reference sample with no quantum dots; however, the V_{oc} was measured while the solar cell device was being illuminated by a supraband-gap energy laser. Thermal escape of electrons from the intermediate band (IB) to the conduction band (CB) at room temperature has also been reported [16], [42], [9].

2.4.4. Suggestions for IBSCs improvement

2.4.4.1. Ways to Reduce Voltage Losses in QD IBSCs

There are some factors contributing to the voltage reduction in IBSCs. Reducing intermediate band to conduction band tunneling and thermal escape by increasing the spacing barrier thickness and introducing a strain relief layer have been found to reduce IBSCs V_{oc} losses. IB-CB carrier escape is caused by defects related to the localized energy levels and quantum dot excited states. The defects increase the probability of electrons being trapped in the defect states and increase the SRH recombination. Thermal escape is caused by the reduced value of the IB-CB gap, where phonons and thermal photons are contributing to a connection of some of the confined levels of CB and IB within the band gap at room temperature. The reduction in the intermediate band to the conduction band gap by about 0.2 eV can result in a reduction in the effective gap (E_g) due to the wetting layer states or augmenting the indium arsenide band gap due to strain build up. Also, it has been suggested by Luque *et al* to increase the spacer thickness between the quantum dot layers to larger than 20 nm and introducing a 2 nm InAlGaAs strain relief layer. This can decrease the wetting layer confining potential as well as produce a better quantum dot confined energy level distribution, thereby blocking the electrons from tunneling and escaping from the confined states to the continuum and reducing thermal escape. Also, using GaNAs, GaAsP, or GaP as a strain balancing layer has improved voltage losses in such devices [53], [34], [9].

Furthermore, optimizing the location of the quantum dots in the intrinsic region, taking into account the intrinsic region background doping level, has shown V_{oc} enhancement. The change of the quantum dot position in the intrinsic region has been studied by comparing the result of quantum dot layers positioned in the center of the intrinsic region, near the p-type

emitter region, and near n-type base region. High losses in the open circuit voltage have resulted in the solar cells with the quantum dot layers placed in a region where SRH recombination is dominant. With the n-type doped quantum dots, positioning the quantum layers either in the center of the intrinsic region or near the base region was suggested [54].

Moreover, enhancing open circuit voltage in IBSCs can also be achieved by reducing the InAs coverage. By the time that the two dimensional wetting layer reaches a critical thickness, the quantum dot growth occurs and the quantum dot density then increases with the increase of the InAs coverage. The increased density of the quantum dots can result in a reduction of the material quality when the device structure contains several QD layers. In QD IBSCs, reducing the InAs coverage has reduced the effect of the higher density of quantum dots on the material optical quality and the non-radiative recombination induced by defects, thereby enhancing the open circuit voltage in QD IBSCs [52].

2.4.4.2. Research Suggestion to Investigate the Reason Behind Open Circuit Voltage Degradation in QD IBSC

The variation in size can affect the band gap width and the lowest energy state's radiative life-time [55]. Theoretical studies have been performed to understand the effects of the quantum dot size on the intermediate band solar cell performance. Theoretically, in an IBSC system, QD size affects the open circuit voltage. Furthermore, some studies have suggested optimizing the size of the quantum dots before embedding them into the IBSCs structures [9], [40], [15], [16], [8]. However, no experimental studies have been done to specifically address the role of quantum dot size on the performance of IBSCs. This research experimentally explores the effect of QD height on the IBSCs performance in a systematic way that can provide insight into improving the IBSC material properties for manufacturing high efficiency solar cells.

Chapter 3: Experimental Techniques

3.1. Growth of QD IBSC devices

3.1.1. Molecular Beam Epitaxy (MBE)

Molecular Beam Epitaxy is an ultrahigh vacuum (UHV) based technique for growing high quality, crystalline materials through sub-monolayer control. In MBE, a solid source is heated to produce a beam of atoms or molecules in an ultrahigh vacuum environment that travel towards and impinge on a heated crystalline substrate surface. There, they diffuse along the surface and incorporate into the lattice of the crystalline structure of the substrate [56], [57], [58]. Figure 15 shows a schematic diagram describing some of the important MBE components that help in visualizing the basic principle.

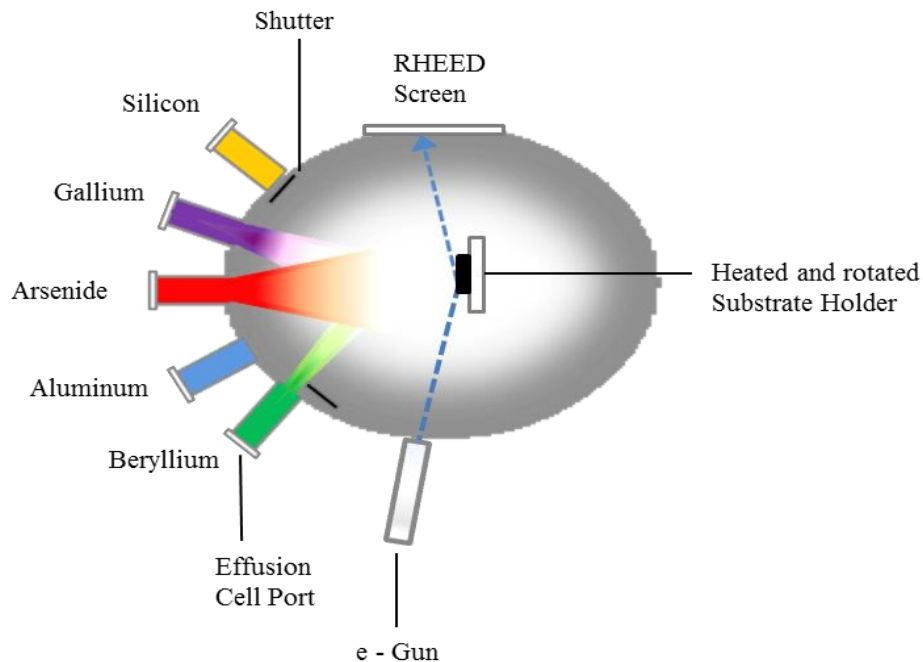


Figure 15. A schematic diagram of MBE chamber.

MBE consists of several cells with different sources. In Figure 15, arsenic, indium, gallium, and aluminum are considered the primary sources, where silicon and beryllium cells are the n-doping and p-doping sources, respectively. During the growth, the substrate is rotated to improve the material uniformity on the wafer. Also, the growth process is observed on a fluorescent screen using Reflection High Energy Electron Diffraction (RHEED). In this technique, high energy electrons are directed to the wafer surface at a grazing incident angle. When the electron beam reaches the sample surface, it reflects off a few atomic layers. Subsequently, an image of the diffraction pattern can be seen in the RHEED screen [56], [57].

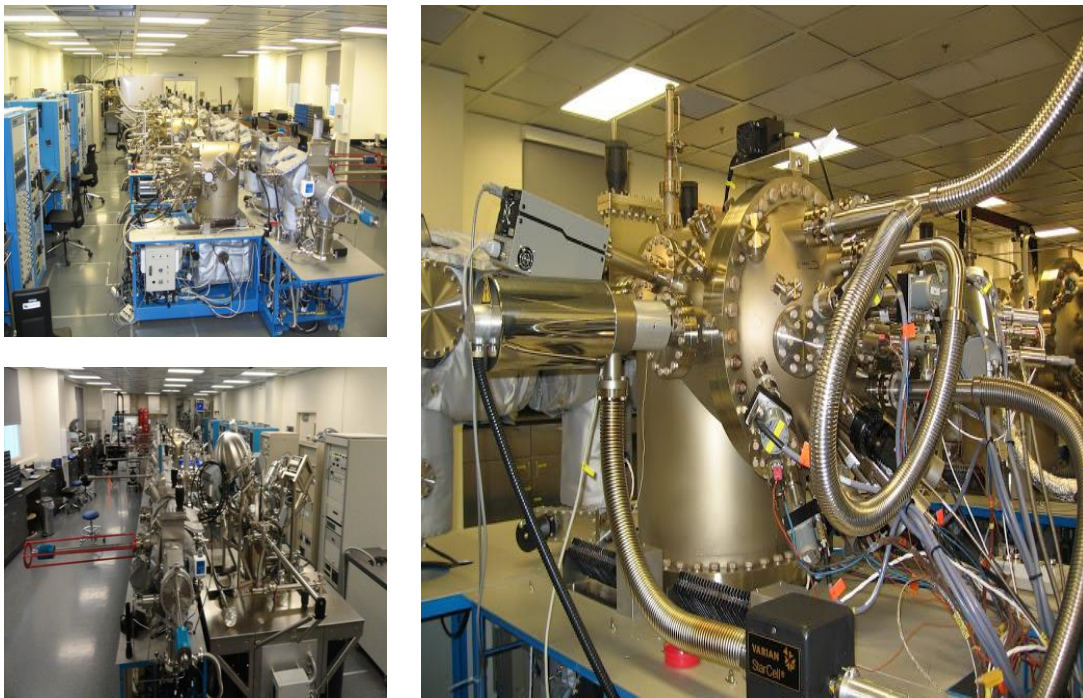


Figure 16. Riber 32P MBE chamber at the University of Arkansas Nano Facility.

Figure 16 illustrate the MBE lab and Riber 32P MBE chamber at the University of Arkansas. The MBE technique has led to major improvements in the realization of new electronic devices. It is a powerful technique for semiconductor band gap engineering and is

capable of producing heterostructures, multiple quantum wells, and superlattices. The MBE's powerful capabilities are a result of the ability to precisely control shutters, cells and substrate temperatures, material composition, thickness, crystal quality, and doping, allowing for the creation of sharp interfaces [57] .

3.1.2. QD Fabrication

3.1.2.1. Stranski-Krastanov Growth

There are a variety of methods that have been reported for quantum dot fabrication, such as self-assembled growth and e-beam lithography, followed by etching techniques. Compared to other QD growth methods, the Stranski-Krastanov (SK) growth method is considered one of the most important and suitable techniques to grow quantum dots. It is useful when modifying the size of quantum structures. Another attractive feature of SK growth is that self-organized quantum dots with high density, uniform size and shape, controlled interfaces, and high structural crystallinity can be achieved [59].

In the SK growth method, a 3D strain driven quantum structure can be achieved. To realize this, two materials that have a large lattice mismatch ($\sim 3-7\%$) and the same lattice structure are required, such as indium arsenide and gallium arsenide, which have a lattice mismatch of $\sim 7\%$. Figure 17 explains the basic principle of this type of growth. The InAs material with the larger lattice constant ($a_{\text{InAs}} = 0.60584 \text{ nm}$) is deposited on the GaAs with smaller lattice constant ($a_{\text{GaAs}} = 0.56534 \text{ nm}$). Subsequently, a 2D thin film of the InAs forms on the GaAs. When this film reaches a critical thickness ($\sim 1.7\text{ML}$), the lattice strain energy becomes stronger and the surface energy reduces, causing the 2D thin film to transform to 3D quantum dots. The resulting structure consists of a 2D wetting layer and a self-assembled quantum dot. This growth method is also called strained epitaxial growth. By covering the quantum dots with a

GaAs spacer and repeating the quantum dot formation growth, vertical stacks of quantum dots can be obtained [60], [61], [62], [63], [64], [65], [66].

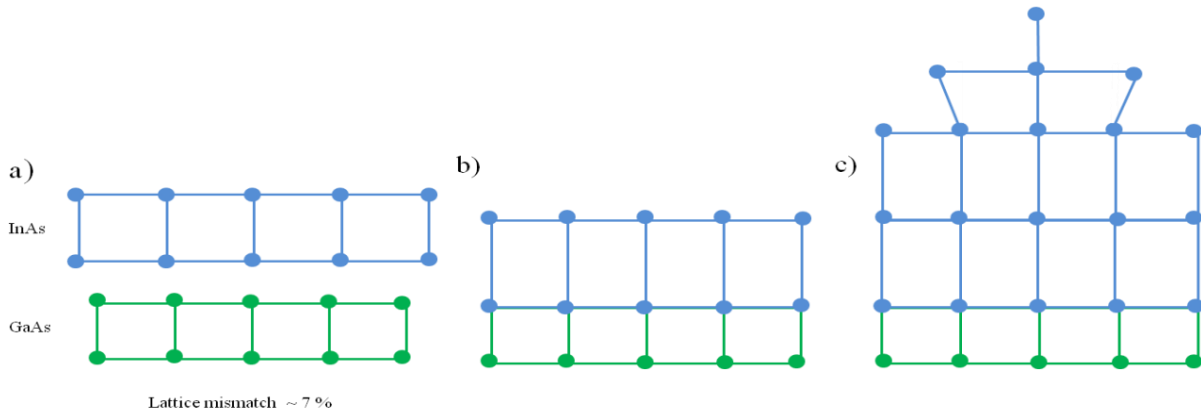


Figure 17. A schematic diagram of QD formation using SK Growth method.

3.1.2.2. QD Truncation

Using MBE, the quantum dot size and the quantum dot shape can be precisely controlled during the growth. By capping the self-assembled quantum dots with a layer of the barrier material via controlling the amount of the deposited material, growth temperature, and annealing time, the quantum dots can be truncated. In this way the size of the quantum dot can be accurately varied [67].

3.1.2.3. Growth Details

The plan in this project was to vary the height of quantum dots while keeping the density constant. Using molecular beam epitaxy, this plan was achieved by controlling the size, density, doping, and distribution of the quantum dots by changing different variables, such as the amount of InAs deposited, the arsenic flux, the substrate temperature, and the deposition rate. Using the well-defined Stranski-Krastanov approach, InAs/GaAs quantum dots were grown. InAs and

GaAs have a relatively high lattice mismatch of approximately 7%; therefore, depositing 2 monolayers of indium arsenide on a gallium arsenide (100) substrate resulted in QD formation.

Six different samples were grown as p-i-n solar cell structures. Five of them have been grown with quantum dots (QD IBSCs) named SF2, SF3, SF4, SF5, and SF7. The sixth sample is a reference sample that was grown at identical conditions but with no quantum dots, named SF0.

Figure 18 shows the grown structures of the reference and quantum dot samples.

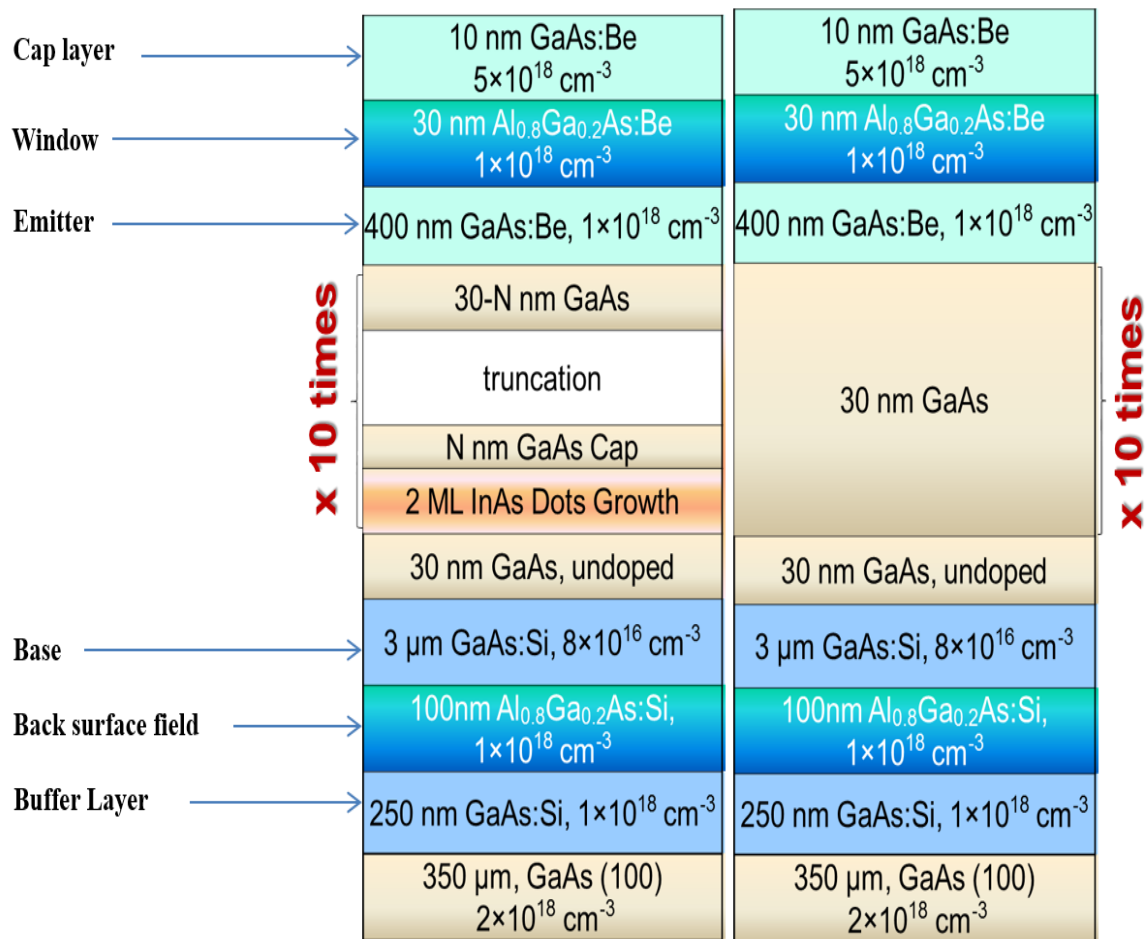


Figure 18. The QD IBSC solar cell and the p-i-n reference solar structures.

All the QD samples have ten layers of quantum dots, but each sample has a different quantum dot size. All samples were grown on a 350 μm thick GaAs substrate. Subsequently, a 250 nm thick Si doped GaAs buffer layer was grown at 580°C to smooth the substrate surface and to build a high quality crystal. After the buffer layer was grown, a heavily silicon doped (10^{18} cm^{-3}) $\text{Al}_{0.8}\text{Ga}_{0.2}\text{As}$ back surface field (BSF) layer was grown at 580 °C. On top of the BSF layer, a 3 μm GaAs base layer was grown with Si doping of $8 \times 10^{16} \text{ cm}^{-3}$. Then, the quantum dot formation step started by growing a 30 nm undoped GaAs layer at 580°C.

The growth of 2 monolayers of InAs QDs was done at 510°C. Normally at these growth conditions, the quantum dots have a height range between 5 to 7 nm. To vary the quantum dot heights in the five QD samples, the QD truncation technique was performed. GaAs capping layers of 2, 3, 4, 5, and 7 nm thicknesses were deposited at 510°C for the five samples, respectively. The thickness of the GaAs partial capping layer defines the height of the QDs. In other words, to have 2 nm quantum dot heights, a 2 nm GaAs capping layer was deposited following the QD growth. Then, the growth temperature was rapidly raised up to 540 °C, and annealed for 4 minutes in order to evaporate the exposed InAs to leave the truncated QDs. After getting the desired quantum dot height, a GaAs spacer layer was grown to have a total quantum dot and spacer layer thickness of 30 nm. For example, in the case of 2 nm QDs, a 28 nm GaAs spacer layer was grown on top of the 2 nm QDs. The steps for the quantum dot growth and truncation were repeated ten times. The ten InAs QD layers were grown to construct the intermediate band. The process of the quantum dot truncation is illustrated in Figure 19.

The ten layers of QDs were sandwiched between n and p type GaAs layers, thereby producing the structure for this project: a QD intermediate band solar cell. A 400 nm heavily doped 10^{18} cm^{-3} GaAs:Be layer was then grown on top of the ten QD layers. Next, a 30 nm $\text{Al}_{0.8}\text{Ga}_{0.2}\text{As}:\text{Be}$ (doped at 10^{18} cm^{-3}) was grown. The purpose of this layer in the solar cell structure was to minimize the electron recombination at the surface states as well as to use it as a window layer in the post growth processing of the solar cell. The reduction of recombination should increase the number of electrons participating in the photo current. Finally, a 10 nm thick $5 \times 10^{18} \text{ cm}^{-3}$ doped GaAs layer was grown to protect the AlGaAs layer from being oxidized.

Figure 18 illustrates the final QD and reference sample structures.

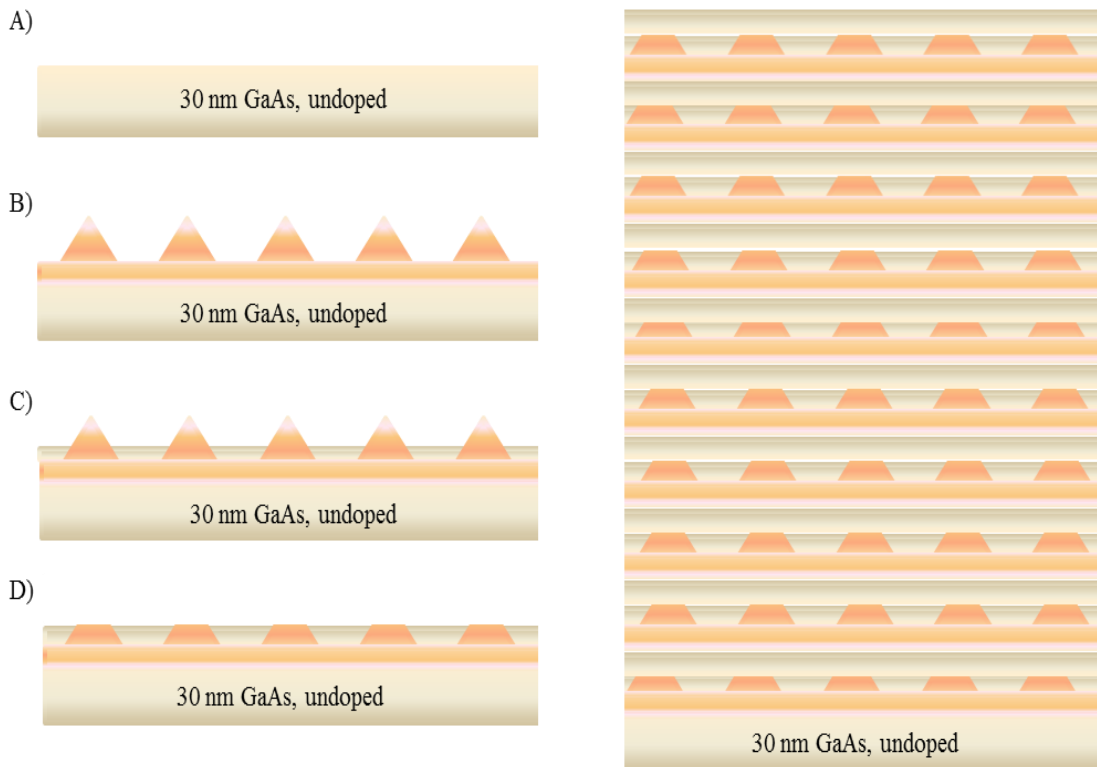


Figure 19. The process of quantum dot truncation.

3.2. Fabrication of QD IBSC device

3.2.1. Optical Photolithography

Optical photolithography is a set of processes used as an important step of semiconductor fabrication in which a micro-scale pattern on the surface of semiconductors can be prepared for etching. Before starting the photolithography process, cleaning the surface of the samples is an important step to get rid of dust, dirt, or any particles on the surface. The first step in processing is applying photoresist on the surface of the sample. After applying the photoresist on the surface, a spinning process is performed in order to achieve a thin film of photoresist with the desired thickness. In the third step, the photoresist material and its sensitivity to light have the ability to transfer the prepared mask pattern to the sample surface when it is exposed to UV light. The pattern transferred to the sample surface depends on the type of photoresist [25].

There are positive and negative photoresists. The chemical light sensitivity and formation of the positive and negative photoresists are different. In positive photoresists, the resist of the exposed areas are removed and washed away when added to a chemical solution developer. On the other hand, in negative photoresists, the resist of unexposed areas are removed and washed away during the developing process. The photoresist is usually soft-baked after the spinning process and before being exposed to UV light to evaporate the solvents. However, after being exposed to UV light, photoresist is hard-baked to increase the adhesion to the sample surface. Finishing the steps of cleaning, applying photoresist, soft-baking, UV exposing, hard baking, and developing, the surface of the sample will be prepared with the desired pattern and ready for selective etching or metallization [21], [25], [68], [21], [25].

3.2.2. Metal-Semiconductor Contacts

Preparing the semiconductor device with metal-semiconductor contacts is an important step during the device fabrication process. The resistance between the semiconductor device and the metal contacts cannot be assumed to be low, as in the case of two attached metals. Choosing inappropriate metal contacts for the semiconductor material can result in high-resistance and a mismatch between the Fermi level of the semiconductor and metal. For further metal-semiconductor contact resistivity improvement, annealing is performed after the deposition of the metal [69].

Ohmic contact is a metal-semiconductor electric junction that follows the characteristics of Ohm's law, which has linear current-voltage behavior. To form Ohmic contacts, the work function of the chosen metals should be close to the electron affinity of the semiconductor. The metal and semiconductor work function and electron affinity are illustrated in Figure 20-a. By applying a positive voltage to the metal, the resistance between the metal and semiconductor becomes smaller and the free carriers then have the ability to tunnel through the barrier and out of the semiconductor, see Figure 20-b. For n-type GaAs, a metallization system consisting of Au-Ge/Ni/Au has been studied extensively for use in electronic and optoelectronic device fabrication to form low resistance Ohmic contacts. For p-type GaAs, the commonly used Ohmic contacts are AuZn/Au, Au Be, and Au/Pt/Ti [70], [21], [69], [71].

In this research, standard optical photolithography, wet chemical etching and electron-beam metal evaporation for contact fabrication were applied. Both n-type and p-type Ohmic contacts were performed for all devices with AuGe/Ni/Au as an n-type contact and AuZn/Au as a p-type contact.

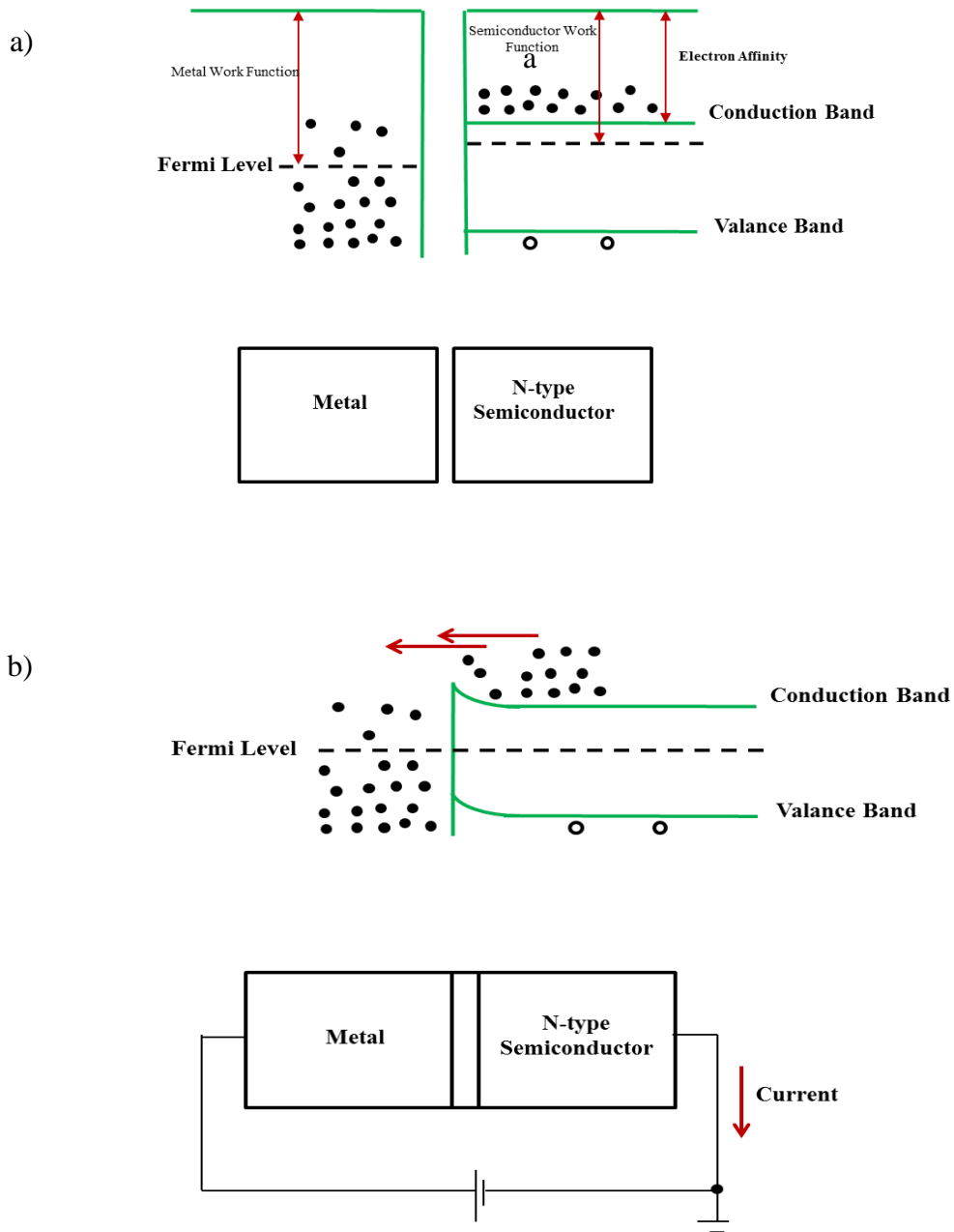


Figure 20. (a) The metal-semiconductor contact in thermal equilibrium. (b) Ohmic metal-semiconductor contact with positive voltage at the metal, adopted from [21].

3.2.3. Fabrication Details

All of the six grown samples were fabricated to solar cell structures using standard photolithography techniques, wet chemical etching, and metallization. High quality Ohmic contacts were made by annealing at different temperatures in dry nitrogen atmosphere. The n-type contact was annealed at 430 °C for 2 minutes and the p-type contact was annealed at 300 °C for 20 seconds in nitrogen atmosphere.

All six samples were processed as solar cell devices with active areas of $5 \times 5 \text{ mm}^2$. The solar cell structure fabrication is important for the device's solar conversion-efficiency and external quantum efficiency measurements. Figure 21 shows the solar cell structure.

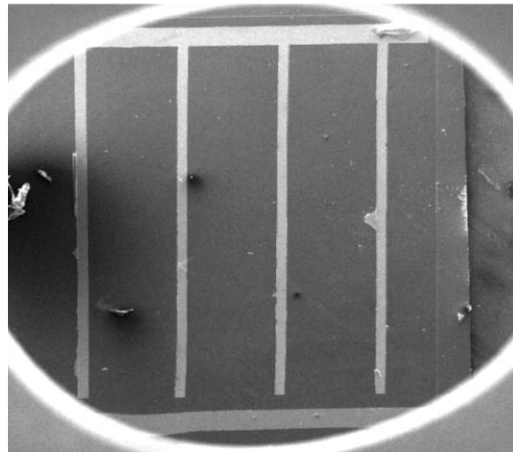


Figure 21. An SEM image for a typical solar cell structure.

The detailed solar cell fabrication procedures used to develop the six samples to solar cell structure devices is illustrated in Figure 22. To fabricate IBSC devices, samples were first prepared for a wet etching process. Samples were cleaned in acetone, methanol, and IPA for 5 minutes each, respectively. Then, AZ 5214 photoresist was applied and each sample was loaded onto the spin coater with a spinning rate of 5000 rpm for 20 sec. Subsequently, the samples were

baked at 110 °C for 3 min. Using a Dektak-3, the resulted photoresist thin film thickness was measured to be approximately 2.3µm. Before aligning the samples to the mask pattern and UV exposing, the exposure time was calculated using Equation 3.

$$\text{Exposure time} = \frac{\text{Nominal Energy of PR per micron} \left(\frac{\text{mJ}}{\text{cm}^2 \mu\text{m}} \right) \times \text{PR thickness} (\mu\text{m})}{\text{Lamp intensity} \left(\frac{\text{mW}}{\text{cm}^2} \right)} \quad (3)$$

The nominal energy of PR AZ5214 is given as 84 mJ/cm² for 1.25 µm of PR thickness.

$$\text{Nominal energy for 1 } \mu\text{m PR thickness} = \frac{84 \text{ mJ/cm}^2}{1.25 \mu\text{m}} = 67.2 \text{ mJ/cm}^2 \quad (4)$$

The photoresist thickness was 2.3 µm, and the mask aligner's lamp intensity was measured to be 11.52 mW/cm². Substituting these values into the exposure time equation, the exposure time required is equal to 13.4 seconds:

$$\text{Exposure time} = \frac{67.2 \frac{\text{mJ/cm}^2}{\mu\text{m}} \times 2.3 \mu\text{m}}{11.52 \text{ mW/cm}^2} = 13.4 \text{ s} \quad (5)$$

Then, the samples individually were aligned to the etching area defining pattern using the etching area defining mask (mask #1) and exposed to UV light for 13.4 seconds. Then, samples were transferred to the AZ300 MIF developer for 40 seconds to develop the exposed photoresist, thereby defining the etching areas.

The total thickness of the grown layers on the top of the substrate is 4.47 microns. Using the wet etching method, samples were etched 130 nm down into the substrate to have a total etched thickness of 4.6 microns. The etching solution used is H₃PO₃ : H₂O₂ : H₂O, with a ratio of the concentrations 1:1: 20. The etching rate was equal to 190 nm/min. After the etching step,

the samples were cleaned again using acetone, methanol, and IPA, respectively. Then, the depth of the etched material thickness was measured using Dektak-3. The measured etching thicknesses were ~ 4.6 microns for all samples.

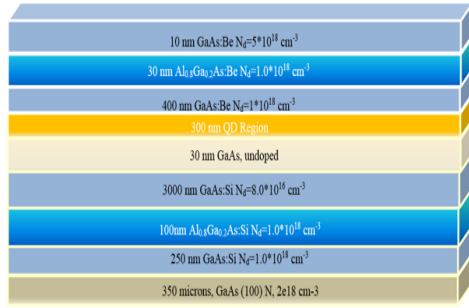
The second step of fabricating the IBSCs devices was preparing samples for n-type contact deposition (back-side contact). Photoresist was applied on the top of the samples to protect the surface when depositing the back side contact. Then, hard baking was performed at 110 °C for 3 minutes. Before depositing metals on the samples to form n-type contact, the oxide layer was etched using HCL: H₂O (1: 1) for 15 seconds. An e-beam evaporator was then used to deposit the n-type contact on the back side of the samples. The n-type contact was formed using AuGe/Ni/Au with thicknesses of 100/20/200 nm, respectively. The deposition rate was ~ 5 Å/s. After that, high quality Ohmic contacts were made by annealing at 430 °C for 2 minutes.

The third step of IBSCs device fabrication was preparing samples for p-type contact deposition (front-side contact). Samples were prepared for the (solar/diode structure) patterning mask (mask #2) by cleaning, applying photoresist, and hard baking as explained previously. Aligning samples to the pattern and exposure procedures were then repeated, using the solar cell structure defining mask (mask # 2). Then, solar and diode structure patterns were developed in AZ300 MIF developer for 2 minutes. Similarly to the n-type contact, an e-beam evaporator was used to form the p-type contacts. AuZn/Au with a thicknesses of 200 nm each were deposited to form the p-type contact. The deposition rate used was ~ 5 Å/s. The final step of the device fabrication process was done and the final device structure was then achieved by lifting off the unneeded photoresist and metals using acetone. Subsequently, the p-type contact was annealed at 300 °C for 20 seconds in nitrogen atmosphere. The sample fabrication procedures are summarized in Table 2.

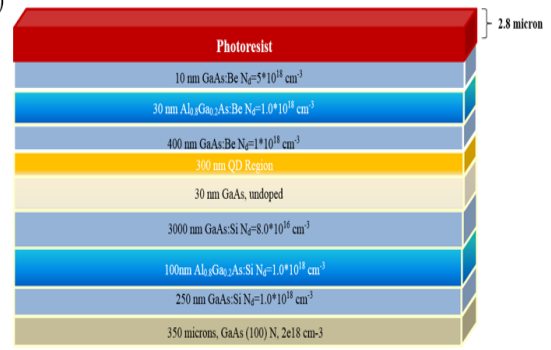
	Steps	Details
1	Cleaning	Acetone, Methanol, and IPA
2	Applying Photoresist & Baking	AZ5214 5000 rpm/20 s & 110 °C for 3 m
3	Exposing	13.4 s (Mask# 1)
4	Developing	40 s
5	Etching	(4.6 micron) H ₃ PO ₃ : H ₂ O ₂ : H ₂ O (1:1:20)
6	Cleaning	Acetone, Methanol, and IPA
7	Photoresist Application & Baking	AZ5214 5000 rpm/20 s & 110 °C for 3 minutes
8	Oxide Etching & Metallization	HCL:H ₂ O (1:1) for 15 s & AuGe/Ni/Au (100 nm/80 nm/ 200 nm)
9	Cleaning & annealing	Acetone, Methanol, and IPA & 430 °C for 2 m.
10	Photoresist Application & Baking	AZ5214 5000 rpm/20 s & 110 °C for 3 m
11	Exposure	13.4 s (Mask# 2)
12	Development	40 s
13	Oxide Etching & Metallization	HCL:H ₂ O (1:1) for 15 s & AuZn/Au (200 nm/ 200 nm)
14	Lift Off & annealing	Acetone (40 °C) for 10 m & 300°C for 20 s

Table 2. Detailed steps for fabrication of the solar cell device.

1)

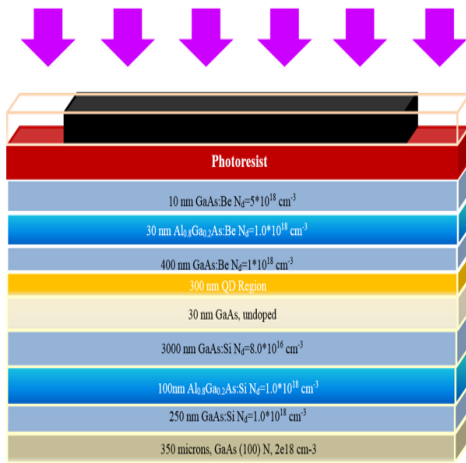


2)

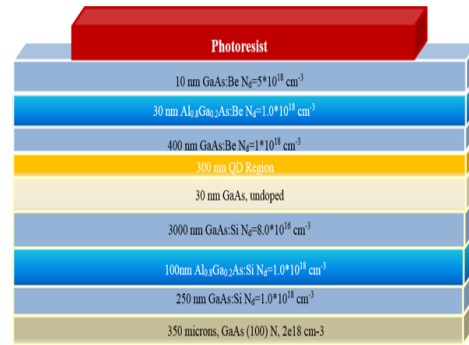


UV Light

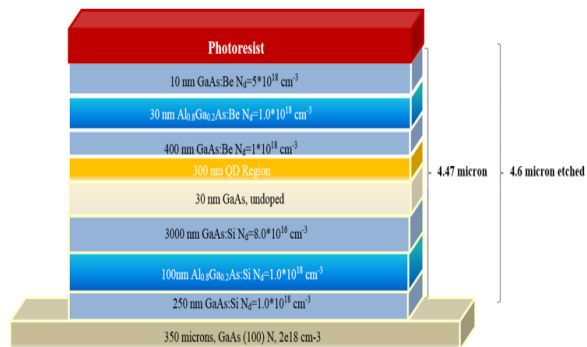
2)



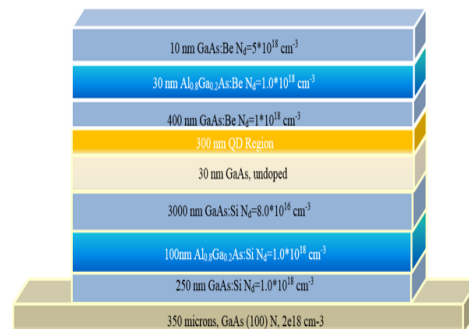
3)



4)



5)



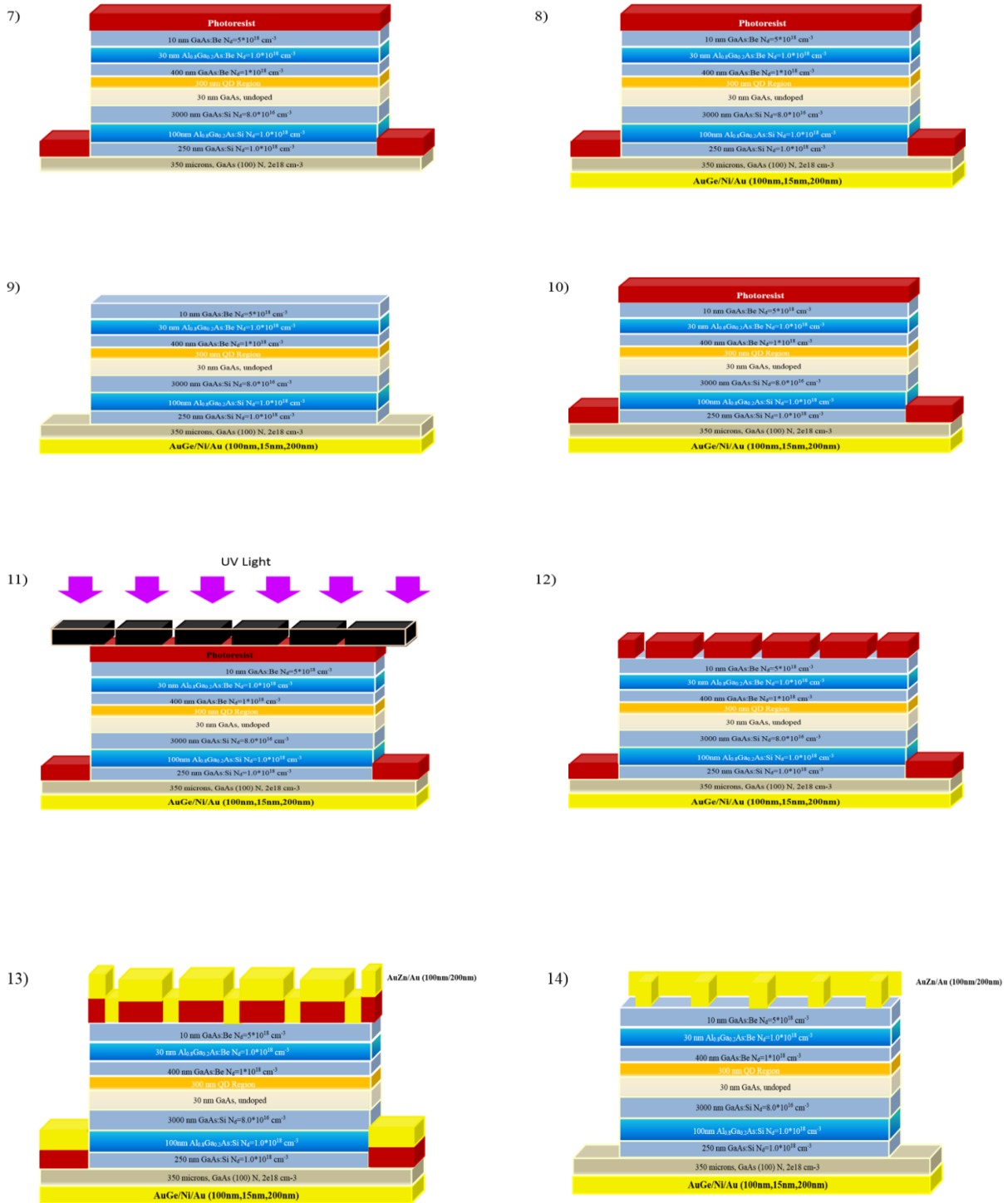


Figure 22. A schematic diagrams illustrating detailed photolithography processes used for solar cell structure fabrication.

3.3. Characterization

3.3.1. Material and Structural Characterization

3.3.1.1. Atomic Force Microscopy (AFM)

Atomic Force Microscopy is a valuable technique for characterizing the surface morphology of materials at the nanoscale. The working principle of AFM explains how this method can precisely scan the surface of the measured material. The material surface is scanned using a cantilever that contains a sharp tip. The curvature of the tip is very small (nanometer scale). Characterizing the material surfaces by AFM is used extensively due to the accuracy of the AFM tip movement along the top of the tested material surface. There are three basic modes of Atomic Force Microscopy: contact, non-contact, and tapping mode [72], [73], [74].

- **Contact Mode**

In this mode, the surface of the tested sample is scanned by the tip of the cantilever by coming in contact with the surface through a fluid layer on the sample surface. A photodiode detector is used to monitor the deflection of the cantilever during the scan. The disadvantage of using this method is that the force resulting from the tip-sample connection has a high possibility of damaging the surface of the tested sample. Other than damaging the sample surface, this method can also result in reduced imaging resolution [72], [74].

- **Non-Contact Mode**

In this mode, a sample surface is scanned without the tip being in contact with the sample surface, so it is called non-contact mode. However, during the scanning, the tip fluctuates on top of the fluid layer on the sample surface with a frequency higher than the resonance of the cantilever. Even though there is no force in this mode that is negatively affecting the sample

surface as in the contact mode, the sample surface can be affected by the fluid layer causing perversion of the surface morphology. Additionally, slow scan speeds and low resolution are some of the disadvantages of this mode, thereby limiting the applications of AFM non-contact mode [74], [72].

- Tapping Mode

The operation of the tapping mode combines the operations of contact and non-contact modes. In tapping mode, the sample surface is scanned by the tip with a cantilever oscillation amplitude of 20 to 100 nm. In the tapping mode, the tip is slightly touching the sample surface without affecting the surface morphology. The cantilever oscillation is maintained by a feedback loop to be constant, so the sample-tip interaction during scanning is preserved. Tapping mode has relatively more advantages than contact and non-contact modes by overcoming the measurement inaccuracy caused by the fluid layer, without causing surface damage or tip degradation. However, the AFM tapping mode scans have small errors that can be a result of the size and shape of the sharp tip. Also, noise is a factor that affects tapping mode scanning [72], [74]. Figure 23 shows a schematic diagram of the AFM tapping mode operation principle [72].

In the growth optimization phase, uncapped self-assembled InAs quantum dots were grown using the SK growth method. The purpose of these growths was to study and optimize the growth of quantum dots before embedding ten layers of them in the solar cell structure. Once the uncapped InAs were grown, AFM-Tapping mode was used to characterize and examine the growth of the quantum dots (see Table 3 for the AFM probe parameters).

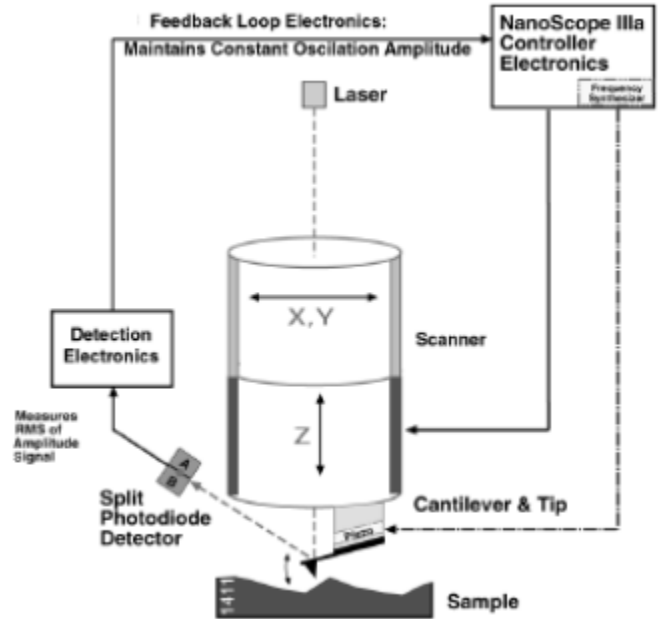


Figure 23. A schematic diagram of the AFM tapping mode operation [72].

AFM Probe parameters	
Tip curvature radius	10 nm
Cantilever resonance frequency	300Hz
Spring constant	37 N/m

Table 3. Summary of the AFM probe parameters.

3.3.1.2. Cross-Sectional Transmission Electron Microscopy (X-TEM)

Transmission Electron Microscopy is considered one of the best imaging techniques for a number of materials. High resolution and the capability of high magnification have allowed for broad TEM imaging applications in many fields, such as biological, medical, and material research. TEM images are produced using a different working principle to the optical microscope. Electrons are used in TEM instead of light. The images resolution of the TEM is

considerably higher than that of the optical microscope. Also, Transmission Electron Microscopy can provide images of objects with the size of a few Angstroms [75].

TEM is a valuable tool to study self-assembled quantum dot structures grown using SK growth. The optical and electronic properties of quantum dots can be accurately understood by knowing their precise parameters such as shape and size, and by studying the complex strain effect, which can be determined by TEM [75], [76].

Cross-Sectional TEM (X-TEM) can provide accurate data about the height and lateral dimensions of the quantum dots based on which section of the sample is viewed [75]. In this research, it is very important to show the true shape and height of the truncated InAs quantum dots. Moreover, since the quantum dot truncation technique involves high temperatures during annealing, it is very essential to do X-TEM to illustrate the effect of the rapid temperature ramps to truncated dots and the defect nucleation that might result after growing multiple layers of QDs. Figure 24 shows the FEI Titan 80-300 TEM instrument used in this research.



Figure 24. FEI Titan 80-300TEM instrument used in this research.

3.3.2. Optical Characterization

Photoluminescence (PL) measurement has been shown as a suitable technique for characterizing III-V semiconductors in general, and more specifically, quantum dot and intermediate band solar cells. In this technique, photo-excited carriers are generated by laser excitation when the semiconductor material absorbs photons with an energy larger than the material band gap. Subsequently, the carriers relax to a lower energy state, resulting in electron-hole recombination and photon emission. The PL measurement detects the radiative light resulting from the radiative electron-hole recombination. The energy level structure can be characterized using this method. The non-radiative recombination process is usually active at room temperature. PL measurements were performed at low temperatures to reduce the effect of lattice vibrations (phonons) [77], [78], [73].

Excitation is produced by shining an optical source on the sample. Typically, a laser source, with photon energy higher than the material band gap, is used. For example, a frequency-doubled, Nd: YAG Laser (Wavelength = 532 nm) can excite InAs/GaAs quantum dots IBSC samples resulting in the e-h recombination between the quantum dot discrete energy states. Therefore, the PL spectrum displays peaks, which then can be analyzed to understand the quantum dot states [79]. Figure 25 illustrates the setup used for low temperature (PL) and excitation power dependent photoluminescence measurements performed on the quantum dot intermediate band solar cell samples.

The setup contains a closed-cycle Helium optical cryostat that is capable of varying the temperature from 10 to 300 Kelvin. The distance between the stage where the sample is mounted and the window of the cryostat is less than 1 cm.

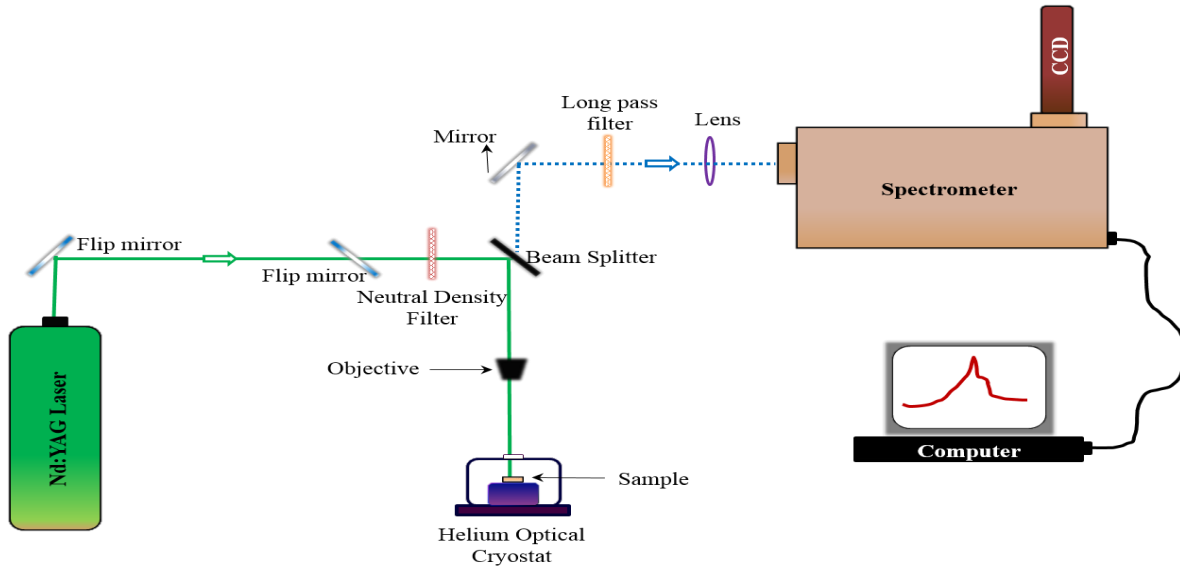


Figure 25. A schematic diagram of the experimental setup for PL measurement, modified from [79].

A frequency-doubled Nd:YAG Laser was used for QD and GaAs excitation. In the power excitation dependent measurement, neutral density filters were used. The optical intensities were varied from 0.03183 to 18581.8 W/cm². An objective was placed near the cryostat window to focus the incoming laser beam onto the sample. The laser beam spot size at the sample surface had a diameter of 20 microns and the light was collected by 50× objective.

PL measurements were performed on all of the QD samples in order to understand the quantum dot intermediate band's energy spectrum. Studying and understanding the energy spectrum of the quantum dots allows for understanding the photo-generated carriers' transport mechanism in the QD solar cell devices. To prove the concept of this project, it was important to do low temperature PL studies in order to prove the uniformity of the quantum dots.

Furthermore, the excitation power dependent measurement was performed in order to illustrate the existence of the excited states in the quantum dots.

3.3.3. Solar Cell Efficiency Studies

3.3.3.1. External Quantum Efficiency (EQE)

One of the most important solar cell characterization tools is the quantum efficiency (QE) measurement. QE measures the solar cell's sensitivity to the solar spectrum (spectral response) by measuring the efficiency of the device at different wavelengths and characterizing the efficiency of the solar cell. EQE measurements are used to examine different cell materials and structures [80], [81].

The quantum efficiency (QE) of a solar cell can be calculated by knowing the number of charge carriers that the solar cell collected and the number of the incident photons on the solar cell of a specific energy, thereby indicating the amount of current that a measured solar cell can produce. Photons with energies less than the energy of the material band gap produce a quantum efficiency of zero [3]. By plotting the QE of a solar cell as a function of wavelength, information about how effective the solar cell is at converting light to current at different wavelengths can be explored. From that, wavelengths at which the photovoltaic device is efficiently converting light and where there is room for improvement can be quickly visualized [80].

There are two types of quantum efficiency measurements: external quantum efficiency (EQE) and internal quantum efficiency (IQE). External quantum efficiency is the ratio of the number of collected electrons per second to the number of incident photons per second on the solar cell, and depends on external factors from the diode, such as reflection, and is given by Equation 4.

$$EQE = \frac{\# \text{ of collected electrons/sec}}{\# \text{ of incident photons/sec}} \times 100 \quad (4)$$

However, internal quantum efficiency is defined as the ratio of the collected electrons per second to the absorbed incident photons per second, so the IQE is only affected by the junction [80], [3], [82] and is given by Equation 5.

$$IQE = \frac{\# \text{ of collected electrons/sec}}{\# \text{ of absorbed photons/sec}} \times 100 \quad (5)$$

By knowing the external quantum efficiency, the solar cell internal quantum efficiency can be calculated as, Equation 6 [83].

$$IQE = \frac{EQE}{1 - \text{spectral Reflection} - \text{device transmission}} \quad (6)$$

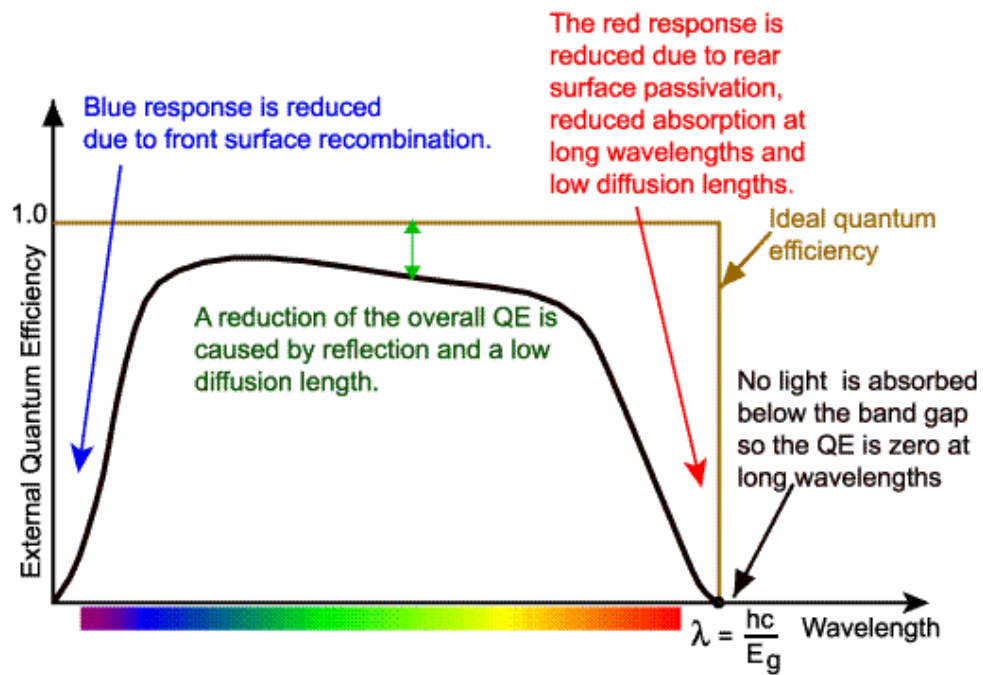


Figure 26. The ideal external quantum efficiency curve and the mechanisms behind EQE reduction [84].

The ideal quantum efficiency for a solar cell has a square curve, as shown in Figure 26. However, most solar cells are affected by recombination mechanisms, and thus their quantum

efficiency is reduced. The reduction in the quantum efficiency can be a result of the front surface recombination, reflection, low diffusion length, and reduced absorption at long wavelengths [84].

There are several steps involved in the operation of quantum efficiency system. First, a xenon arc lamp is used to provide a broad band white light. The light coming from the lamp is collected by an ellipsoidal reflector and focused onto the entrance slit of the monochromator. After that, the monochromator and the filter wheel select a particular wavelength of light. Subsequently, the filter wheel introduces a suitable wavelength filter to the beam path to reduce stray light. The light passing through the filter is then split by a beam splitter, and a portion of the light is deviated to the monitor photodiode through a lens. Then, the beam converges by a concave mirror. The tested solar cell device is located at the focal point of the beam. The signal generated by the solar cell device is then amplified and applied to the processor of a digital signal [80]. The optical setup of the EQE system is shown in Figure 27.

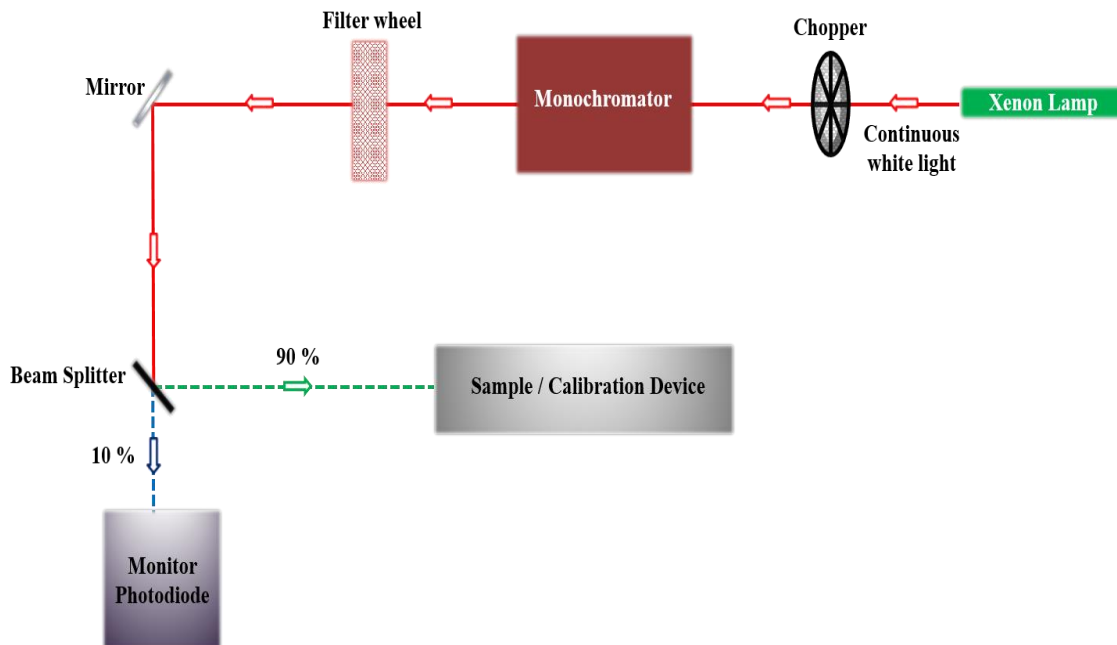


Figure 27. A schematic diagram of the optical setup of the EQE system.

Before each measurement, the EQE system is calibrated. A calibrated reference device is required for the external quantum efficiency measurements. The calibration of the EQE system is very important since the quantum efficiency measurement of the solar cell-under-test is compared to the response of a calibrated silicon photodiode/germanium photodiode. For QD IBSC EQE measurements, a silicon photodiode was used. This photodiode was calibrated at the National Institute of Standard and Technology (NIST), typically I755. The transfer uncertainty of the silicon diode is very small. It is less than 0.5% for wavelengths in the range of 400 to 1000 nm, and it is less than 1% for other wavelengths [80]. The calibration of the system was done for wavelengths ranging from 300 to 1100 nm in steps of 5 nm. The EQE system calculates the quantum efficiency of the cell-under-test using Equation 7.

$$QE_{\text{test}} = \frac{I_{\text{test}}}{I_{\text{cal}}} QE_{\text{cal}} \quad (7)$$

where QE_{test} is the measured quantum efficiency of the tested solar cell, I_{test} is the measured current of the tested solar cell, I_{cal} is the measured current of the calibrated silicon photodiode, and QE_{cal} is the calibrated quantum efficiency of the calibrated silicon photodiode.

External quantum efficiency measurements at room temperature and at variable temperatures have been performed for all samples. The external quantum efficiency is measured for wavelengths ranging from 300 to 1100 nm in increments of 5 nm, with lamp power being 65 W, and the voltage bias equal to zero. Figure 28 shows the EQE system used in this research.



Figure 28. QEX10 Quantum Efficiency Measurement System, Inc.

3.3.3.2. Maximum Solar Cell Efficiency Conversion (SE)

The solar cell efficiency measurement is one of the most important characterization techniques to evaluate the solar cell performance and to find the maximum solar cell efficiency conversion. It is a popular and standard technique for comparing efficiencies of different solar cell devices with different materials and designs. Air mass of 1.5 spectrum (AM 1.5) and intensity of 100 mW/cm^2 (one-sun illumination) is considered a standard for solar cell efficiency testing [5].

The ratio between the maximum power generated by the solar cell and the incident power defines the conversion efficiency of a solar cell device and can be found by current-voltage measurement performed on the solar cell device, represented by Equation 8 [5].

$$\eta = P_{out} / P_{in} \quad (8)$$

where P_{out} is the maximum power generated by the solar cell, and P_{in} is the incident power on the solar cell. If the illumination on the solar cell is uniform, the solar efficiency conversion is expressed by Equation 9 [25].

$$\eta = (V I)_{max} / \text{Light intensity} \cdot A_{cell} \quad (9)$$

Therefore, knowing the maximum voltage (V_{max}) and current (I_{max}) generated by the cell, the lamp intensity (which in this case is calibrated to 100 mW/cm^2) and the solar cell active area A_{cell} , we can calculate the maximum solar conversion efficiency [5].

The solar efficiency measurement can also provide information about the open circuit voltage (V_{oc}) and short circuit current (I_{sc}) of the cell under-test, which can be extracted directly from the dark and illuminated I-V curves. A schematic graph of solar I-V characteristics, showing the diode dark current and the increase of diode current under illumination can be seen in Figure 29. The filling factor, which is a measure of the solar cell device quality corresponding to the largest rectangle of the current-voltage curve, can be calculated using Equation 10 [2].

$$FF = (V I)_{max} / V_{oc} I_{sc} \quad (10)$$

Figure 30 shows a schematic diagram of the solar efficiency measurement setup. The PV measurements Small Area Solar Simulator in the lab has the ability to test solar cells with a diameter up to 1 cm. Using a custom filter and tungsten lamp, the light intensity and spectrum generated in this system is comparable to the sun light. The spectrum matches the Global reference spectrum (ASTM G 173) AM 1.5. The power to the lamp, fan, and shutter in the solar simulator is provided by B&K Precision 1665 DC Regulated power supply.

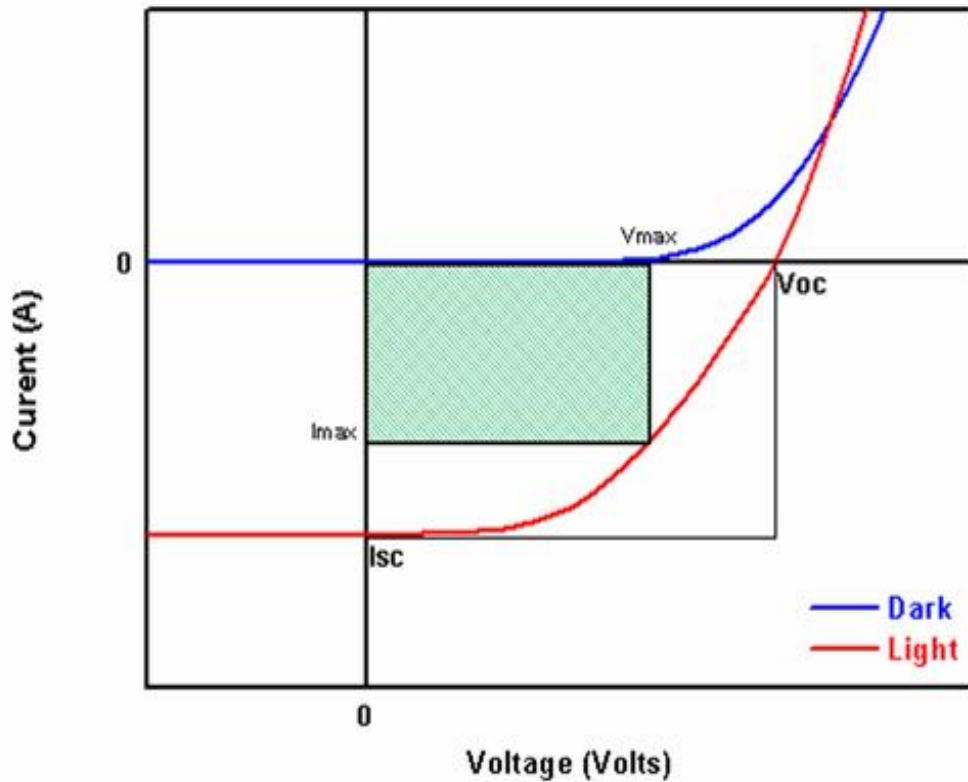


Figure 29. A schematic graph of solar I-V characteristics, showing diode dark current and the increase of diode current under illumination.

The irradiance is equal to 100 mW/cm^2 with stability better than $\pm 1\%$ in one hour and a non-uniformity of $\pm 5.0\%$ for solar cells with a diameter of 1 cm. The beam of the light focused on the sample under-test has a diameter of ~ 7 cm. However, for accurate solar efficiency results, the sample under-test should be placed in an area parallel to the center of the beam because the 1 cm round region of the beam has the highest light uniformity [85].

Before measuring each sample, the current under short circuit bias conditions was examined with the SMU from Keithley while moving the test device around the central area of the beam to find the maximum current value, where the center of the tested cell active area matched the center of the beam.

For the best spectral performance, the power supply voltage was set to be 13.36 V with a current of 4.65 A, as found from system calibration on May 24, 2013. System calibration was done using Reference Silicon Solar Cell provided by PV Measurements, Inc.

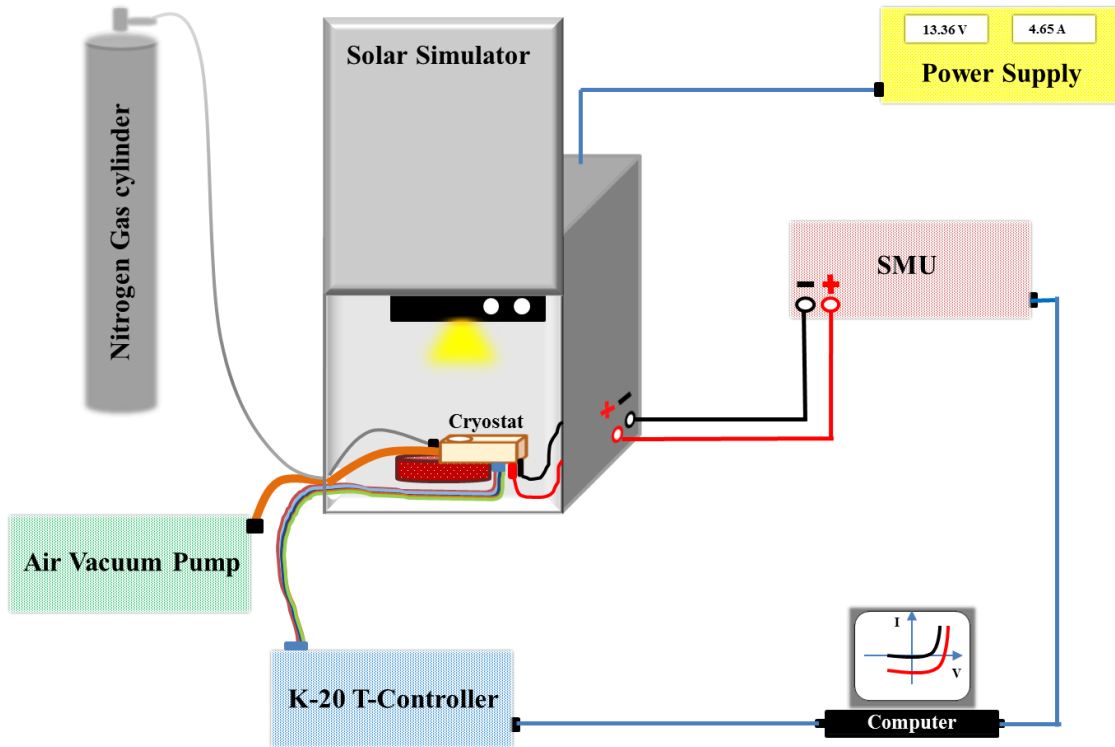


Figure 30. A schematic diagram of the solar efficiency measurement setup.

The solar efficiency measurement has been done on all samples at room temperature. Also, temperature dependent solar efficiency measurements were performed. During the temperature dependent measurements, temperature was controlled using a K-20 Programmable Temperature Controller. The Cryostat used is an MMR D2500 which is capable of varying the temperature from 80-400 K. Figure 31 illustrates the PV Measurements Small Area Solar Simulator at the University of Arkansas.

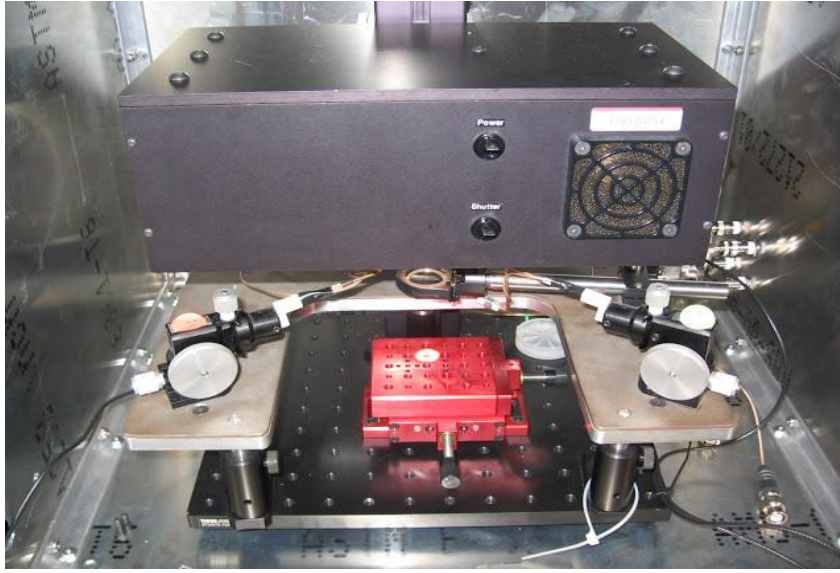


Figure 31. The PV Measurements Small Area Solar Simulator.

3.3.4. Electrical Characterization

The Shockley equation expressing the shape of the I-V curve is represented by Equation 11 [82].

$$J_d = J_0 \left\{ \exp \left[\frac{V}{V_t} \right] - 1 \right\} \quad (11)$$

J_d and J_0 are the current density measured in dark condition and the density of reverse saturation current, respectively. V and V_t are the applied voltage and the thermal voltage, respectively. The thermal voltage is expressed by $V_t = q/KT$, which is equal to 0.0259 V at room temperature. Since this expression assumes no recombination occurs, it shows the ideal solar cell behavior with an ideality factor equal to 1, under dark condition [86].

The ideality factor (n), which can be calculated by knowing the dark I-V slope, is considered a robust way to identify the non-radiative recombination mechanism. When the diode ideality factor value is equal to 1, the dominate recombination in the neutral regions is

represented by the minority carriers, which represent the theoretical ideal diode characteristics. However, when the value of the diode ideality factor is equal to 2 or higher, the high recombination rate is dominated by both majority and minority carriers. An ideality factor equal to 2 or 3 represents Auger and SRH recombinations contributing to filling factor and open circuit voltage degradation [21]. By measuring I-V and analyzing the carrier recombination mechanisms using the model of single diode expressed by Equation 12, the fundamental physics of the degradation of open circuit voltage in IBSC can be explored [87] [86].

$$J_d = J_0 \left\{ \exp \left[\frac{V}{n(V) V_t} \right] - 1 \right\} \quad (12)$$

The current of the solar cell device under illumination is expressed by Equation 13.

$$J_{d=} [J_0 \left\{ \exp \left[\frac{V}{n(V) V_t} \right] - 1 \right\}] - J_L \quad (13)$$

Solar cell device design involves a series resistance (R_s). The series resistance can be a result of several layers of solar cell design, resistance between the front contact and front device surface, and the resistance between the back contact and the back of the device surface [82]. The total diode current measured passing through a series resistance is expressed in Equation 14.

$$J_d = J_0 \left\{ \exp \left[\frac{V - J R_s}{n(V) V_t} \right] - 1 \right\} \quad (14)$$

When the saturation current is very small compared to the measured current and the background radiation is negligible, the ideality factor (n) can be calculated using Equation 15 [87] [86].

$$n(V) = \frac{d \left(\frac{V}{V_t} \right)}{d [\ln(I)]} \quad (15)$$

In order to identify the reason for the efficiency degradation of the quantum dot intermediate band solar cell, detailed current-voltage measurement in forward and reverse biases have to be done. This helps to distinguish between surface and bulk phenomena, understand carrier transport, and classify generation and recombination centers. All samples were measured at room temperature. Figure 32 illustrates the equipment used for I-V measurements.



Figure 32. Current-Voltage measurement setup.

Chapter 4: Results and Discussion

4.1. Material and Structural Characterization (Cross-Sectional TEM)

Cross-Sectional Transmission Electron Microscopy measurements have been done on the quantum dot samples SF2, SF3, SF4, SF5, and SF7. Cross-Sectional TEM is essential to study the growth quality of the layers and interfaces. A single InAs quantum dot with a high growth quality is illustrated in Figure 33-a. In addition, the cross sectional TEM image of the quantum dot intermediate band solar cells is shown in Figure 33-b. This image shows the barrier layer (100 nm of $\text{Al}_{0.8}\text{Ga}_{0.2}\text{As}$: Si, $N_D = 1 \times 10^{18} \text{ cm}^{-3}$), which appears as a thick bright layer on a dark background. Also, image 31-b shows the device's active area consisting of 10 layers of InAs quantum dots. These images demonstrate high quality epitaxial growth of the layers and interfaces.

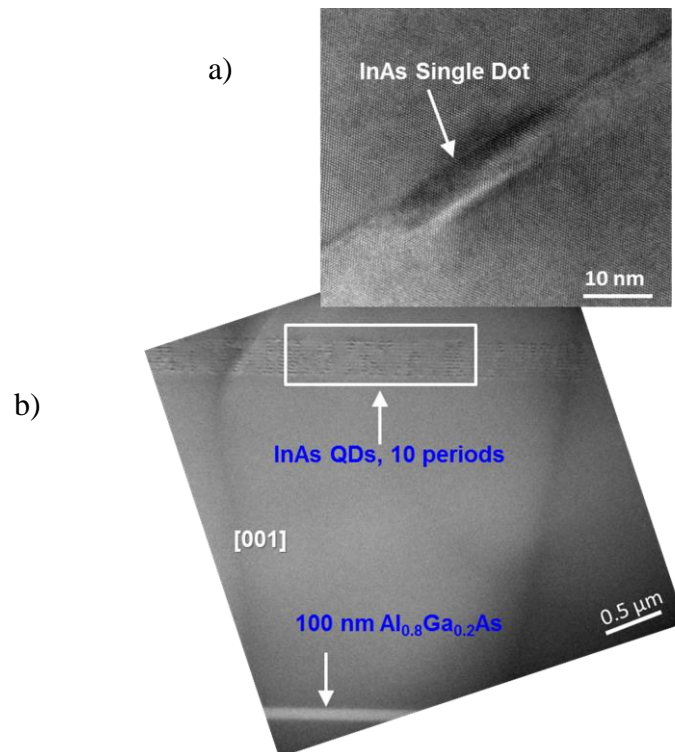


Figure 33. a) TEM image of a single InAs quantum dot for sample SF7 (7 nm GaAs cap) b) TEM image of the entire QD IBSC growth structure QDs.

The probability of creating defects is high for quantum dots created using the strain driven SK growth method [88]. TEM images of the region with 10 layers of quantum dots were essential to see the effect that might result from the strain driven SK growth and the temperature ramps during truncation and annealing. An enlarged TEM image of the 10 periods of 5 nm QDs is shown in Figure 34. The quantum dot regions of the grown samples have a high structural growth quality showing no dislocations or defects in the TEM images. The grown quantum dots are not perfectly aligned as was anticipated, due to the thick 30 nm GaAs spacer. Figure 34 represents the TEM image of the 5 nm quantum dots stacks in sample SF5.

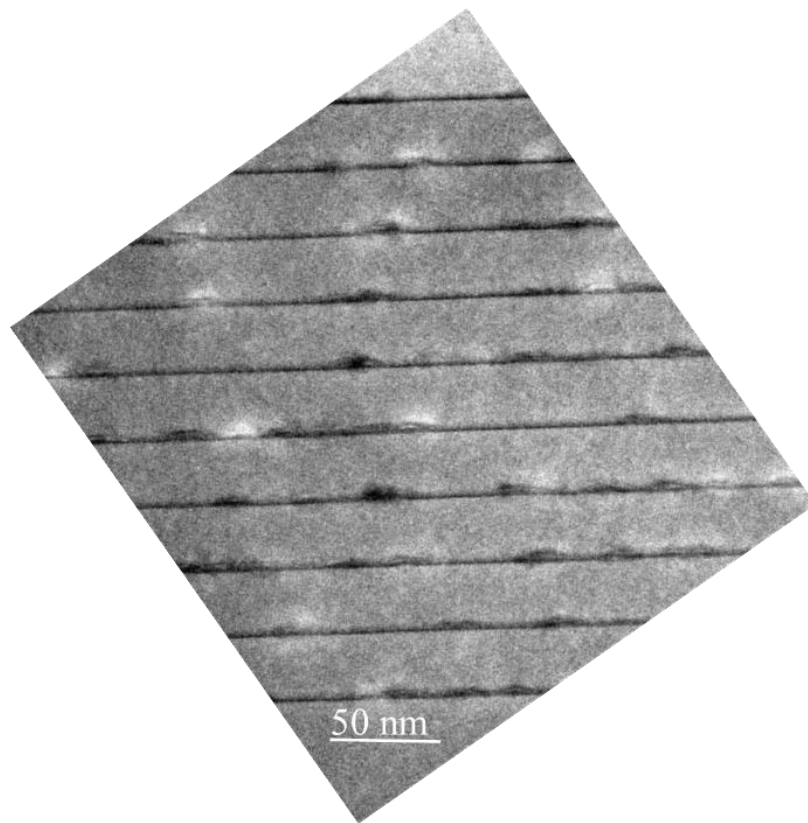


Figure 34. TEM image of sample SF5 with 5 nm coverage showing the 10 layers of QDs.

The height of the InAs quantum dots for each sample has been analyzed and a single QD is shown in Figure 35 as images a, b, c, d, and e for samples SF2, SF3, SF4, SF5, and SF7, respectively. The average heights of the grown quantum dots are: SF2 = 2.5 nm, SF3 = 3.1 nm, SF4 = 4.3 nm, and SF5 = 5.1 nm, which is close to the targeted quantum dot heights. However, the average size of the quantum dot in sample SF7 is 5.3 nm instead of the intended 7 nm. This means that the height of the 2ML InAs quantum dots as grown is ~ 5 nm, so the 7 nm GaAs capping layer had no effect. Table 4 summarizes the targeted and achieved QD heights.

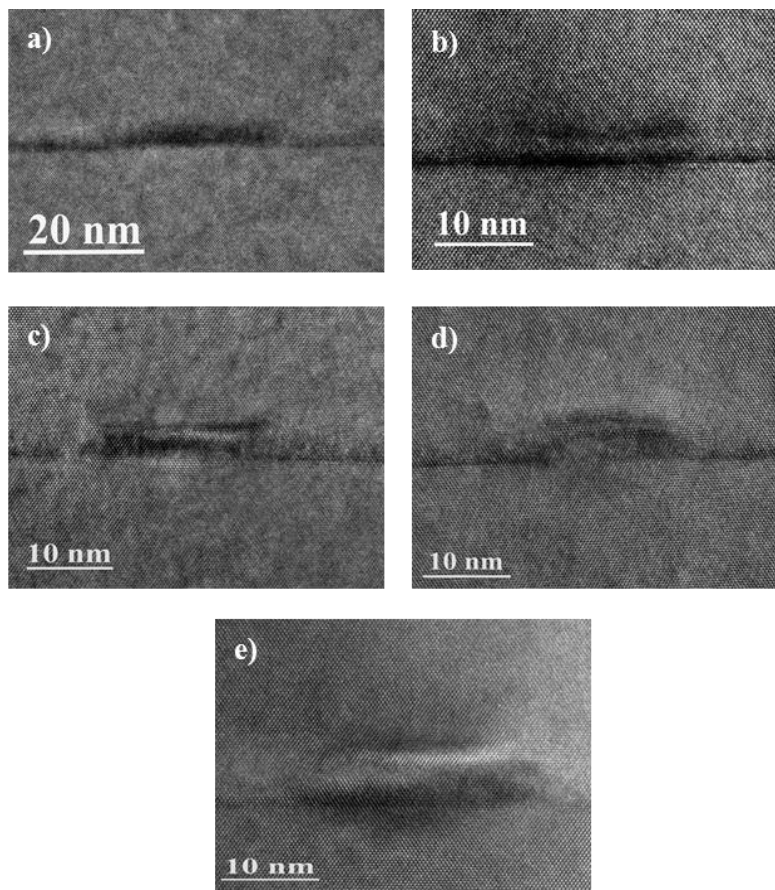


Figure 35. TEM images for (a) SF2 sample with 2 nm coverage, (b) SF3 sample with 3 nm coverage, (c) SF4 sample with 4 nm coverage, (d) SF5 sample with 5 nm coverage, and (e) SF7 sample with 7 nm coverage.

Image label	Targeted QD sizes	Average QD sizes
a	2	2.5
b	3	3.1
c	4	4.3
d	5	5.1
e	7	5.3

Table 4. Targeted and achieved quantum dot heights.

In summary of this section, the TEM images show quality layers and interfaces of the grown solar cell structures. Furthermore, the quantum dot height analysis of the quantum dots with different GaAs capping thickness of 2, 3, 4, and 5 nm demonstrates quantum dot heights of 2.5, 3.1, 4.3, and 5.1 nm, respectively. The measured heights are close to the targeted quantum dots heights for samples SF2, SF3, SF4, SF5. However, the result of the quantum dot analysis demonstrates that the measured 7 nm capped quantum dot height is 5.3 nm, indicating that the height of the quantum dots before truncation is ~ 5 nm.

4.2. Optical Characterization

In addition to the Cross-Sectional TEM measurements, a low temperature photoluminescence study has been performed on samples SF2, SF3, SF4, SF5, and SF7. The measurements were performed at 10 K, with a laser excitation wavelength of 532 nm, and a power intensity of 20 mW/cm^2 and 1 mW/cm^2 . Figure 36 shows normalized photoluminescence spectra for all samples, labeled according to QD size of 2.5, 3.1, 4.3, 5.1, and 5.3 nm.

Since the effective band gap between the InAs ground states increases with the decrease of the quantum dot size, the change in the position of the PL peak in Figure 36 is an indicator of the quantum dot size variation in samples SF2, SF3, SF4, and SF5, which can be seen as a blue shift of the representative PL peaks with the decrease of quantum dot height. Figure 36 also illustrates an insignificant difference in the position of the PL peaks of 5.3 nm (SF7) and 5 nm (SF5) GaAs capped quantum dot samples. This implies that there is a negligible difference between the sizes of the quantum dots in the two samples, as measured in the Cross-Sectional TEM studies.

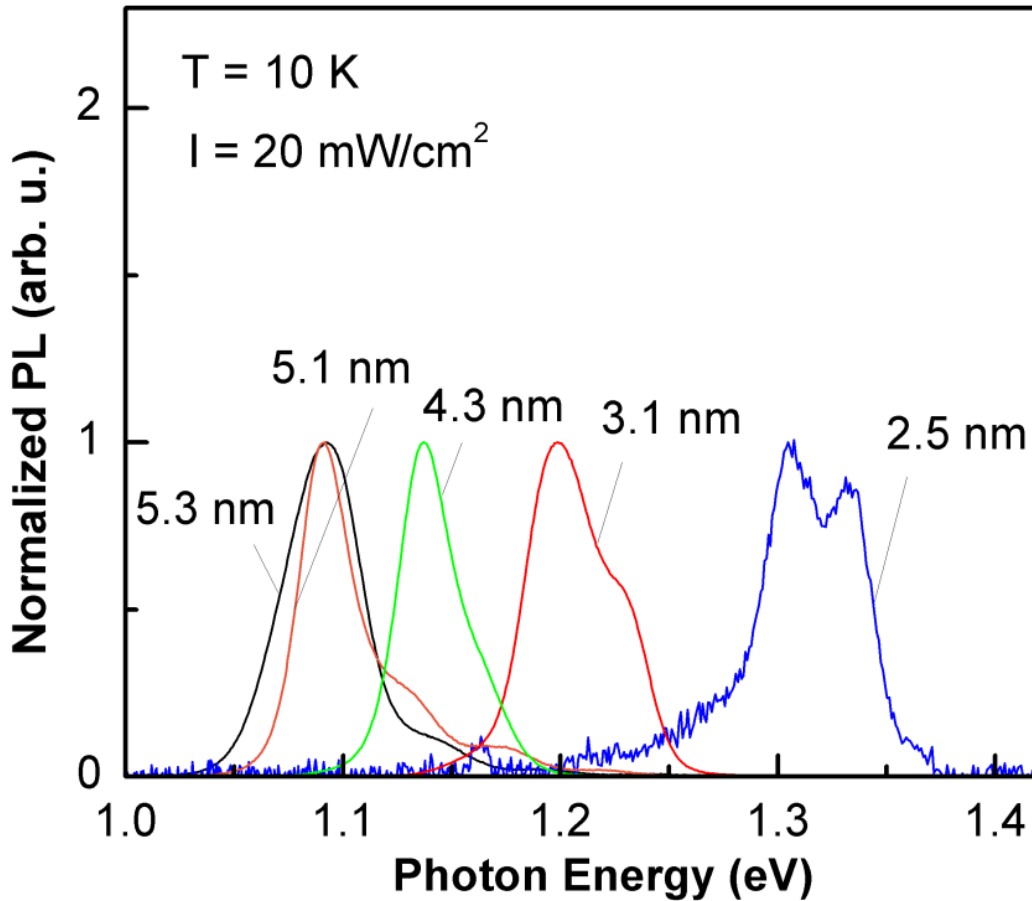


Figure 36. Normalized PL spectra of 2 nm, 3 nm, 4 nm, 5 nm, and 7 nm GaAs cap QD IBSCs samples.

Figure 36 also demonstrates the QD size distribution for samples SF2, SF3, SF4, SF5, and SF7. Additional peaks are measured at higher energies of the PL spectra for all the QD samples. The additional peaks detected are found at energies of $E_{2.5} = 1.34$ eV, $E_{3.1} = 1.23$ eV, $E_{4.2} = 1.17$ eV, $E_{5.1} = 1.14$ eV, $E_{5.1} = 1.17$ eV, $E_{5.3} = 1.14$ eV. To further understand the QD size distribution and investigate the origin of the additional peaks at higher energy, PL power dependent measurements at low temperature (10 K) and power intensity variation of 0.03183-18581.8 W/cm² were performed.

To highlight the additional peaks in the PL power dependent measurement, the normalization of all spectra with respect to the maximum of the quantum dot ground state photoluminescence peak was performed. In the PL excitation power dependent measurement, the optical transition that represents the wetting layer was found to be at $E_{WL,e-hh} = 1.435$ eV. Figure 37, 38, 39, 40, and 41 show the PL excitation power dependent measurements for 2.5, 3.1, 4.3, 5.1 and 5.3 nm QD samples, respectively, which clearly demonstrates the existence of excited states in the confined QDs at a laser excitation of 17.9658 W/cm² and above.

The PL power dependent measurements show that extra peaks detected at higher photon energies shown in Figure 36 for each PL spectrum represent the excited states of the quantum dots. However, the peak appearing at higher energy of the PL spectra of the 2.5 nm quantum dot sample indicates a different size distribution, which is a consequence of InAs QD height fluctuation during the shallow quantum dot truncation and annealing [89].

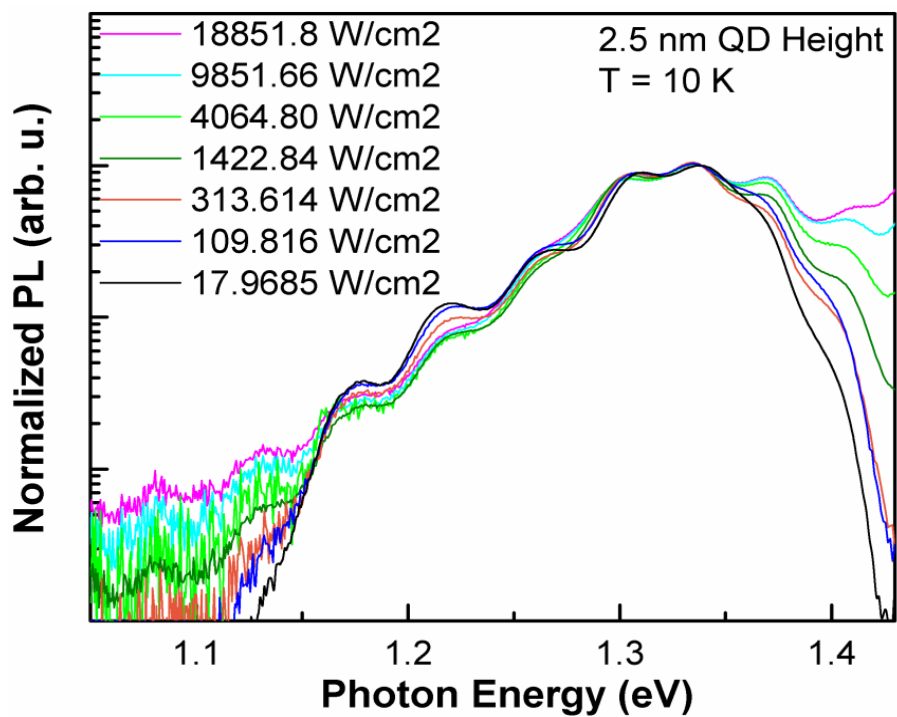


Figure 37. PL spectra for different excitation intensities measured at 10 K for sample SF2.

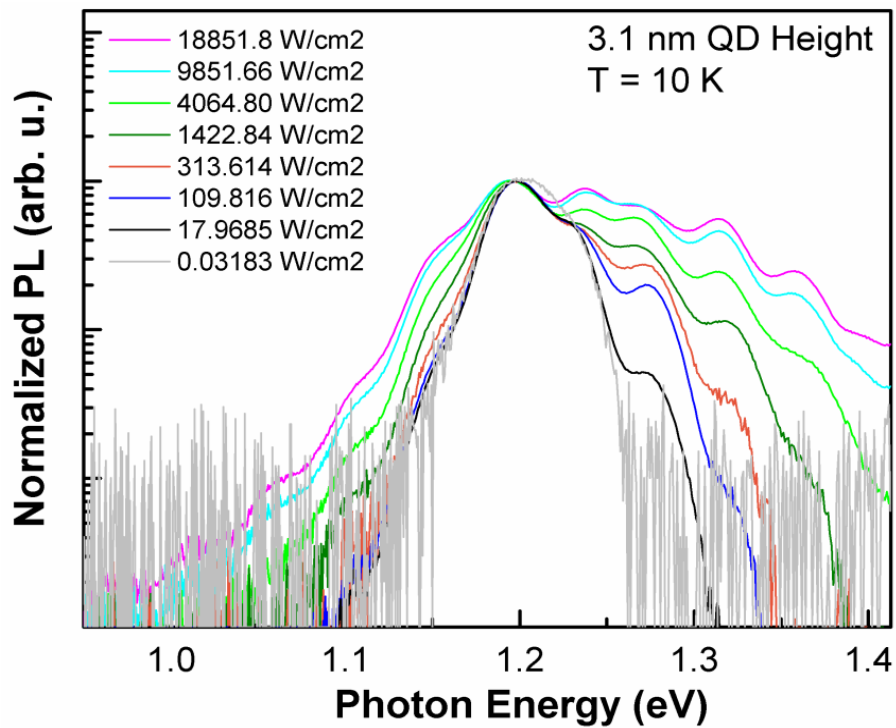


Figure 38. PL spectra for different excitation intensities measured at 10 K for sample SF3.

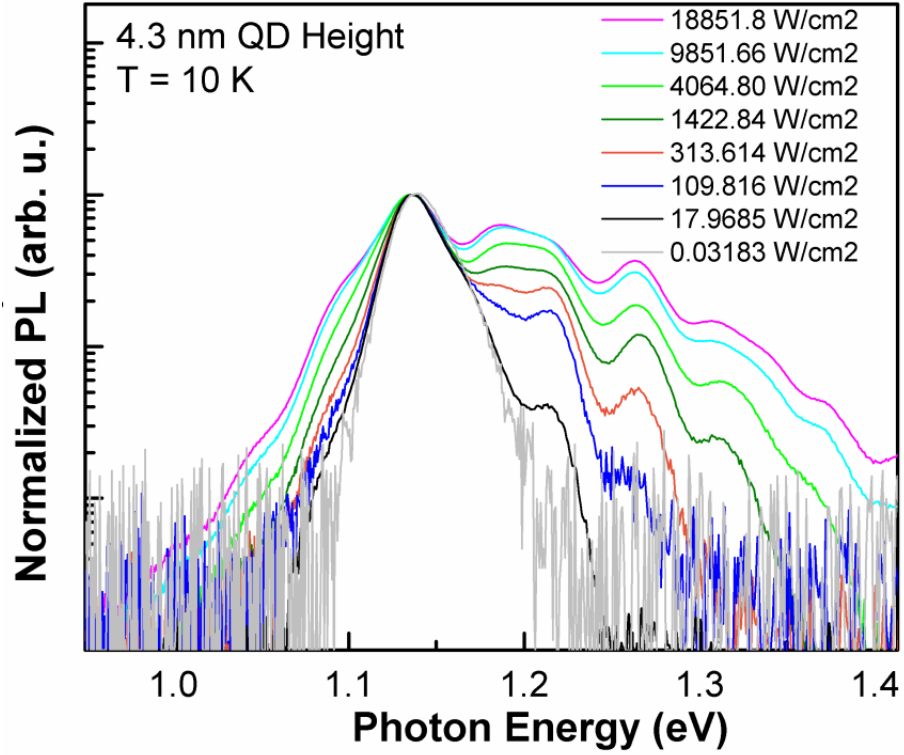


Figure 39. PL spectra for different excitation intensities measured at 10 K for sample SF4.

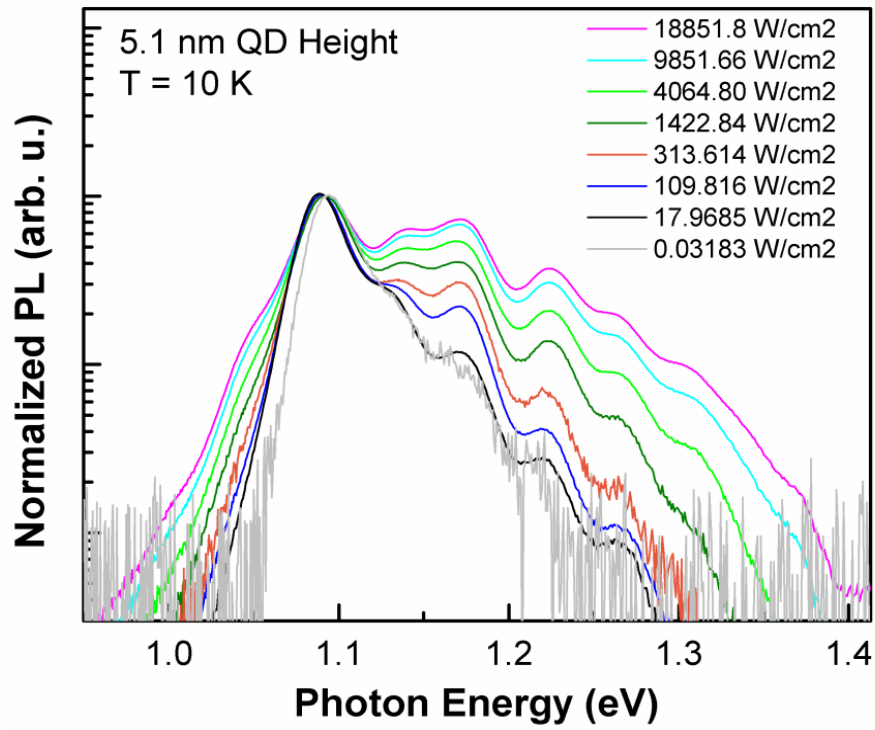


Figure 40. PL spectra for different excitation intensities measured at 10 K for sample SF5.

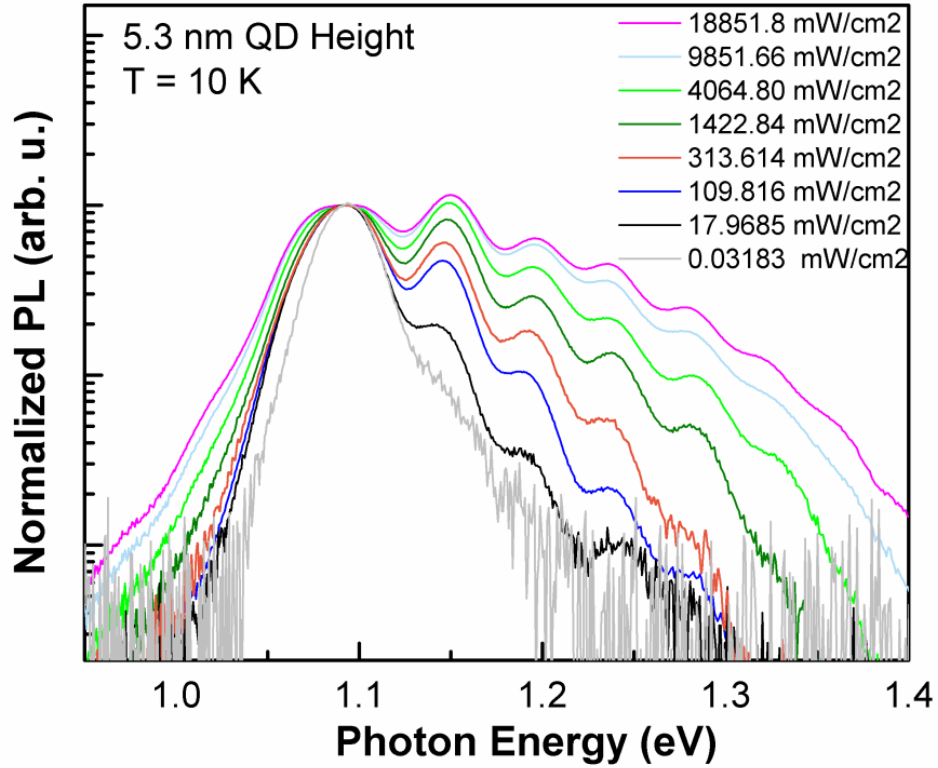


Figure 41. PL spectra for different excitation intensities measured at 10 K for sample SF7.

To confirm the bi-modal size distribution for the 2 nm QD sample and single size distribution for other QD samples, PL measurements were performed at very low power excitation intensity of 1 mW/cm^2 . The results of these measurements are shown in Figure 42. Samples SF3, SF4, SF5, and SF7 show a good fit by a single Gaussian, whereas, the PL spectra of sample SF2 shows a distinctive double-peak feature.

A significant reduction in the photoluminescence intensity correlated with the decrease of quantum dot height is also represented in Figure 42. The position of the CB ground states in small QDs is higher and closer to the GaAs barrier state. Thus, the probability of carrier escape from the small quantum dots into GaAs spacer layers is higher. This explains the decrease of PL intensity with QD height decrease [90].

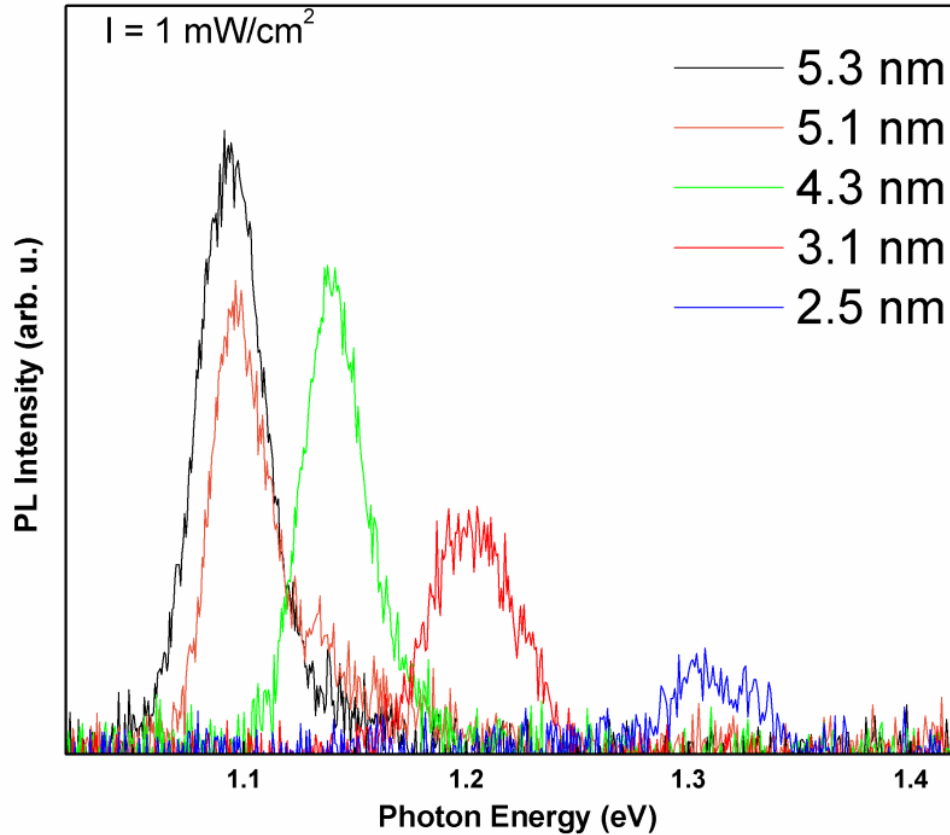


Figure 42. PL spectra of 2 nm, 3 nm , 4 nm, 5nm, and 7 nm GaAs cap QD IBSCs samples at low power intensity of 1 mW/cm^2 .

In summary, the change in the position of the PL peak was an indicator of the variation in quantum dots sizes. The PL peak was shifted toward higher photon energy with the decrease of quantum dot height, which agrees with the TEM results. However, QDs truncated by GaAs capping layers of 5 nm and 7 nm show a negligible shift in PL peak positions, meaning that SF5 and SF7 have insignificant height differences. The growth of small GaAs coverage, truncation, and annealing resulted in a QD height fluctuation and double-peak features in the 2.5 nm quantum dot IBSC. Also, carrier escape in the small quantum dots resulted in a significant reduction in the photoluminescence peak compared to large quantum dots. Furthermore, excitation power dependent measurements were performed and illustrate the existence of excited states in the quantum dots.

4.3. Efficiency Studies

4.3.1. External Quantum Efficiency (EQE)

External quantum efficiency studies have been done on all of the samples. Figure 43 shows the measured external quantum efficiency (EQE) as a function of the incident photon energy of the reference sample SF0 and the InAs quantum dot intermediate band solar cell samples SF2, SF3, SF4, and SF5. The measurements have been done at room temperature ($T = 300$ K) and for bias voltage of $V = 0$ V (Short Circuit Current Bias Condition).

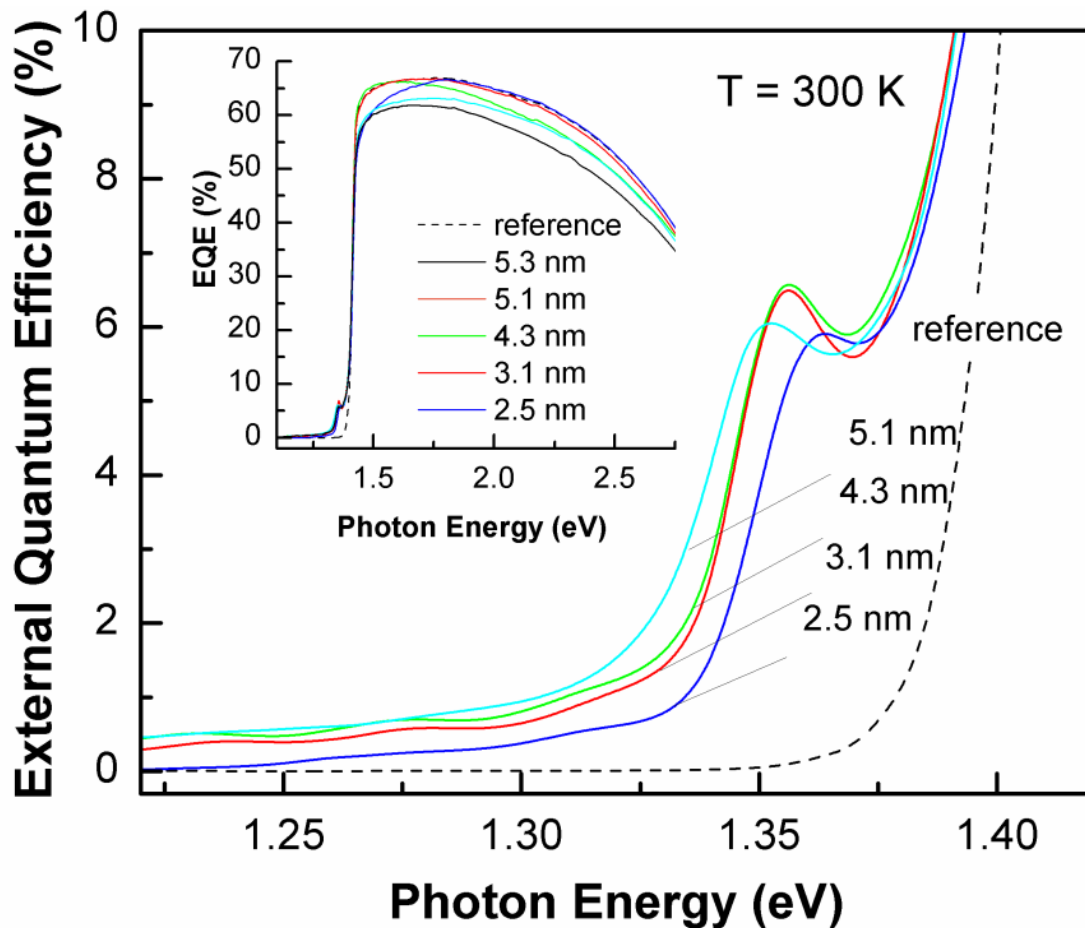


Figure 43. EQE versus incident photon energy for all samples.

The dotted line represents the EQE of the GaAs solar cell reference sample (SF0). The response of a supplementary band is presented below the GaAs band gap ($E_{g,Ga} = 1.42$ eV) for the quantum dot IBSCs. The light absorption resulting from the wetting layer that is intrinsic to SK growth and the quantum dot states is the reason for the photocurrent band below the GaAs band edge. As expected, a clear change in the position of the band edge, resulting from carrier confinement, indicates the quantum dot size variation in samples SF2, SF3, SF4, and SF5. This is in a good agreement with the PL data represented in Figure 36, where a red shift of the representative PL peaks can be observed with the increase of quantum dot height.

EQE efficiency in the IR range of the spectrum is enhanced in the QD IBSCs devices due to QD IB absorption. The supplementary photon absorption from the VB to the quantum dot states has enhanced the EQE in the QD samples SF2, SF3, SF4, and SF5 by ~6%. Also, a 67% EQE is measured due to photon absorption from the GaAs VB to GaAs CB. At room temperature, a quantum efficiency larger than 50% is a good indicator of minimal influence of defect and surface states [91].

As anticipated, the EQE of the reference sample SF0 peaks at the band gap of GaAs (1.42 eV) and the EQE of the QD samples peak at ~ 1.34 eV, representing the photocurrent resulting from the wetting layer states introduced by SK Growth. However, some additional peaks are presented below 1.33 eV. Supplementary analysis and measurement has been done to further understand the additional peaks. Derivative analysis of the EQE spectrum and low temperature (10 K) PL excitation power dependent measurements were performed.

Some loss in the external quantum efficiency on the GaAs side of the EQE spectrum was measured and attributed to higher defect densities for the devices with large quantum dots (~4.3 nm ~5.1 nm and ~ 5.3 nm). For the samples with smaller QD heights, the external quantum efficiencies are comparable to the reference sample without InAs quantum dots. Figure 44 shows the EQE loss of larger quantum dots at photon energy equal to 1.8 eV.

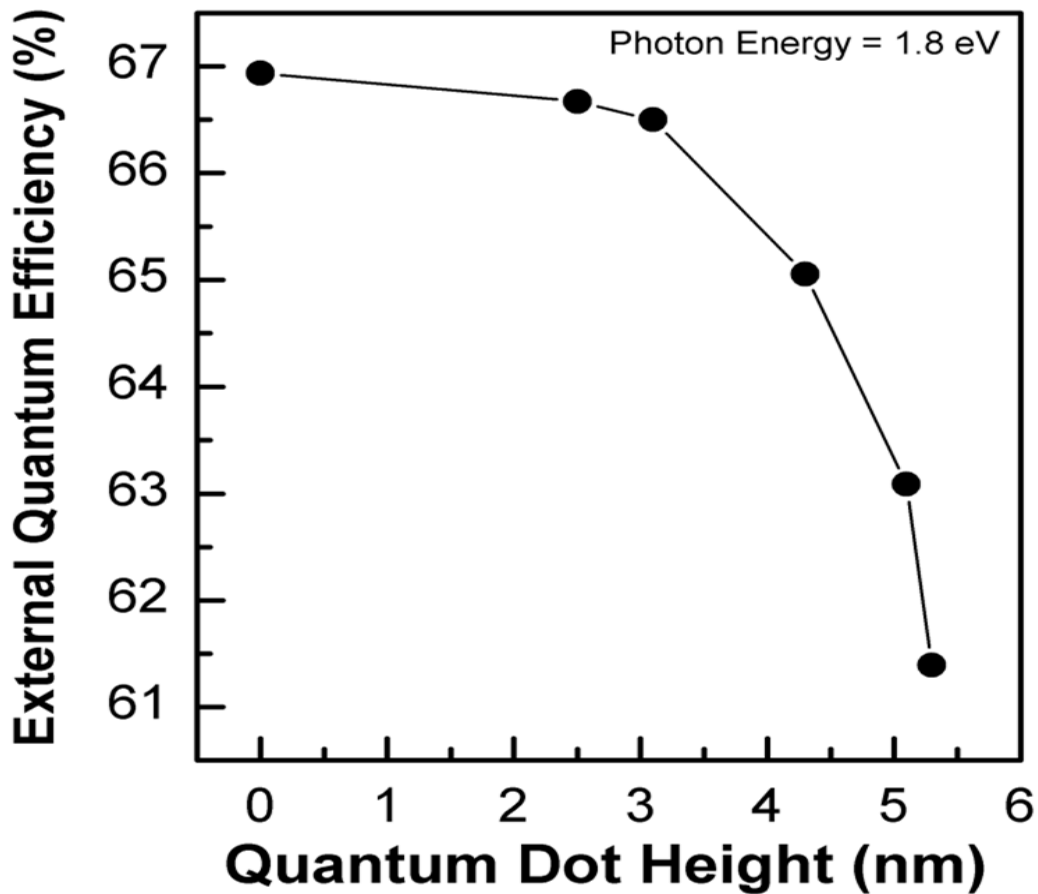


Figure 44. The decrease of EQE spectra in the GaAs region, indicating a loss of photocurrent at photon energy = 1.8 eV.

The result of the EQE spectrum derivative analysis for sample SF2, which corresponds to the 2.5 nm QD IBSC device, is summarized in Figure 45. The peaks that correspond to the photocurrent resulting from the optical transition below the GaAs band gap (measured at $E_{GaAs} = 1.41$ eV) and the wetting layer (measured at $E_{WL} = 1.34$ eV) are found to be at energies $E_1 = 1.22$ eV, $E_2 = 1.25$ eV, $E_3 = 1.28$ eV. Also, in Figure 37, the excitation power dependent PL measurement shows optical transitions between the excited states of the 2.5 nm QD sample measured at $E_{e1-hh1} = 1.33$ eV, $E_{e2-hh2} = 1.37$ eV, and $E_{e3-hh3} = 1.41$ eV.

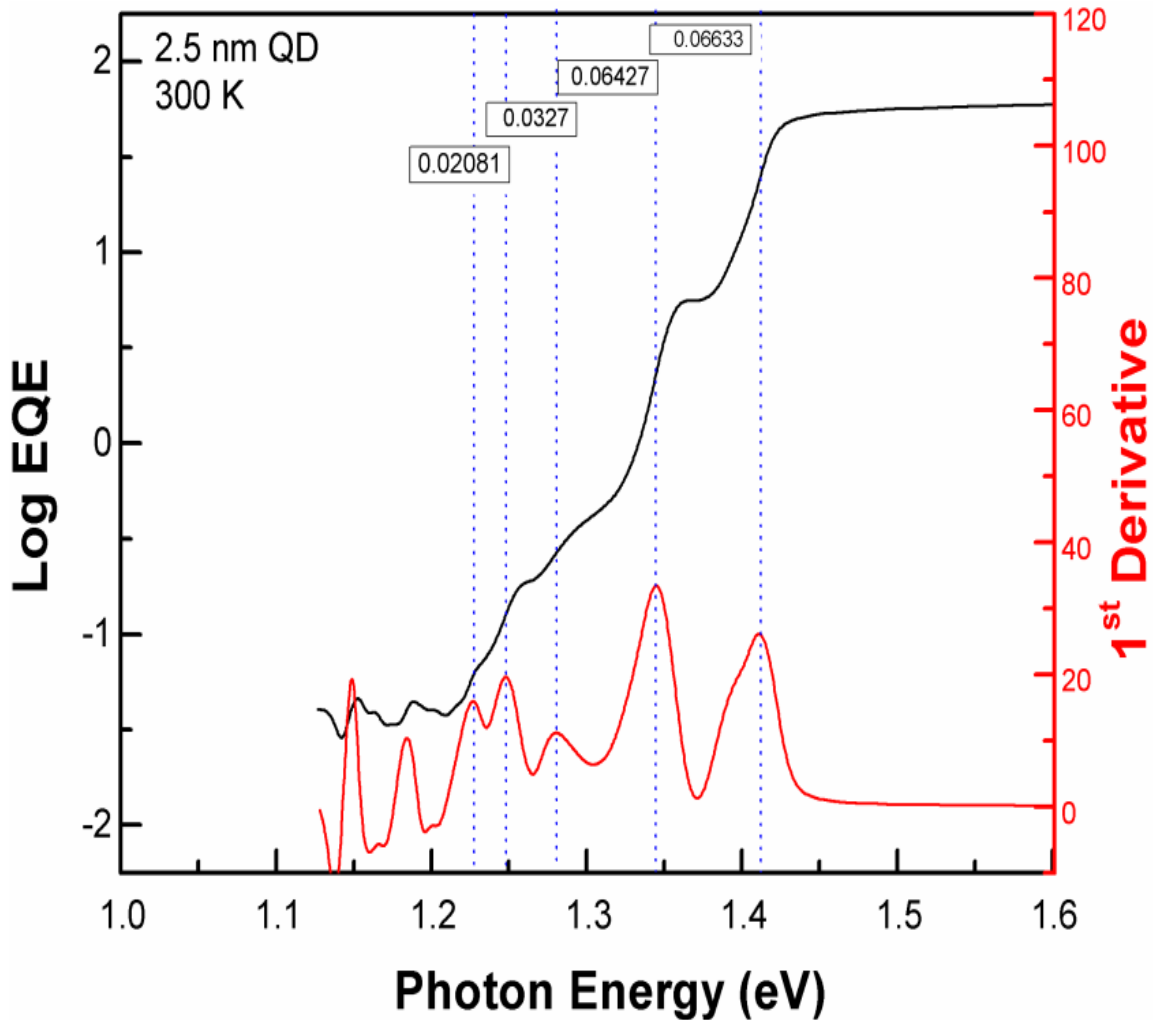


Figure 45. EQE spectrum measured at 300 K (the black line) and the first derivative analysis for sample SF2 (the red line).

Figure 46 summarizes the result of the EQE spectrum derivative analysis for sample SF3, which corresponds to the 3.1 nm QD IBSC. The peaks that correspond to the photocurrent resulting from the optical transition below 1.33 eV are found to be at energies $E_1 = 1.14$ eV, $E_2 = 1.18$ eV, $E_3 = 1.23$ eV, $E_4 = 1.27$ eV and $E_5 = 1.31$ eV. The spacing between the additional photocurrent response peaks below 1.3 eV is ~ 0.04 eV. Also, the PL power dependent measurement for 3.1 nm QD sample, shown in Figure 38, demonstrates optical transitions between the QD excited states at energies of $E_{e1-hh1} = 1.19$ eV, $E_{e2-hh2} = 1.23$ eV, $E_{e3-hh3} = 1.27$ eV, $E_{e4-hh4} = 1.31$ eV, and $E_{e5-hh5} = 1.36$ eV.

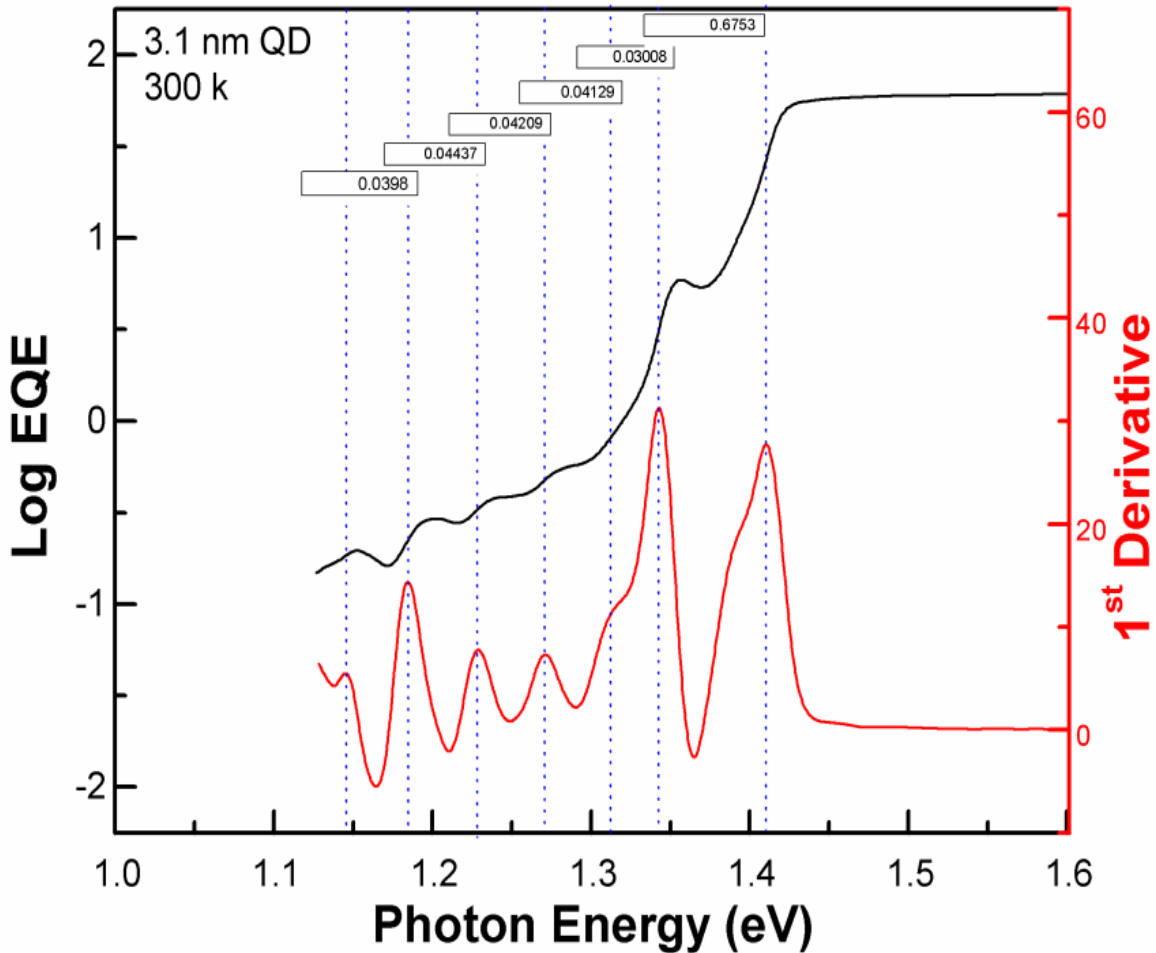


Figure 46. EQE spectrum measured at 300 K (the black line) and the first derivative analysis for sample SF3 (the red line).

The EQE derivative analysis of the SF4 sample illustrates five supplementary peaks below 1.33, shown in Figure 47. The optical transitions of the additional peaks are measured at $E_1 = 1.13$ eV, $E_2 = 1.18$ eV, $E_3 = 1.21$ eV, $E_4 = 1.27$ eV, and $E_5 = 1.31$. In Figure 39, for the 4.3 nm QD sample, QD excited states are represented at energies of $E_{e1-hh1} = 1.13$ eV, $E_{e2-hh2} = 1.18$ eV, $E_{e3-hh3} = 1.21$ eV, $E_{e4-hh4} = 1.26$ eV, $E_{e5-hh5} = 1.31$ eV, and $E_{e6-hh6} = 1.37$ eV.

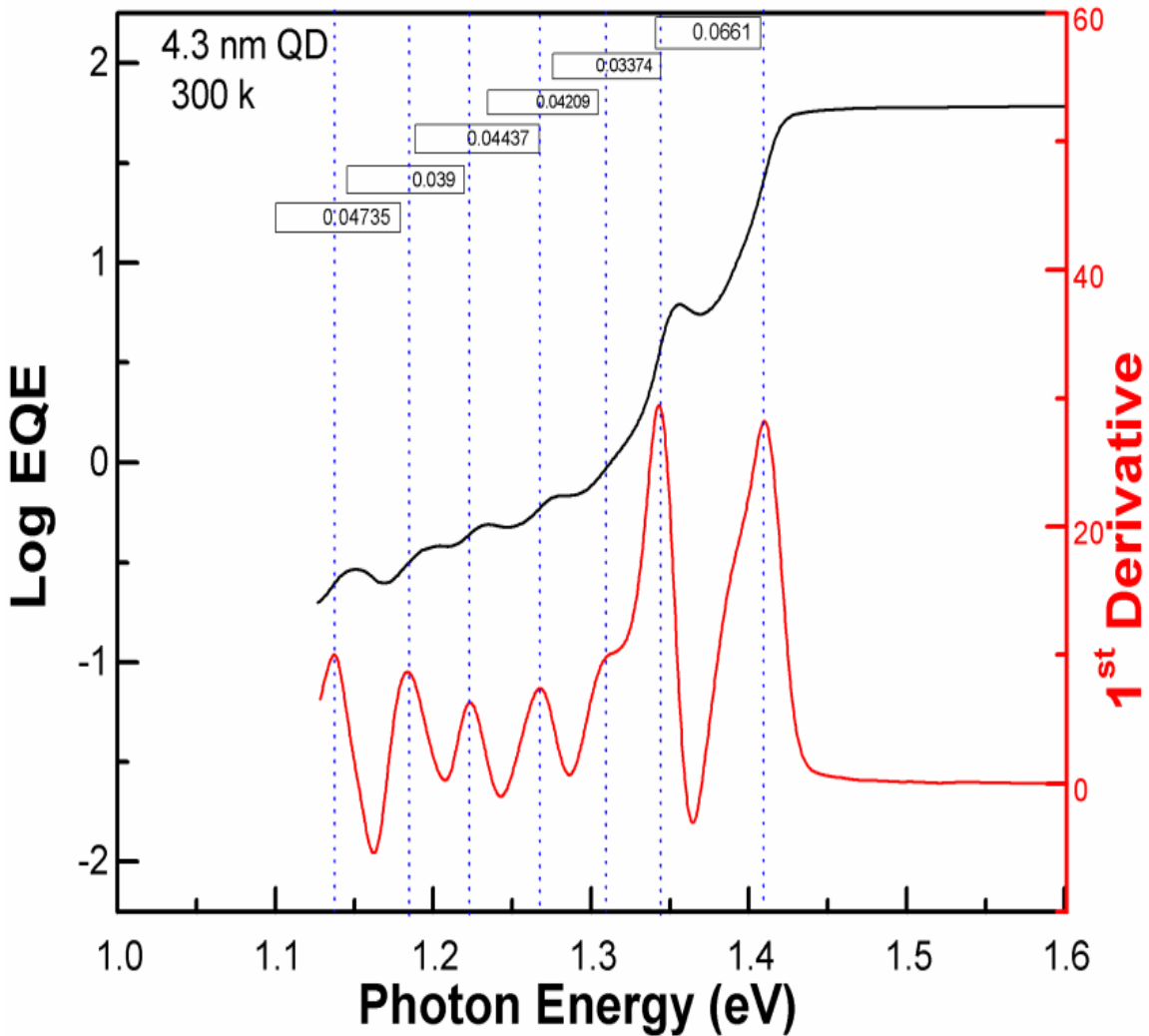


Figure 47. EQE spectrum measured at 300 K (the black line) and the first derivative analysis for sample SF4 (the red line).

Figure 48 summarizes the result of the EQE spectrum derivative analysis for sample SF5, which corresponds to the 5.1 nm QD IBSC. The peaks that correspond to the photocurrent resulting from the optical transition below 1.3 eV are found to be at energies $E_1 = 1.15$ eV, $E_2 = 1.18$ eV, $E_3 = 1.23$ eV, $E_4 = 1.27$ eV. The SF5 QD sample demonstrates optical transitions between the QD excited states at energies of $E_{e1-hh1} = 1.09$ eV, $E_{e2-hh2} = 1.14$ eV, $E_{e3-hh3} = 1.17$ eV, $E_{e4-hh4} = 1.22$ eV, $E_{e5-hh5} = 1.26$ eV and $E_{e6-hh6} = 1.30$ eV, shown in Figure 40.

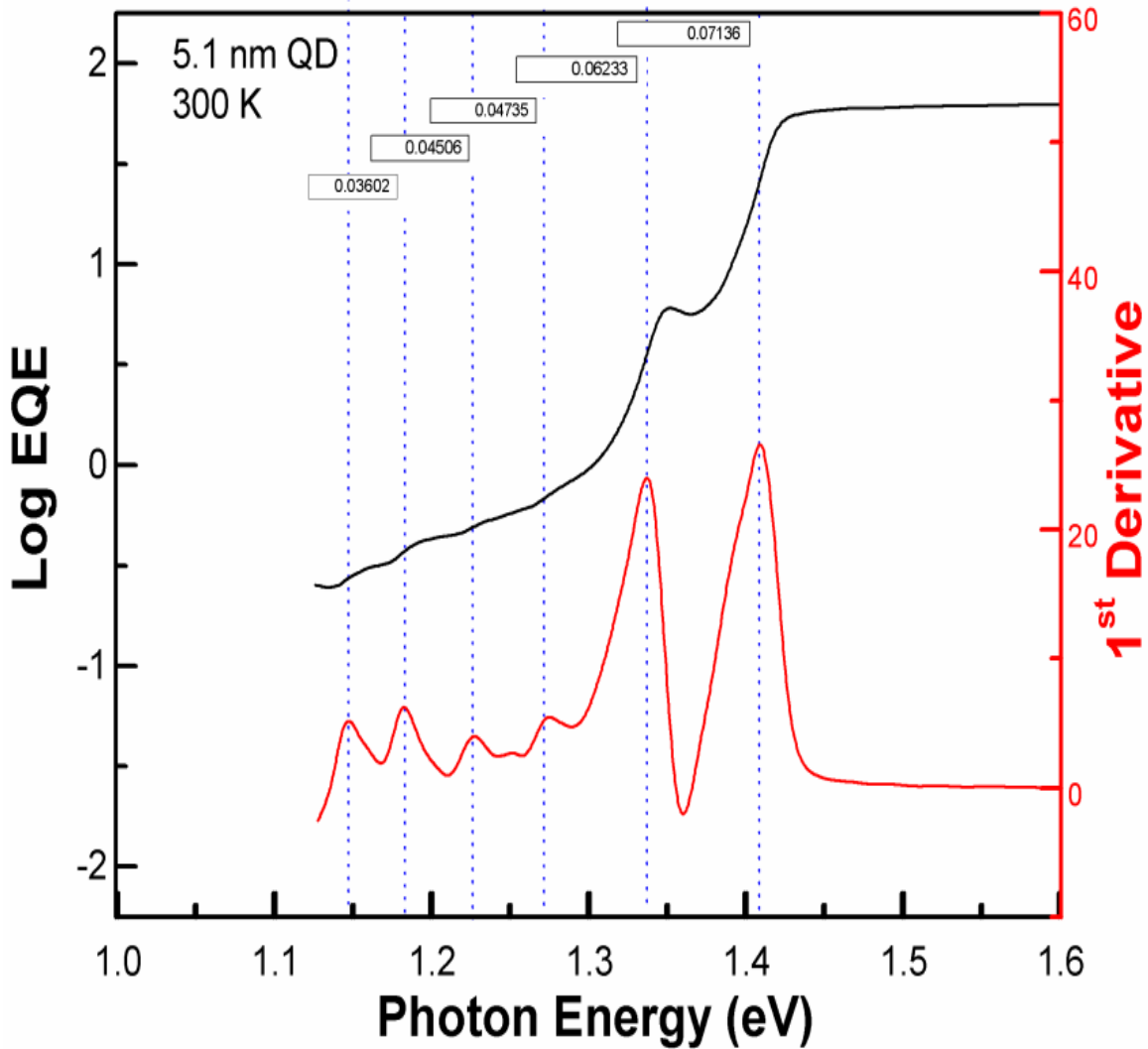


Figure 48. EQE spectrum measured at 300 K (the black line) and the first derivative analysis for sample SF5 (the red line).

Figure 49 shows the derivative analysis of the EQE spectrum for the SF7 sample, illustrating five distinguishable peaks below 1.31 eV. The peaks are measured at $E_1 = 1.13$ eV, $E_2 = 1.17$ eV, $E_3 = 1.21$ eV, $E_4 = 1.26$ eV, and $E_5 = 1.3$ eV. The spacing between the additional photocurrent response peaks is ~ 0.04 eV. In Figure 41, several PL emission peaks representing QD excited states for the 5.3 nm QD sample are measured at energies of $E_{e1-hh1} = 1.09$ eV, $E_{e2-hh2} = 1.14$ eV, $E_{e3-hh3} = 1.19$ eV, $E_{e4-hh4} = 1.24$ eV, $E_{e5-hh5} = 1.28$ eV, and $E_{e6-hh6} = 1.32$ eV. The energies measured for the PL emission peaks and the EQE peaks below 1.33 eV for all QD samples are summarized in Tables 5 and 6, respectively.

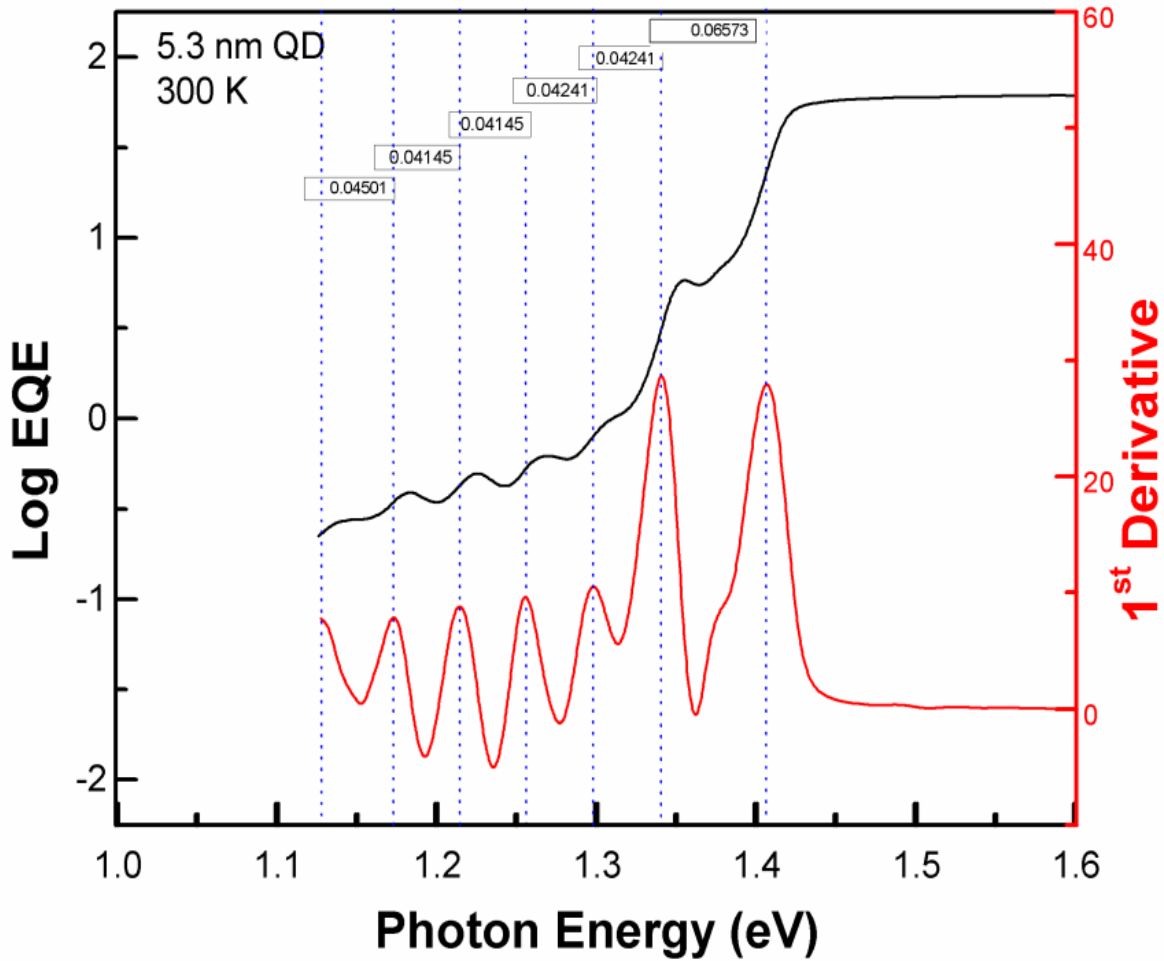


Figure 49. EQE spectrum measured at 300 K (the black line) and the first derivative analysis for sample SF7 (the red line).

Samples	QD size	E_{e1-hh1}	E_{e2-hh2}	E_{e3-hh3}	E_{e4-hh4}	E_{e5-hh5}	E_{e6-hh6}
#	nm	eV	eV	eV	eV	eV	eV
SF2	2.5	1.3382	1.3704	1.4111	-	-	-
SF3	3.1	1.1983	1.2375	1.2718	1.3152	1.3606	-
SF4	4.3	1.1317	1.1867	1.2147	1.2651	1.3103	1.3722
SF5	5.1	1.0923	1.1384	1.1744	1.2245	1.2680	1.3085
SF7	5.3	1.0930	1.1484	1.1941	1.2393	1.2829	1.3244

Table 5. Energies measured for the emission of PL representing QD excited states for all the QD samples.

Samples	QD size	E_1	E_2	E_3	E_4	E_5
#	nm	eV	eV	eV	eV	eV
SF2	2.5	1.2259	1.2468	1.2795	-	-
SF3	3.1	1.1437	1.1835	1.2279	1.2700	1.3113
SF4	4.3	1.1354	1.1827	1.2217	1.2661	1.3082
SF5	5.1	1.1460	1.1820	1.2271	1.2744	-
SF7	5.3	1.1273	1.1723	1.2138	1.2552	1.2976

Table 6. Energies measured for the optical transition in EQE representing QD excited states for all the QD samples.

Samples	QD size	Spacing between E_{e1-hh1} and E_{e2-hh2}	Spacing between E_{e2-hh2} and E_{e3-hh3}	Spacing between E_{e3-hh3} and E_{e4-hh4}	Spacing between E_{e4-hh4} and E_{e5-hh5}	Spacing between E_{e5-hh5} and E_{e6-hh6}
#	nm	eV			eV	eV
SF2	2.5	0.0322	0.407	-	-	-
SF3	3.1	0.0392	0.0343	0.0434	0.0454	-
SF4	4.3	0.0497	0.0280	0.0504	0.0454	0.0619
SF5	5.1	0.0461	0.036	0.0501	0.0435	0.0405
SF7	5.3	0.0554	0.0457	0.0452	0.0436	0.0415

Table 7. Spacing between the energies measured for the emission of PL representing QD excited states for all the QD samples.

Samples	QD size	Spacing between E_1 and E_2	Spacing between E_2 and E_3	Spacing between E_3 and E_4	Spacing between E_4 and E_5	Spacing between E_5 and E_6
#	nm	eV			eV	eV
SF2	2.5	0.0208	0.0327	-	-	-
SF3	3.1	0.0398	0.04437	0.0420	0.04129	-
SF4	4.3	0.04735	0.0390	0.04437	0.04209	-
SF5	5.1	0.03602	0.04606	0.04735	-	-
SF7	5.3	0.04501	0.04145	0.04145	0.04241	-

Table 8. Spacing between the optical transitions of the EQE of photon energies below 1.33 eV, representing QD excited states, for all the QD samples.

The EQE spectrum derivative analysis and the low temperature PL excitation power dependent measurement provide clear explanations of the origin of the additional peaks measured below 1.33 eV in the EQE measurement. It was concluded that the additional peaks response corresponds to optical transitions between quantum dot excited states. The spacing between the additional peaks is different for different samples, depending on the QD size, shown in Tables 7 and 8, respectively.

The temperature-bandgap dependence in the bulk semiconductor materials is attributed to the electron-phonon interaction and lattice thermal expansion. The energy levels and phonon modes change with the quantum dot size, and as a result, the electron-phonon interaction can be changed. Consequently, the band gap of materials with quantum dots can vary with the variation of temperature. The value of dE_g/dT is a characteristic measure of the electron-phonon interaction. The dE_g/dT value can be affected by pressure, confinement energy, strain, exciton-phonon scattering, and Coulomb energy [91].

Since the first derivative of the external quantum efficiency spectra indicates the absorber band gap relative shifts [92], the GaAs band gap values of a small (2.5 nm) and a large (5.1 nm) quantum dot solar devices were extracted from the first derivative of the EQE spectrum at variable temperatures (81-300 K). These values were compared to the result of the GaAs (E_{gGaAs}) bulk material band gaps using the Varshni model, expressed by Equation 16 [93]. The parameters used in the equation are summarized in Table 9. This method was used to study the energy spectrum of QD IBSC devices and examine the relative change in the energy gap of GaAs related to the induced strain caused by the quantum dots.

$$E_g(T) = E_g(T=0) - \frac{\alpha T^2}{T + \beta} \quad (16)$$

Materials	$E_g(T=300)$	$E_g(T=0)$	α	β
	eV	eV	meV/K	K
GaAs	1.42	1.519	0.5405	204
InAs	0.354	0.417	0.276	93

Table 9. Parameters used in the GaAs and InAs bandgap at variable temperatures using Varshni model.

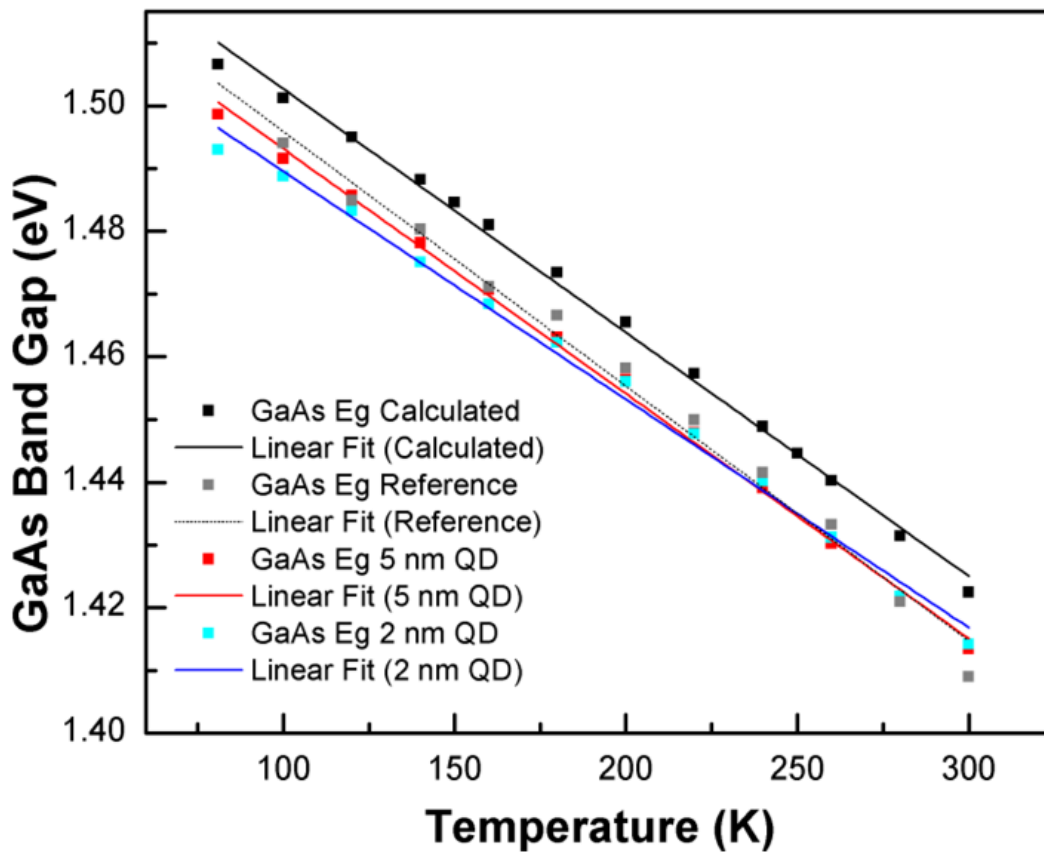


Figure 50. Calculated GaAs band gap and experimental data of GaAs band gap for the reference (SF0), smallest QD (SF2), and largest QD (SF5) samples plotted as a function of temperature (81-300 K).

Figure 50 shows the calculated $E_{g_{\text{GaAs,bulk}}}$ values and the experimentally measured $E_{g_{\text{GaAs}}}$ values of SF0, SF2, and SF5. The $dE_{\text{SF0,SF2,SF5}}/dT$ values are comparable to $dE_{\text{GaAs,bulk}}/dT = \sim -0.4$ meV/K. The band gap shifts of SF0, SF2, and SF5 are due to systematic errors in measurements.

In conclusion, a 67% EQE is measured due to photon absorption from the GaAs VB to GaAs CB and 6% EQE is measured for quantum dot samples at lower energies. At room temperature an increase in the EQE efficiency in the IR range of the spectrum is measured for all the QD IBSC devices due to QD IB absorption. Also, a change in the band edge of the EQE spectrum indicates quantum dot size variation in all the QD samples. In addition, a loss in the external quantum efficiency at high energy light was measured for devices with large quantum dots (SF4 SF5 and SF7) indicating defects and recombination at the GaAs barrier. However, the external quantum efficiencies comparable to the reference sample SF0 efficiency were measured for devices with small quantum dots (SF2 and SF3). Additional peaks corresponds to optical transitions between quantum dot excited states were measured at $E < 1.33$ eV.

4.3.2. Solar Cell Efficiency

Solar efficiency studies have been performed on all the quantum dot IBSC samples and the reference sample. All samples have effective areas of $5 \times 5 \text{ mm}^2$ and have no anti-reflective coating. Solar conversion efficiency was calculated from the I-V curves measured in dark and under illumination, using an AM 1.5 solar simulator (irradiance of 100 mW/cm^2).

Figure 51 summarizes the result of the illuminated I-V measurement on all samples at room temperature (300 K). The dependence of voltage on the quantum dot size is demonstrated, where samples SF4, SF5, and SF7 with quantum dot capping layers of 4, 5, and 7 nm, respectively, exhibit a significant decrease compared to the reference sample (SF0). The I-V curves for large quantum dots exhibit different behavior at voltages above 0.4 V. To understand the mechanisms causing the non-linear behavior for samples 5.1 and 5.3 nm, further studies need to be performed. It is important to note that all quantum dots in these samples were undoped. Since the intermediate band (IB) in the quantum dot samples is not half-full of electrons, the absorption in the IB to CB transition is weak. Knowing that, Figure 51 shows a small increase in the short circuit current (I_{oc}) for the quantum dot samples, compared to the reference sample.

Figure 52 summarizes the result of efficiency studies on all samples at room temperature (300 K), showing all of the samples' efficiencies and open circuit voltages plotted together as a function of the height of the truncated dots. The zero height quantum dots refer to the reference sample. The efficiency of devices with 2.5 and 3.1 nm quantum dots is higher than the efficiency of the reference samples, while larger quantum dot devices (excluding the non-linearity) show a major efficiency decrease compared to the reference sample. Similarly, the open circuit voltage (V_{oc}) drops with the increase of QD height. The decrease in the efficiency with the increase of quantum dot height is attributed to the decrease in open circuit voltage in these samples. In

Figure 52, the tallest quantum dot (SF7) sample shows the lowest efficiency (4.262%). However, the efficiency of the small quantum dot (SF2 and SF3) samples are the highest (8.4818 and 8.6989%).

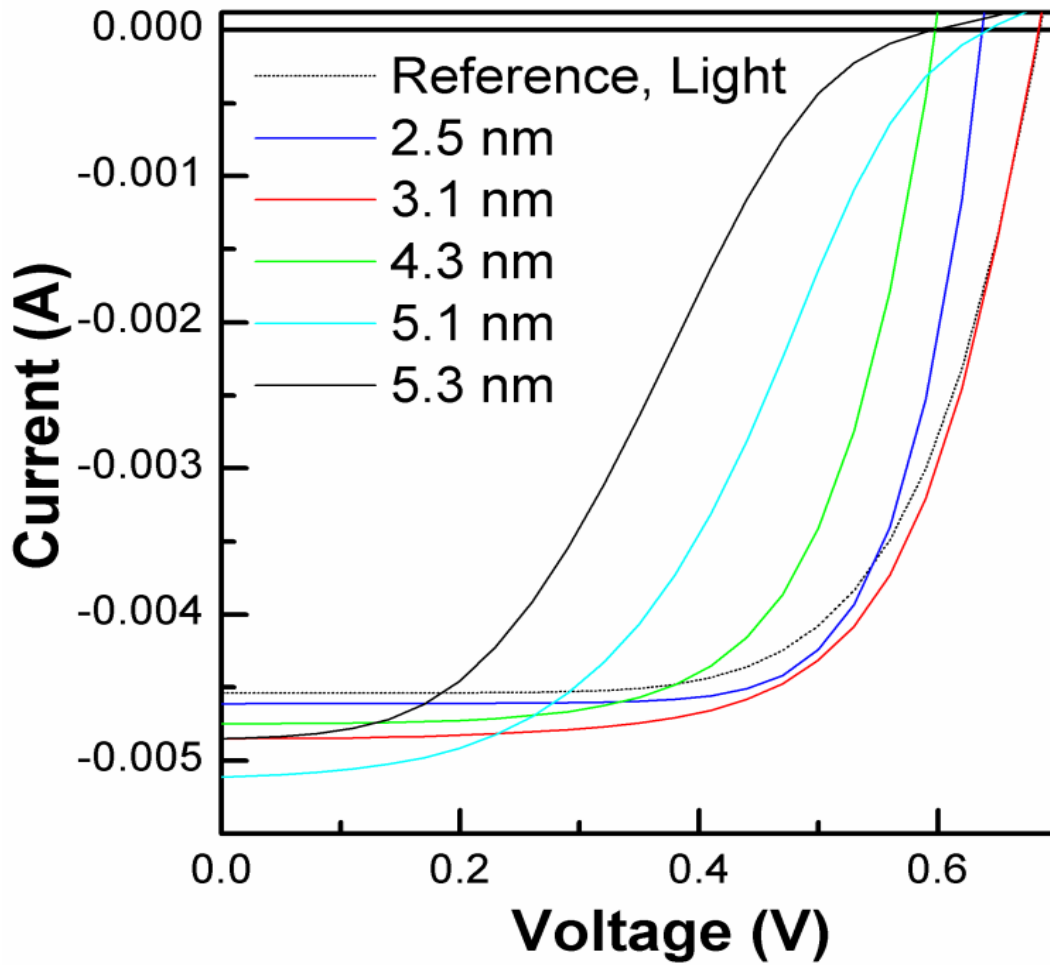


Figure 51. Current-Voltage measurements of all samples under illumination of AM1.5 standard (100mW/cm²) at 300 K.

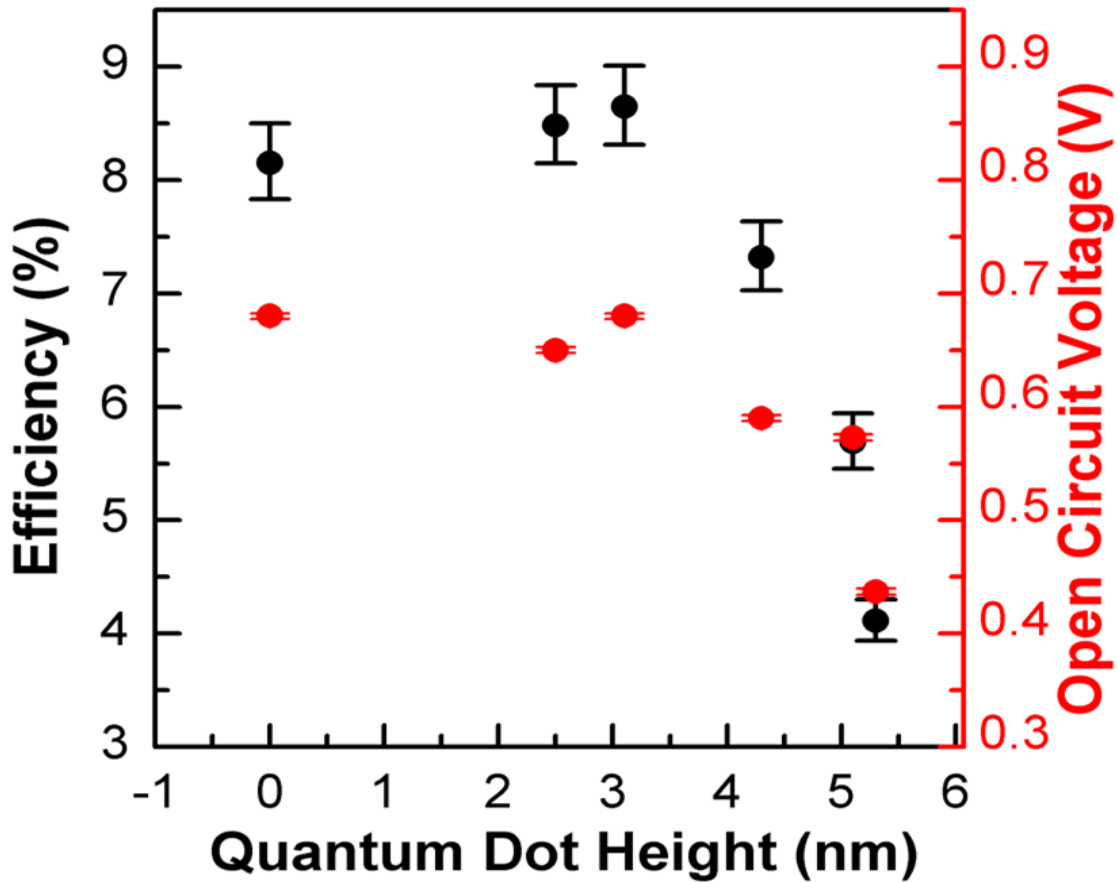


Figure 52. Open circuit voltage and efficiency as a function of QD height for all samples at 300 K.

The observed decrease in the efficiency with the increase of quantum dot size is mainly a result of the decrease in the open circuit voltage. One possible explanation of the V_{oc} degradation with the quantum dot size is related to the open circuit voltage being band gap dependent. V_{oc} increases with the increase of the device's effective band gap, while the effective device's band gap decreases with the increase of the QD height. The open circuit voltage being band gap dependent agrees with previously reported studies as the cause of open circuit reduction in quantum dot solar cells [94], [54], [95]. Also, one of the factors that influences the V_{oc} is electron-hole recombination in the IB region. Recombination is quantum dot size dependent.

Noting that the InAs quantum dots are not doped, the areal densities are the same, and their position within the intrinsic region is close to the 400 nm p-type doped emitter region (heavily doped (10^{18} cm^{-3}) with Beryllium). Therefore, the probability of the quantum dot valence band energy level occupation by the majority charge carrier (holes) of the emitter is very high. The majority charge carriers in the emitter (holes) occupying the QD VB states could capture the carriers generated by the incident light and recombine [95], [76].

One reason for the low efficiency of the solar cell devices with large quantum dots is that large quantum dots result in a higher strain field in the barrier layers compared to the smaller quantum dots, thereby resulting in defect states that function as recombination centers in the emitter region and the space charge region, where SRH recombination is the most effective [54]. This can be seen as a decrease at higher photon energies in the external quantum efficiency spectrum of sample SF4 and SF5. The external quantum efficiency spectra at higher energy for samples SF4 and SF5 is less than that for samples SF2 and SF3, which agrees with the decrease of open circuit voltage in the large quantum dots.

Similarly, the efficiency measurement has been done on QD intermediate band solar cells with different QD heights as a function of temperature. The result of solar cell efficiency measurements at variable temperatures are summarized in Figure 53. Figure 53 demonstrates that the smaller quantum dot solar cells have higher efficiencies than the larger quantum dot solar cells for all temperatures (81–300 K).

For the reference sample, the efficiency increased with the decrease of temperature. The band gap of the space charge region decreases with the increase of temperature, resulting in a slight increase in the solar cell short circuit current and a significant decrease in the open circuit voltage [96]. Therefore, the increase in the efficiency with decreasing temperature is attributed to

the increase of the open circuit voltage with temperature. This can be seen in Figure 54 which shows that the open circuit voltage decreases with temperature for a small quantum dot sample (SF3), a larger quantum dot sample (SF4), and the reference sample.

In Figure 53, at 300 K, the 2 nm and 3 nm quantum dot samples efficiencies are comparable to the reference sample efficiency measurement, while at low temperature (80 K), the efficiencies of the QD samples diverge. The reason behind the efficiency decrease of the QDs samples compared to the reference sample at low temperature is that undoped quantum dots are acting as effective traps of the carriers. By decreasing the temperature, the thermal energy (kT) is reduced, resulting in lowering the probability of escape of the trapped carriers and thereby increasing the probability of band-to-band carrier recombination.

The efficiency increase trend of the QD samples in the temperature range of 140-240 K is different for different samples. The short circuit current and the open circuit voltage has the opposite temperature dependence, where I_{sc} decrease with the decrease of temperature and V_{oc} increase with increase of temperature. This is reflected in Figure 54. The combination of the values of I_{sc} and V_{oc} at moderate temperature results in the complex behavior of the efficiency curves of the QD samples in the temperature range of 140-240 K. Also, the carrier trapping/escape is a temperature dependent process, which along with quantum dot size dependence can affect temperature behavior of the efficiency curves. The solar cell efficiency conversion (η), open circuit voltage (V_{oc}), short circuit current (I_{sc}), filling factor (FF), and solar cell maximum power (P_{max}) values at variable temperatures (81-300K) for all samples are summarized in Tables 10-15.

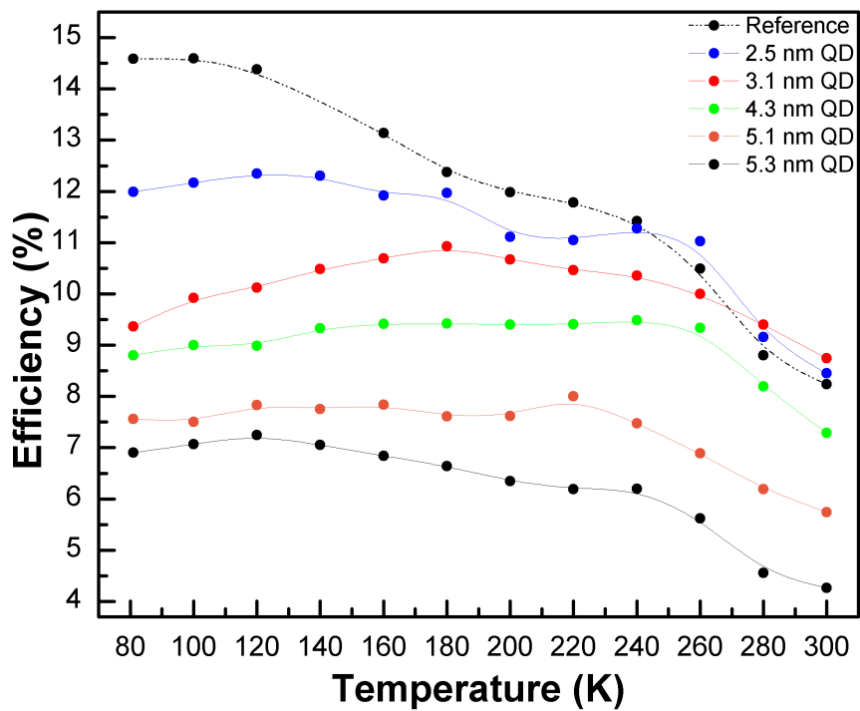


Figure 53. Efficiency as a function of temperature for all samples.

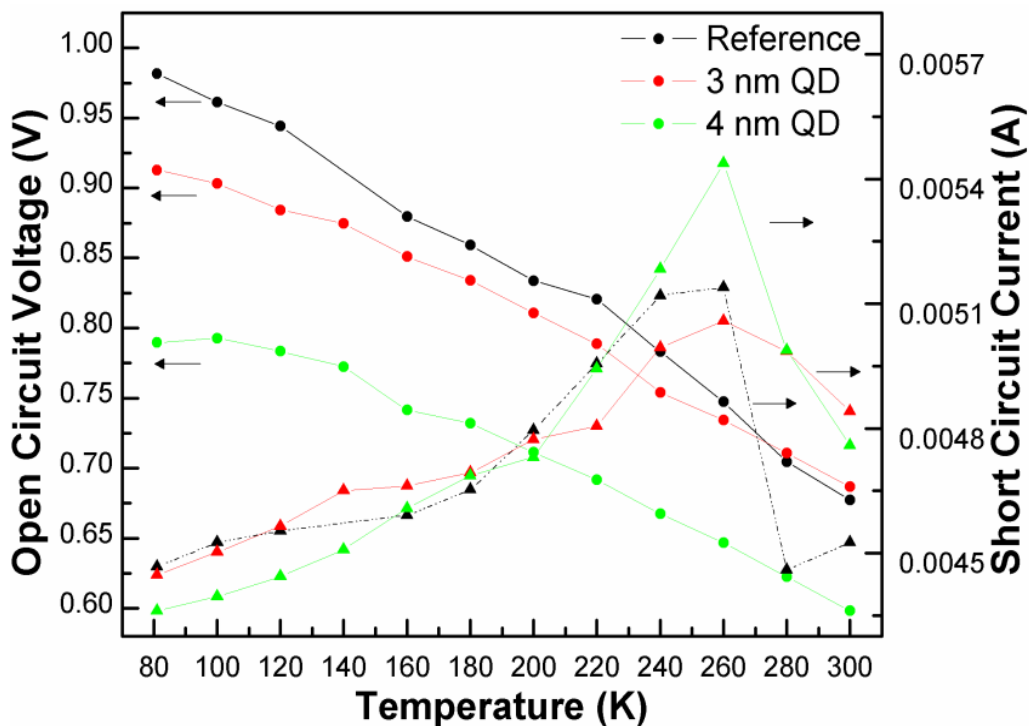


Figure 54. Open circuit voltage and short circuit current as a function of temperature for reference, 3 nm QD, 4 nm QD samples.

Reference (SF0)					
Temperature	V_{oc}	I_{sc}	P_{max}	FF	Efficiency
K	V	A	W		%
81	0.9815	0.00447	0.00365	0.8316	14.5880
100	0.9612	0.00453	0.00365	0.83891	14.5960
120	0.9441	0.00455	0.0036	0.8361	14.3804
160	0.8796	0.00459	0.00329	0.8135	13.1408
180	0.8594	0.00465	0.00309	0.7738	12.3780
200	0.8337	0.0048	0.00300	0.7491	11.9812
220	0.8205	0.00496	0.00295	0.7244	11.7828
240	0.7832	0.00512	0.00285	0.7117	11.4160
260	0.7474	0.00514	0.00262	0.6829	10.4940
280	0.7047	0.00446	0.00220	0.6999	8.79960
300	0.6853	0.00453	0.00206	0.67148	8.23480

Table 10. The open circuit voltage (V_{oc}), short circuit current (I_{sc}), solar cell maximum power (P_{max}) values, filling factor (FF), and efficiency at variable temperatures for the reference sample (SF0).

2.5 nm (SF2)					
Temperature	V_{oc}	I_{sc}	P_{max}	FF	Efficiency
K	V	A	W		%
81	0.85184	0.00453	0.00300	0.7761	11.9886
100	0.8456	0.00455	0.00304	0.7904	12.1648
120	0.8362	0.00460	0.00309	0.8035	12.3496
140	0.8129	0.00462	0.00308	0.8190	12.3060
160	0.7943	0.00465	0.00298	0.8070	11.9176
180	0.7818	0.00473	0.00299	0.8092	11.9652
200	0.7647	0.00465	0.00278	0.7818	11.1156
220	0.7445	0.00480	0.00276	0.7732	11.0508
240	0.7212	0.00530	0.00282	0.7370	11.2792
260	0.6776	0.00554	0.00276	0.7340	11.0300
280	0.6714	0.00475	0.00229	0.7185	9.15800
300	0.6341	0.00464	0.00219	0.7437	8.48180

Table 11. The open circuit voltage (V_{oc}), short circuit current (I_{sc}), solar cell maximum power (P_{max}) values, filling factor (FF), and efficiency at variable temperatures for the 2.5 nm sample (SF2).

3.1 nm (SF 3)					
Temperature	V_{oc}	I_{sc}	P_{max}	FF	Efficiency
T	V	A	W		%
81	0.9129	0.00445	0.00234	0.5722	9.36120
100	0.9031	0.0045	0.00248	0.6097	9.91880
120	0.8844	0.00456	0.00253	0.6267	10.1228
140	0.8747	0.00465	0.00262	0.6444	10.4864
160	0.8508	0.00466	0.00267	0.6736	10.6884
180	0.8339	0.00469	0.00273	0.6981	10.9304
200	0.8106	0.00477	0.00267	0.6895	10.6709
220	0.7889	0.00481	0.00262	0.6897	10.4608
240	0.7541	0.00500	0.00259	0.6875	10.3588
260	0.7341	0.00506	0.00250	0.6730	9.99760
280	0.7108	0.00499	0.00235	0.6629	9.39760
300	0.6839	0.00484	0.00214	0.6432	8.69896

Table 12. The open circuit voltage (V_{oc}), short circuit current (I_{sc}), solar cell maximum power (P_{max}) values, filling factor (FF), and efficiency at variable temperatures for the 3.1 nm sample (SF3).

4.3 nm (SF4)					
Temperature	V_{oc}	I_{sc}	P_{max}	FF	Efficiency
K	V	A	W		%
81	0.7896	0.00436	0.0022	0.6387	8.7996
100	0.7927	0.00439	0.00225	0.6459	9.0016
120	0.7834	0.00444	0.00224	0.6456	8.9880
140	0.7725	0.00451	0.00233	0.6698	9.3324
160	0.7414	0.00461	0.00235	0.6891	9.4176
180	0.7321	0.00469	0.00235	0.6863	9.4192
200	0.7114	0.00473	0.00235	0.6984	9.4028
220	0.6916	0.00494	0.00235	0.6880	9.4108
240	0.6675	0.00518	0.00237	0.6852	9.4828
260	0.6466	0.00544	0.00233	0.6638	9.3372
280	0.6225	0.00499	0.00205	0.6596	8.1920
300	0.5983	0.00476	0.00182	0.6404	7.2920

Table 13. The open circuit voltage (V_{oc}), short circuit current (I_{sc}), solar cell maximum power (P_{max}) values, filling factor (FF), and efficiency at variable temperatures for the 4.3 nm sample (SF4).

5.1 nm (SF5)					
Temperature	V_{oc}	I_{sc}	P_{max}	FF	Efficiency
T	V	A	W		%
81	0.9947	0.00454	0.00189	0.4187	7.5616
100	0.9550	0.00467	0.00188	0.4206	7.5016
120	0.9154	0.00471	0.00196	0.4539	7.8284
140	0.9014	0.00485	0.00194	0.4433	7.7500
160	0.8555	0.00482	0.00196	0.4749	7.8344
180	0.8096	0.00489	0.00190	0.4803	7.6092
200	0.7793	0.00499	0.00190	0.4894	7.6132
220	0.7435	0.00542	0.00200	0.4964	8.0024
240	0.7381	0.00561	0.00187	0.4516	7.4748
260	0.6790	0.00571	0.00172	0.4442	6.8864
280	0.6448	0.00562	0.00155	0.4266	6.1888
300	0.6689	0.00510	0.00144	0.4205	5.7400

Table 14. The open circuit voltage (V_{oc}), short circuit current (I_{sc}), solar cell maximum power (P_{max}) values, filling factor (FF), and efficiency at variable temperatures for the 5.1 nm sample (SF5).

5.3 nm (SF7)					
Temperature	V_{oc}	I_{sc}	P_{max}	FF	Efficiency
K	V	A	W		%
81	0.8804	0.00441	0.00173	0.4446	6.9008
100	0.8446	0.00445	0.00177	0.4703	7.0684
120	0.8182	0.00451	0.00181	0.4904	7.2436
140	0.8205	0.00458	0.00176	0.4695	7.0556
160	0.7762	0.00472	0.00171	0.4667	6.8364
180	0.7684	0.00472	0.00166	0.4575	6.6412
200	0.7482	0.00473	0.00159	0.4480	6.3500
220	0.7295	0.00489	0.00548	0.4335	6.1916
240	0.7062	0.00526	0.00155	0.4169	6.1937
260	0.6541	0.00548	0.00141	0.3919	5.6212
280	0.6596	0.00527	0.00114	0.3274	4.5564
300	0.6044	0.00485	0.00107	0.3638	4.2620

Table 15. The open circuit voltage (V_{oc}), short circuit current (I_{sc}), solar cell maximum power (P_{max}) values, filling factor (FF), and efficiency at variable temperatures for the 5.3 nm sample (SF7).

Growth Technique	Total Thickness of the Grown Layers (nm)	Thickness of The n region (nm)	Thickness of The Intrinsic region (nm)	Thickness of The p region (nm)	QD Layers (#)	Barrier Layer Thickness (nm)	Anti-Reflective Coating	Spectrum	Open Circuit Voltage V_{oc} (V)	Decrease of QD V_{oc} VRS REF V_{oc} (%)	Conversion Efficiency (%)	Sample	References
MBE	1093	300	613	180	10	50	No	AM1.5	0.71	15.4	6.8	-	[97]
MBE	1798	500	1118	180	20	25	No	AM1.5	0.696	-	9.0	-	[98]
MBE	3660	3010	130	430	10	10	Yes ZnS/MgF ₂	AM1.5	0.84	19.23	18.32	State of the Art	[99]
MBE	4120	3350	330	440	10	28	No	AM1.5	0.63	7.4	8.75	2 nm InAs QD	Thesis
MBE	4120	3350	330	440	10	28	No	AM1.5	0.797	-	10.13	2 nm InAs QD Optimized contact-mask	Thesis
MBE	4120	3350	330	440	10	27	No	AM1.5	0.68	0.2	8.55	3 nm InAs QD	Thesis

Table 16 Intermediate band solar cell experimental recorders of the efficiency and open circuit voltage compared with the results of this research.

Table 16 summarizes the intermediate band solar cell experimental data of the efficiencies and open circuit voltages [97], [98], [99] and are compared with the results of this research. The open circuit voltage of the IBSC devices has been improved by growing a strain compensated layer (SC) on top of the quantum dots. The SC layer decreases the strain effects of dislocations resulting during SK growth, thereby reducing the strain-related non-radiative recombination [52]. Also, an improvement in the open circuit voltage in IBSCs resulted from surrounding the QDs by a AlGaAs defense layer that led to an increase in the transmission through the WL and a reduction of the recombination process [97]. In addition, doping the InAs/GaAs (n-doping) QDs increases the open circuit voltage of the IBSCs compared to undoped quantum dots by reducing the effect of the quantum dots acting as recombination centers [98]. Despite adding a SC layer, surrounding the QD by AlGaAs layers, and n- doping the quantum dots, the reported IBSCs have open circuit voltages less than the reference devices. Comparing the V_{oc} of QD samples to the V_{oc} of the reference samples, this research results in the fabrication of QD IBSC device with a V_{oc} comparable to the V_{oc} of the reference sample. The efficiencies of SF2 and SF3 can be enhanced by modifying several parameters in the structure of the device growth and fabrication, such as doping the QDs, including the strain balancing layer, lapping the thick GaAs substrate, and introducing an anti-reflective coating.

In conclusion, illuminated I-V measurement demonstrates a small difference in the photocurrent of the quantum dot samples and reference sample that can be attributed to the quantum dots being undoped. Also, a dependency of the open circuit voltage on QD size is observed. The open circuit voltage and efficiency of QD IBSCs decreases with the increase of the QDs size, above 3 nm. Furthermore, the open circuit voltage of the small quantum dot sample (SF3) is comparable to the reference sample's V_{oc} .

Chapter 5: Conclusion and Future Work

The effect of quantum dot height on the performance of quantum dot intermediate band solar cells was investigated in this work. All solar cell samples were grown by solid source molecular-beam epitaxy. For all the QD samples, the intermediate band was created with InAs quantum dots, using the Stranski-Krastanov (SK) growth method, consisting of 10 quantum dot layers and placed in the space charge region of the solar cell close to the emitter. Applying the capped and annealed quantum dot truncation technique, the height of the quantum dots was varied while the density of the dots was kept constant. Detailed structural, optical, electrical, as well as temperature dependent efficiency studies were done to reveal possible mechanisms of efficiency degradation of the quantum dot solar cells compared to the reference solar cell device.

Transmission Electron Microscopy (TEM) studies allowed us to learn about the InAs quantum dot shape, physical dimensions, and specifically, about the quantum dot heights modified during the truncation growth method. The results of the TEM analysis showed that the average quantum dot heights achieved are 2.5 nm, 3.1 nm, 4.3 nm, 5.1 nm, and 5.3 nm for 2 ML InAs quantum dot deposition followed by GaAs capping of different thicknesses of 2 nm, 3nm, 4nm, 5 nm and 7 nm, respectively, and truncation by annealing. High resolution TEM images indicate high quality quantum dots, InAs/GaAs interfaces, and GaAs spacers.

Low temperature photoluminescence measurements for the QD samples confirmed InAs quantum dot height variation from sample to sample, which is in good agreement with the structural studies. The quantum dot height decrease was shown as a blue shift of the PL line at low temperatures. These studies indicated that the quantum dot samples have a single size distribution, with the exception of the sample with 2 nm GaAs capping, where a bi-modal quantum dot size distribution was revealed. Additionally, PL shows enhanced carrier escape in

the smaller quantum dots compared to the larger quantum dots, resulting in a significant reduction of the PL signal. Furthermore, power dependent PL measurements were performed to illustrate the presence of the quantum dot excited states.

Efficiency studies, including both external quantum efficiency measurements and solar conversion efficiency were executed. EQE measurements indicated separate contributions of the GaAs bulk and InAs quantum dots to the conversion of the incoming light into electricity. The EQE efficiencies as high as 67% for the GaAs material and as high as 6% InAs QDs were found, respectively. Some loss in the external quantum efficiency on the GaAs side of the EQE spectrum was measured and attributed to higher defect densities for the devices with large quantum dots (~4.3 nm and ~5.1 nm.). For the samples with smaller QD heights, the external quantum efficiencies are comparable to the reference sample without InAs quantum dots.

From the solar efficiency-conversion study, a small increase in the photocurrent due to quantum dot presence was observed compared to the reference sample. Small changes in the photocurrent are understood as a result of the quantum dots being undoped. From the other side, the open circuit voltage shows degradation with increase of quantum dot heights. This experimental data suggests that the open circuit voltage decreases with the decrease of the effective band gap of the absorber media for the taller quantum dots. Another mechanism, involving Shockley-Read-Hall recombination in the presence of deep states due to defects in the quantum dot region could lead to V_{oc} degradation as well. This suggestion requires further experimental and theoretical considerations.

These results suggest that optimization of the quantum dot height is critical for reaching high efficiency conversions in the intermediate band solar cells. The results of this research found the enhancement to be best for a quantum dot height of 3 nm. To improve this type of

solar cell, further detailed studies of the recombination phenomena in the solar cell space-charge region via temperature dependent dark current-voltage and deep level transient spectroscopy studies are required. This is considered as a future goal of this project. Furthermore, studies of quantum dot intermediate band doping, introducing strain-balanced growth, thinning the GaAs substrate by lapping, adding the anti-reflective coatings, surface passivation, and improved design of the top solar cell electrode are steps that have to be studied to improve solar cell conversion efficiencies.

References

- [1] G. Conibeer, "Third-generation photovoltaics," *Mater. Today*, vol. 10, no. 11, pp. 42–50, Nov. 2007.
- [2] Natalya V. Yastrebova, "High-efficiency multi-junction solar cells: Current status and future potential," *Cent. Res. Photonics, Univ. Ottawa*, 2007.
- [3] J. Fritz and D. H. Russ, "Quantum Efficiency Measurements a-C : H Based Photovoltaic Cells," Ohio University, 1997.
- [4] E. Carlidge, "Bright Outlook for Solar Cells," *Physics World*, pp. 20–24, 2007.
- [5] "Solar cell conversion-efficiency limits 5.1." [Online]. Available: <http://aerostudents.com/files/solarCells/CH5SolarCellConversionEfficiencyLimits.pdf>. [Accessed: 10-Oct-2014].
- [6] L. Cuadra, A. Martí, and A. Luque, "Present status of intermediate band solar cell research," *Thin Solid Films*, vol. 451–452, pp. 593–599, Mar. 2004.
- [7] F. K. Tutu, J. Wu, P. Lam, M. Tang, N. Miyashita, Y. Okada, J. Wilson, R. Allison, and H. Liu, "Antimony mediated growth of high-density InAs quantum dots for photovoltaic cells," *Appl. Phys. Lett.*, vol. 103, no. 4, p. 043901, 2013.
- [8] A. Mellor, A. Luque, I. Tobias, and A. Martí, "The influence of quantum dot size on the sub-bandgap intraband photocurrent in intermediate band solar cells," *Appl. Phys. Lett.*, vol. 101, no. 13, p. 133909, 2012.
- [9] A. Luque, A. Martí, and C. Stanley, "Understanding intermediate-band solar cells," *Nat. Photonics*, vol. 6, no. 3, pp. 146–152, Feb. 2012.
- [10] A. Martí, L. Cuadra, and A. Luque, "Quantum dot intermediate band solar cell," in *Conference Record of the Twenty-Eighth IEEE Photovoltaic Specialists Conference - 2000 (Cat. No.00CH37036)*, 2000, pp. 940–943.
- [11] V. Kunets, M. Ware, M. Mortasavi, and G. Salamo, "Control of Open Circuit Voltage in Quantum Dot, Intermediate Band Solar Cells," 2013.
- [12] A. Klaver, *Irradiation-induced degradation of amorphous silicon solar cells in space*, no. december. 2007.
- [13] F. Dimroth, C. Baur, and A. Bett, "3-6 junction photovoltaic cells for space and terrestrial concentrator applications," *IEEE, Photovolt. Spec. Conf. 2005*, pp. 525–529, 2005.

- [14] Y. Okada, K. Yoshida, Y. Shoji, and T. Sogabe, "Recent progress on quantum dot intermediate band solar cells," *IEICE Electron. Express*, vol. 10, no. 17, pp. 20132007–20132007, 2013.
- [15] D. Guimard, R. Morihara, D. Bordel, K. Tanabe, Y. Wakayama, M. Nishioka, and Y. Arakawa, "Fabrication of InAs/GaAs quantum dot solar cells with enhanced photocurrent and without degradation of open circuit voltage," *Appl. Phys. Lett.*, vol. 96, no. 20, p. 203507, 2010.
- [16] A. Mart, E. Antol, A. Luque, and S. Member, "Review of Experimental Results Related to the Operation of Intermediate Band Solar Cells," vol. 4, no. 2, pp. 736–748, 2014.
- [17] B. Streetman and S. Banerjee, *Solid State Electronic Devices*, 6th ed. New Delhi: PHI Learning Private Limited, 2005, pp. 1–89.
- [18] "Electrical Conductance Conductivity of Metal Semiconductor and Insulator | Band Theory," *Electrical4U*. [Online]. Available: <http://www.electrical4u.com/electrical-conductivity-of-metal-semiconductor-and-insulator/>. [Accessed: 11-Jan-2014].
- [19] "Intrinsic Carrier Concentration," *PV Education*. [Online]. Available: <http://www.pveducation.org/pvcdrom/pn-junction/intrinsic-carrier-concentration>. [Accessed: 10-Feb-2014].
- [20] "Doping," *PV Education*. [Online]. Available: <http://www.pveducation.org/pvcdrom/pn-junction/doping>. [Accessed: 10-Feb-2014].
- [21] S. Dimitrijević, *Principles of Semiconductor Devices*, 2nd ed. New York: Oxford University Press, Inc, 2011, pp. 20–44.
- [22] R. Shankar, *Principles of Quantum Mechanics*, 2nd ed. Plenum Press, 2011, pp. 5–202.
- [23] G. Sun, "The Intersubband Approach to Si-based Lasers," , Massachusetts, U.S.A: Advances in Lasers and Electro Optics, Nelson Costa and Adolfo Cartaxo, 2010.
- [24] "Types of Recombination," *PV Education*. [Online]. Available: <http://pveducation.org/pvcdrom/pn-junction/types-of-recombination>. [Accessed: 23-Sep-2014].
- [25] E. Timo and B. Vilpponen, "Analysis of Intermediate Band Solar Cell Performance," Norwegian University of Science and Technology, 2011.
- [26] A. Sproul, "Understanding the p-n Junction," *Key Cent. Photovolt. Eng. UNSW*, pp. 13–24.
- [27] J. Gray, *The Physics of the Solar Cell*. Indiana, USA: Purdue University, 2005, pp. 61–63.

- [28] “Standard Solar Spectra,” *Education, PV*. [Online]. Available: <http://pveducation.org/pvcdrom/appendices/standard-solar-spectra>. [Accessed: 11-Jan-2014].
- [29] F. Dimroth, “High-efficiency solar cells from III-V compound semiconductors,” *Phys. Status Solidi*, vol. 3, no. 3, pp. 373–379, Mar. 2006.
- [30] “Humane Society of Greater Miami.”
- [31] “Efficiency limits of photovoltaic energy conversion.” [Online]. Available: <http://www.superstrate.net/pv/limit/>. [Accessed: 07-Mar-2014].
- [32] O. Semonin, J. M. Luther, and M. C. Beard, “Multiple exciton generation in a quantum dot solar cell,” *The International Society for Optics and Photonics*, 2012.
- [33] A. Luque, A. Martí, P. Wahnou, L. Cuadra, C. Tablero, C. Stanley, A. McKee, D. Zhou, R. Konenkamp, R. Bayon, A. Belaidi, J. Alonso, J. Ruiz, J. Fernandez, P. Palacios, and N. Lopez, “Progress towards the practical implementation of the intermediate band solar cell,” in *Conference Record of the Twenty-Ninth IEEE Photovoltaic Specialists Conference, 2002.*, pp. 1190–1193.
- [34] E. Antolín, A. Martí, C. D. Farmer, P. G. Linares, E. Hernández, A. M. Sánchez, T. Ben, S. I. Molina, C. R. Stanley, and A. Luque, “Reducing carrier escape in the InAs/GaAs quantum dot intermediate band solar cell,” *J. Appl. Phys.*, vol. 108, no. 6, p. 064513, 2010.
- [35] V. P. Kunets, C. S. Furrow, T. A. Morgan, Y. Hirono, M. E. Ware, V. G. Dorogan, Y. I. Mazur, V. P. Kunets, and G. J. Salamo, “InGaAs quantum wire intermediate band solar cell,” *Appl. Phys. Lett.*, vol. 101, no. 4, p. 041106, 2012.
- [36] X.-G. Yang, T. Yang, K.-F. Wang, Y.-X. Gu, H.-M. Ji, P.-F. Xu, H.-Q. Ni, Z.-C. Niu, X.-D. Wang, Y.-L. Chen, and Z.-G. Wang, “Intermediate-Band Solar Cells Based on InAs/GaAs Quantum Dots,” *Chinese Phys. Lett.*, vol. 28, no. 3, p. 038401, Mar. 2011.
- [37] A. Luque and A. Martí, “Increasing the efficiency of ideal solar cells by photon induced transitions at intermediate levels,” *Phys. Rev. Lett.*, 1997.
- [38] A. Martí, L. Cuadra, and A. Luque, “Quasi-drift diffusion model for the quantum dot intermediate band solar cell,” *Electron Devices, IEEE*, vol. 49, no. 9, pp. 1632–1639, 2002.
- [39] K. A. Sablon, J. W. Little, V. Mitin, A. Sergeev, N. Vagidov, and K. Reinhardt, “Strong enhancement of solar cell efficiency due to quantum dots with built-in charge,” *Nano Lett.*, vol. 11, no. 6, pp. 2311–7, Jun. 2011.

- [40] A. Martí, E. Antolín, E. Cánovas, N. López, and A. Luque, “Progress in Quantum-Dot Intermediate Band Solar Cell Research,” *WIP-Renewable Energies*, 2006.
- [41] A. Marti, L. Cuadra, and A. Luque, “Partial filling of a quantum dot intermediate band for solar cells,” *IEEE Trans. Electron Devices*, vol. 48, no. 10, pp. 2394–2399, 2001.
- [42] E. Antolin, A. Marti, P. G. Linares, I. Ramiro, E. Hernandez, C. D. Farmer, C. R. Stanley, and A. Luque, “Advances in quantum dot intermediate band solar cells,” in *2010 35th IEEE Photovoltaic Specialists Conference*, 2010, pp. 000065–000070.
- [43] “Achieving Both High-Efficiency and Flexibility.” [Online]. Available: <http://www.altadevices.com/technology-overview.php>.
- [44] G. Kamath and C. Anderson, “GaAs-GaAlAs Solar Cell,” U.S. Patent 4,163,987 Hughes Aircraft Company, Culver City, Calif, 1979.
- [45] J. F. Geisz, D. J. Friedman, J. S. Ward, a. Duda, W. J. Olavarria, T. E. Moriarty, J. T. Kiehl, M. J. Romero, a. G. Norman, and K. M. Jones, “40.8% Efficient Inverted Triple-Junction Solar Cell With Two Independently Metamorphic Junctions,” *Appl. Phys. Lett.*, vol. 93, no. 12, p. 123505, 2008.
- [46] “Why Gallium Arsenide?,” *AltaDevices*, 2012. [Online]. Available: <http://altadevices-blog.com/?p=14>. [Accessed: 23-Jun-2014].
- [47] P. Preuss, “The Practical Full-Spectrum Solar Cell Comes Closer,” 2011. [Online]. Available: <http://newscenter.lbl.gov/2011/01/24/practical-full-spectrum/>. [Accessed: 30-Mar-2014].
- [48] E. Yablonovitch, O. D. Miller, and S. R. Kurtz, “The opto-electronic physics that broke the efficiency limit in solar cells,” in *2012 38th IEEE Photovoltaic Specialists Conference*, 2012, vol. 3, no. 1, pp. 001556–001559.
- [49] X. Wang, M. R. Khan, J. L. Gray, M. A. Alam, and M. S. Lundstrom, “Design of GaAs Solar Cells Operating Close to the Shockley–Queisser Limit,” *IEEE J. Photovoltaics*, vol. 3, no. 2, pp. 737–744, Apr. 2013.
- [50] Antolín Fernández Elisa, A. M. Vega, P. G.-L. Fontes, I. R. Gonzalez, E. H. Martín, and A. L. López., “Raising the Efficiency Limit of the GaAs-based Intermediate Band Solar Cell Through the Implementation of a Mololithic Tandem with an AlGaAs top Cell,” 2010.
- [51] A. Martí, E. Antolín, C. Stanley, C. Farmer, N. López, P. Díaz, E. Cánovas, P. Linares, and A. Luque, “Production of Photocurrent due to Intermediate-to-Conduction-Band Transitions: A Demonstration of a Key Operating Principle of the Intermediate-Band Solar Cell,” *Phys. Rev. Lett.*, vol. 97, no. 24, p. 247701, Dec. 2006.

- [52] C. G. Bailey, D. V. Forbes, S. J. Polly, Z. S. Bittner, Y. Dai, C. Mackos, R. P. Raffaele, and S. M. Hubbard, "Open-Circuit Voltage Improvement of InAs/GaAs Quantum-Dot Solar Cells Using Reduced InAs Coverage," *IEEE J. Photovoltaics*, vol. 2, no. 3, pp. 269–275, Jul. 2012.
- [53] C. G. Bailey, D. V. Forbes, R. P. Raffaele, and S. M. Hubbard, "Near 1 V open circuit voltage InAs/GaAs quantum dot solar cells," *Appl. Phys. Lett.*, vol. 98, no. 16, p. 163105, 2011.
- [54] K. Driscoll, M. F. Bennett, S. J. Polly, D. V. Forbes, and S. M. Hubbard, "Effect of quantum dot position and background doping on the performance of quantum dot enhanced GaAs solar cells," *Appl. Phys. Lett.*, vol. 104, no. 2, p. 023119, Jan. 2014.
- [55] A. P. Alivisatos, "Semiconductor Clusters, Nanocrystals, and Quantum Dots," *Science*, vol. 271, no. 5251, pp. 933–937, Feb. 1996.
- [56] G. Biasiol, L. Sorba, and M. V. Phase, "Molecular Beam Epitaxy : Principles and Application," pp. 66–83, 2001.
- [57] K. Alavi, P. H. Holloway, and G. E. McGuire, *Handbook of Compound Semiconductors: Growth, Processing, Characterization, and Devices*. pp. 84–123.
- [58] F. Rinaldi, "Basics of Molecular Beam Epitaxy (MBE)," Annual Report, Optoelectronics Department, University of Ulm, 2002, pp. 1–8.
- [59] A. Lenz, "Atomic structure of capped In (Ga) As and GaAs quantum dots for optoelectronic devices," Technical University of Berlin, 2008.
- [60] Z. Othaman, L. K. Boo, S. Sakrani, and R. Muhammad, "The Stranski – Krastanov Three Dimensional Island Growth Prediction on Finite Size Model," *J. Fiz. UTM* 3, pp. 1–5, 2008.
- [61] F. Boxberg and J. Tulkki, "Theory of the electronic structure and carrier dynamics of strain-induced (Ga, In)As quantum dots," *Reports Prog. Phys.*, vol. 70, no. 8, pp. 1425–1471, Aug. 2007.
- [62] M. Cusack, P. Briddon, and M. Jaros, "Electronic structure of InAs/GaAs self-assembled quantum dots," *Phys. Rev. B*, vol. 54, no. 4, pp. R2300–R2303, Jul. 1996.
- [63] A. G. Norman, M. C. Hanna, P. Dippo, D. H. Levi, R. C. Reedy, J. S. Ward, and M. M. Al-Jassim, "InGaAs/GaAs QD superlattices: MOVPE growth, structural and optical characterization, and application in intermediate-band solar cells," in *Conference Record of the Thirty-first IEEE Photovoltaic Specialists Conference, 2005.*, pp. 43–48.
- [64] P. Holister, C. Roman, and T. Harper, "Quantum dots," *Cientifica*, no. 13, pp. 2–7, 2003.

- [65] O. Schmidt, D. Bimberg, N. N. Ledentsov, V. A. Shchukin, M. Grundmann, N. Kirstaedter, J. Bo, V. M. Ustinov, A. E. Zhukov, S. V Zaitsev, A. I. Borovkov, J. Heydenreich, A. O. Kosogov, S. S. Ruvimov, P. Werner, and U. Go, “Direct formation of vertically coupled quantum dots in Stranski-Krastanow growth,” vol. 54, no. 12, pp. 8743–8750, 1996.
- [66] K. W. Atanabe, N. K. Oguchi, and Y. G. Otoh, “Fabrication of GaAs Quantum Dots by Modified Droplet Epitaxy Fabrication of GaAs Quantum Dots by Modified Droplet Epitaxy,” *Jpn. J. Appl. Phys.*, vol. 79, 1999.
- [67] S. Fafard, Z. Wasilewski, C. Allen, D. Picard, M. Spanner, J. McCaffrey, and P. Piva, “Manipulating the energy levels of semiconductor quantum dots,” *Phys. Rev. B*, vol. 59, no. 23, pp. 15368–15373, Jun. 1999.
- [68] J. Plummer, M. Deal, and P. Griffin, *Silicon VLSI Technology: Fundamentals, Practice, and Modeling*, 1st ed. 2000, pp. 11–12.
- [69] V. Zeghbroeck, “Metal-Semiconductor Contacts,” in *Principle of Semiconductor Devices*, 2011, p. Chapter 3.
- [70] A. Baca, F. Ren, J. Zolper, R. Briggs, and S. Pearton, “A survey of ohmic contacts to III-V compound semiconductors,” *Thin Solid Films*, vol. 308–309, pp. 599–606, Oct. 1997.
- [71] H. G. Henry, “Characterization of alloyed AuGe/Ni/Au ohmic contacts to n-doped GaAs by measurement of transfer length and under the contact sheet resistance,” *IEEE Trans. Electron Devices*, vol. 36, no. 7, pp. 1390–1393, Jul. 1989.
- [72] C. Kowalski, L. Burrows, C. Fitzgerald, and J. Thornton, “AFM Manual, Document Revision History : SPM Training Notebook,” Veeco instruments, Inc. pp. 1–13, 2003.
- [73] X. Shang, “Study of quantum dots on solar energy applications,” Royal Institute of Technology Stockholm, Sweden, 2012.
- [74] S. Minor, “Plasma-Assisted Molecular Beam Epitaxial Growth of Indium Nitride for Future Device Fabrication,” University of Arkansas, 2012.
- [75] A. Pancholi, “(In,Ga)As quantum dot materials for solar cell applications: Effect of strain-reducing and strain -compensated barriers on quantum dot structural and optical properties,” University of Delaware, 2008.
- [76] T. E. Microscopy, “Quantum Dot Structures in the InGaAs System Investigated by TEM Techniques,” *Cryst. Res. Technol.*, no. C1, pp. 759–768, 2000.
- [77] D. Schroder, *Semiconductor Material and Device Characterization*, 3rd ed. Wiley Interscience, 2006, pp. 600–617.

- [78] I. Ramiro, E. Antolin, P. G. Linares, E. Hernández, A. Marti, A. Luque, C. D. Farmer, and C. R. Stanley, “Application of photoluminescence and electroluminescence techniques to the characterization of intermediate band solar cells,” *Energy Procedia*, pp. 117–121, 2011.
- [79] V. Dorgan, “Optical study of coupling mechanisms in quantum dot - quantum well hybrid nanostructure,” University of Arkansas, 2011.
- [80] PV Measurements Inc, “QEX10 Solar Cell IPCE / Quantum Efficiency / Spectral Response Measurement System.”
- [81] A. Adla, “Instrumentation for quantum efficiency measurement of solar cells,” *Renewable Energy*, pp. 1–10, 2010.
- [82] T. Nagle, “Quantum Efficiency as a Device-Physics Interpretation Tool For Thin-Film Solar Cells,” Colorado State University, 2007.
- [83] M. Law, M. C. Beard, S. Choi, J. M. Luther, M. C. Hanna, and A. J. Nozik, “Determining the internal quantum efficiency of PbSe nanocrystal solar cells with the aid of an optical model,” *Nano Lett.*, vol. 8, no. 11, pp. 3904–10, Nov. 2008.
- [84] “Quantum Efficiency,” *PV Education*. [Online]. Available: <http://www.pveducation.org/pvcdrom/solar-cell-operation/quantum-efficiency>. [Accessed: 13-Aug-2014].
- [85] Small Area Solar Simulator User’s Manual, PV Measurements, Inc. Boulder, CO.
- [86] T. Gu, M. a. El-Emawy, K. Yang, A. Stintz, and L. F. Lester, “Resistance to edge recombination in GaAs-based dots-in-a-well solar cells,” *Appl. Phys. Lett.*, vol. 95, no. 26, p. 261106, 2009.
- [87] V. P. Kunets, C. S. Furrow, T. A. Morgan, Y. Hirono, M. E. Ware, V. G. Dorogan, Y. I. Mazur, V. P. Kunets, and G. J. Salamo, “InGaAs quantum wire intermediate band solar cell,” *Appl. Phys. Lett.*, vol. 101, no. 4, p. 041106, 2012.
- [88] V. Polojärvi, A. Schramm, A. Aho, A. Tukiainen, and M. Guina, “Removal of strain relaxation induced defects by flushing of InAs quantum dots,” *J. Phys. D: Appl. Phys.*, vol. 45, no. 36, p. 365107, Sep. 2012.
- [89] M. Ware, Personal Communication, Nano Science and Engineering Institute, University of Arkansas, 2014.
- [90] M. Henini, *Handbook of Self Assembled Semiconductor Nanostructures for Novel Devices in Photonics and Electronics*. 2011, pp. 1– 78.

- [91] T. J. Liptay and R. J. Ram, "Temperature dependence of the exciton transition in semiconductor quantum dots," *Appl. Phys. Lett.*, vol. 89, no. 22, p. 223132, 2006.
- [92] "I-III-VI₂ Chalcopyrite Compound Semiconductors," in *Material Properties, Chapter 1*, pp. 5–20. [Online]. Available: <http://webdoc.sub.gwdg.de/ebook/diss/2003/fu-berlin/2002/19/chapter01.pdf>. [Accessed: 30-Oct-2014].
- [93] I. Vurgaftman, J. R. Meyer, and L. R. Ram-Mohan, "Band parameters for III–V compound semiconductors and their alloys," *J. Appl. Phys.*, vol. 89, no. 11, p. 5815, 2001.
- [94] H. F. Lu, L. Fu, G. Jolley, H. H. Tan, S. R. Tataavarti, and C. Jagadish, "Temperature dependence of dark current properties of InGaAs/GaAs quantum dot solar cells," *Appl. Phys. Lett.*, vol. 98, no. 18, p. 183509, 2011.
- [95] G. Jolley, H. F. Lu, L. Fu, H. H. Tan, and C. Jagadish, "Electron-hole recombination properties of In_{0.5}Ga_{0.5}As/GaAs quantum dot solar cells and the influence on the open circuit voltage," *Appl. Phys. Lett.*, vol. 97, no. 12, p. 123505, 2010.
- [96] N. Eisenmenger, "The Temperature Dependence of Solar Cells," no. 4, pp. 1–2, 2011.
- [97] K. A. Sablon, J. W. Little, K. A. Olver, Z. M. Wang, V. G. Dorogan, Y. I. Mazur, G. J. Salamo, and F. J. Towner, "Effects of AlGaAs energy barriers on InAs/GaAs quantum dot solar cells," *J. Appl. Phys.*, vol. 108, no. 7, p. 074305, 2010.
- [98] P. J. Carrington, M. Missous, E. Garduo-Nolasco, and A. Krier, "Characterisation of InAs/GaAs quantum dots intermediate band photovoltaic devices," *IET Optoelectron.*, vol. 8, no. 2, pp. 71–75, Apr. 2014.
- [99] S. A. Blokhin, A. V. Sakharov, A. M. Nadtochy, A. S. Pauysov, M. V. Maximov, N. N. Ledentsov, A. R. Kovsh, S. S. Mikhrin, V. M. Lantratov, S. A. Mintairov, N. A. Kaluzhniy, and M. Z. Shvarts, "AlGaAs/GaAs photovoltaic cells with an array of InGaAs QDs," *Semiconductors*, vol. 43, no. 4, pp. 514–518, Apr. 2009.

Appendix A: Description of Research for Popular Publication

Quantum dots for Solar Cell Application: Smaller Is Better

By: Najla Alnami

Scientists at the University of Arkansas are working to improve and perfect the harvesting of solar energy. This year, Najla Alnami, a scientist at The University of Arkansas, made an important contribution for improving solar efficiency by creating a new kind of quantum dot intermediate band solar cells (IBSCs). Never heard of “quantum dots” or an “intermediate band”? No problem. Here is the story of one of the most important IBSC studies in 2014 on efficiency degradation (lost efficiency).

Distinguished professor Gregory Salamo, at the University of Arkansas, has developed outstanding facilities for material growth, electrical/optical/structural characterization, and nanofabrication. In these revolutionary facilities, Dr. Salamo, along with the brilliant and talented Dr. Vasyl Kunets, attempted to understand the reasons why certain kinds of new materials, when used in solar cells, perform better than others. Before I tell the whole story about how these wonderful scientists’ new knowledge, discoveries, and perspectives can contribute to solving an actual problem to make the world a better place, let me give you a little background on solar cells. In the simplest sense, a solar cell is a device that converts sunlight to electricity. Nikola Tesla dreamed of powering the entire world for free out of the ground. While that concept still remains a dream, these scientists’ dream of powering the entire world for very little money with energy from the sun, has become a reality.

Recently, a new type of solar cell, with a promising maximum efficiency of 63% (WOW!), called a ‘quantum dot intermediate band solar cell (QD IBSC)’ attracted the attention of Drs. Salamo and Kunets. Quantum dots are very small structures (a few nanometers in size)

that cause electrons to behave differently than in regular materials. By creating several layers of these ‘quantum dots’ that are electrically connected, they form an intermediate band. Despite the high predicted efficiency (how well the device works) of these solar cells, no one has successfully created a QD IBSC with an efficiency higher than 18.3%. By thinking about the causes of this low efficiency, Drs. Salamo and Kunets decided to study the effect of quantum dot size on QD IBSC performance. To execute this new idea, Drs. Salamo and Kunets chose Najla Alnami to research and capture the relative functional theory.

Najla Alnami is a scientist and graduate student majoring in Microelectronics-Photonics at the Institute of Nano Science and Engineering at the University of Arkansas. She has taken a promising existing solar cell device (the QD IBSC) and sought to improve its efficiency. By studying the effect of the QD size on the performance of the IBSC, she found that the smaller the quantum dots, the better the efficiency of the solar cell. “The result of this research,” says Alnami, “shows that open circuit voltage decreased as quantum dot height increased.” She found that quantum dots with a size of 3 nm or less work very well to enhance the open circuit voltage of the solar cell device, thereby enhancing the overall performance of the solar cell in converting sun light to electricity.

Najla Alnami says, “these results clearly demonstrates the critical impact quantum dot size has on the performance of IBSCs. This is one step in understanding this new technology and helps to prove that this is a viable new material system. By continuing to study and understand these QD IBSCs, we hope to increase the efficiency closer to the predicted 63% from the mere 18% currently.” Her work is vital to creating the next generation of high efficiency solar cells capable of providing low cost energy. Her work could lead to the world’s power source being revolutionized in a very short time.

Appendix B: Executive Summary of Newly Created Intellectual Property

Understanding the reasons behind quantum dot intermediate band solar cell performance is crucial for additional research and improvements of IBSC efficiency. The following is a list of original intellectual property items that were created in the course of this research project and should be considered from both a patent and commercialization perspective.

1. A method of precisely controlling the quantum dot height in the intermediate band solar cells, called the “capped and annealed truncation technique”, using Molecular Beam Epitaxy.
2. A solar cell structure leading to open circuit voltage preservation in intermediate band solar cells under a non-concentrated system.
3. A quantum dot intermediate band solar cell device with a solar conversion efficiency higher than the reference and significant enhancement of the open circuit voltage, capable of being commercially produced.
4. Characterization and quantification of how quantum dot height affects the performance of the intermediate band solar cell.
5. Characterization of quantum dot intermediate band solar cell efficiencies at variable temperatures (80-300 K).

Appendix C: Potential Patent and Commercialization Aspects of Listed Intellectual Property Items

C.1 Patentability of Intellectual Property

The study of the role of quantum dot size on the performance of IBSCs in this thesis is considered a fundamental study to understand the reasons behind the QD IBSCs performance degradation of previous IBSC research. However, since there are devices presented in this research project created to understand the physical reason behind the degradation or enhancement of IBSCs, the following items are listed on the prospect of patentability.

- 1. A method of precisely controlling the quantum dot height in the intermediate band solar cells, called the “capped and annealed truncation technique”, using Molecular Beam Epitaxy.** The use of the capping and annealing method has been reported prior to this research. Therefore, the method of the quantum dot capped and annealed cannot be patented. However, no one precisely used the cap and anneal method to control the size of the quantum dots in a system of IBSCs. Therefore, it could be argued that the proof of open circuit voltage preservation and efficiency increase in these IBSCs resulting from using this method is patentable.
- 2. A solar cell structure leading to open circuit voltage preservation in intermediate band solar cells under a non-concentrated system.** The IBSC solar cell structure with capped quantum dots with a size of 2 to 3 nm have not been tested in prior research. Therefore, the IBSC structure with quantum dots of 2-4nm, created by the methods described in this research, could be patented.

C.2 Commercialization Prospects

The new technologies created in this research were then considered from the perspective of whether or not the item should be commercialized:

First, this method of capped and annealed QDs in IBSCs should be pursued for a patent. This method of controlling the quantum dot height has shown a preservation of the open circuit voltage and an increase in efficiency, it can be implemented immediately in commercially produced InGaAs-based solar cells created using MBE and MOCVD. This method could be extended to other common solar cell materials, such as InGaP, InGaN, CdS, etc., but requires further research into the viability of this idea in different materials.

C.3 Possible Prior Disclosure of IP

Prior disclosure of the intellectual property of this research has been discussed in public, including but not limited to two conferences and several meetings, and the results will be submitted to an Applied Physics journal. The first conference was in the Summer of 2013 at the VICTER Conference in Little Rock, Arkansas. The second conference was in the Spring of 2014 in Hot Springs, Arkansas.

Appendix D: Broader Impact of Research

D.1 Applicability of Research Methods to Other Problems











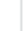



















The methods used in this research can be practically applied to solar cell growth and characterization studies for most material systems. The quantum dot truncation growth technique can be used for most p-i-n-based semiconductor device structures. Additionally, the creation of an intermediate band composed of quantum dots could be beneficial in other p-i-n devices, such as photo-detectors or light-emitting diodes. The structural and optical characterization methods used in this research are commonly used in most semiconductor material systems. The electrical, efficiency-conversion, and external efficiency measurements are commonly used to characterize the performance of most solar cell devices, as well as other semiconductor devices.

D.2 Impact of Research Results on U.S. and Global Society

The result of this research can lead to a significant increase in the efficiency solar cells. For that reason, investigating the reason for efficiency degradation of QD intermediate band solar cells and improving solar cell performance can meet the desired quality for space applications, which is considered essential for the solar community.

D.3 Impact of Research Results on the Environment

The materials used in this research have no harmful impact on the environment other than the byproducts produced by the fabrication procedure of solar cell devices and the energy consumed in creating and measuring the devices.

		Start									
		January		July		January		July		January	
		M	B	E	M	B	E	M	B	E	M
71	 Task Mode 										
	L-F noise measurement equipment										
72	Preamplifier										
73	Noise Analyzer										
74	K-20 Temperature Controller										
75	Adjustable Resistor										
76	2.2 kilo ohm resistor										
77	Battery- 120										
78	Material Characterization										
79	AFM (Atomic Force Microscopy)										
80	PL (Photoluminescence)										
81	Electrical Characterization										
82	Solar cell Efficiency										
83	Current-Voltage (D,L, and T)										
84	Q Efficiency noise Characterization										
85	DLTS (Deep Level Transient Spectroscopy)										
86	External Quantum Efficiency										
87	Analytical equipment identification:										
88	Molecular-Beam Epitaxy										
89	Atomic Force Microscopy										
90	Transmission Electron Microscopy										
91	Photo Lithography, Wet Etching, and Metalization										
92	Photoluminescence										
93	External Quantum Efficiency										
94	Efficiency-Conversion										
95	Current-Voltage characterization										
96	Helium cryostats										
97	LOW-Frequency Noise Measurement										
98	electric characterization										

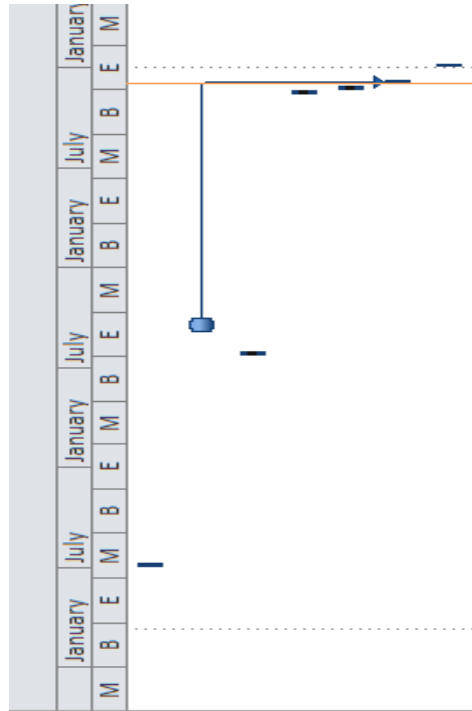
		Task Mode	Task Name	Start	January	July	January	July	January	July	January	July		
					M	B	E	M	B	E	M	B	E	M
133	✓		Solar cell Efficiency Measurement	Tue 2/12/13										
134	✓		Solar Cell Efficiency Measurement at Variable Temp	Thu 3/21/13										
135	✓		I-V Measurement at 300 k - Plotting Data	Wed 2/13/13										
136	✓		I-V Measurement at Variable T - Plotting Data	Thu 3/14/13										
137	✓		EXPERIMENT - SE 4 (SE041)	Mon 4/1/13										
138	✓		ProcessNG Sample	Mon 4/1/13										
139	✓		I-V Measurement at 300 k - Plotting Data	Wed 4/3/13										
140	✓		EXPERIMENT - SE 5 (SF084)(7nm QDs)	Fri 4/5/13										
141	✓		Process Sample (Diode, Solar, and Ring Structures)	Mon 5/13/13										
142	✓		Solar Cell Efficiency Measurement	Fri 4/5/13										
143	✓		Solar Cell Efficiency Measurement at Variable Temp	Mon 4/8/13										
144	✓		I-V Measurement at 300 k - Plotting Data	Wed 5/15/13										
145	✓		I-V Measurement at Variable T - Plotting Data	Fri 5/17/13										
146	✓		EQE Measurement at Room Temp	Fri 4/5/13										
147	✓		EQE Measurement at Room Temp at Variable Temp	Thu 5/23/13										
148	✓		EXPERIMENT - SE 6 (SF085)(5nm QDs)	Thu 5/23/13										
149	✓		Process Sample (Diode, Solar, and Ring Structures)	Thu 5/23/13										
150	✓		Solar Cell Efficiency Measurement	Thu 5/23/13										
151	✓		Solar Cell Efficiency Measurement at Variable Temp	Fri 5/24/13										
152	✓		I-V Measurement at 300 k - Plotting Data	Mon 5/27/13										
153	✓		I-V Measurement at Variable T - Plotting Data	Wed 5/29/13										
154	✓		EQE Measurement at Room Temp	Thu 5/23/13										
155	✓		EQE Measurement at Room Temp at Variable Temp	Fri 5/24/13										
156	✓		EXPERIMENT - SE 8V(SF086)(3nm QDs)	Fri 5/31/13										
157	✓		Process Sample (Diode, Solar, and Ring Structures)	Tue 6/4/13										
158	✓		Solar Cell Efficiency Measurement	Fri 5/31/13										
159	✓		Solar cell Efficiency Measurement at Variable Temp	Mon 6/3/13										
160	✓		I-V Measurement at 300 k - Plotting Data	Thu 6/6/13										

		January							July							January							July							January						
		M	B	E	M	B	E	M	M	B	E	M	B	E	M	M	B	E	M	B	E	M	M	B	E	M	B	E	M	M	B	E	M	B	E	M
ID	Task Mode	Task Name	Start																																	
161	✓	I-V Measurement at Variable T - Plotting Data	Mon 6/10/13																																	
162	✓	EQE Measurement at Room Temp	Fri 5/31/13																																	
163	✓	EQE Measurement at Room Temp at Variable Temp	Mon 6/3/13																																	
164	✓	EXPERIMENT - SE 7V(SF087)(Reference)	Wed 6/12/13																																	
165	✓	Process Sample (Solar Cell, Ring, and Diode Structure)	Fri 6/14/13																																	
166	✓	Solar Cell Efficiency Measurement	Mon 6/17/13																																	
167	✓	Solar Cell Efficiency Measurement at Variable Temp	Tue 6/18/13																																	
168	✓	I-V Measurement at 300 k - Plotting Data	Wed 6/19/13																																	
169	✓	I-V Measurement at Variable T - Plotting Data	Thu 6/20/13																																	
170	✓	EQE Measurement at Room Temp	Wed 6/12/13																																	
171	✓	EQE Measurement at Room Temp at Variable Temp	Thu 6/13/13																																	
172		EXPERIMENT - SE 7V(SF091)(4nmQDs)	Tue 5/14/13																																	
173	✓	Process Sample (Solar Cell, Ring, and Diode Structure)	Tue 5/14/13																																	
174	✓	Solar Cell Efficiency Measurement	Tue 6/25/13																																	
175	✓	Solar Cell Efficiency Measurement at Variable Temp	Sat 6/1/13																																	
176	✓	I-V Measurement at 300 k - Plotting Data	Thu 6/27/13																																	
177	✓	I-V Measurement at Variable T - Plotting Data	Fri 6/28/13																																	
178	✓	EQE Measurement at Room Temp	Fri 6/21/13																																	
179	✓	EQE Measurement at Room Temp at Variable Temp	Mon 6/24/13																																	
180	✓	EXPERIMENT - SE 10V(SF093)(2nmQDs)	Mon 7/1/13																																	
181	✓	Process Sample (Solar Cell Ring and Diode Structure)	Mon 7/1/13																																	
182	✓	Solar Cell Efficiency Measurement	Tue 7/2/13																																	
183	✓	Solar Cell Efficiency Measurement at Variable Temp	Wed 7/3/13																																	
184	✓	I-V Measurement at 300 k - Plotting Data	Thu 7/4/13																																	
185	✓	I-V Measurement at Variable T - Plotting Data	Fri 7/5/13																																	
186	✓	EQE Measurement at Room Temp	Mon 7/1/13																																	

	Task Mode	Task Name	Start
187		EQE Measurement at Room Temp at Variable Temp	Tue 7/2/13
188		Thesis/Dissertation creation:	Fri 3/9/12
189		Read UARK Thesis Guideline	Mon 12/17/12
190		Write Detailed Outline	Wed 12/26/12
191		Write Abstract	Mon 3/10/14
192		Write Introduction	Thu 3/13/14
193		Write Methods	Mon 3/17/14
194		Write Physics and Theory	Fri 5/30/14
195		Write Results	Mon 6/30/14
196		Write Conclusion	Mon 11/3/14
197		Write Appendices	Wed 11/5/14
198		<input type="checkbox"/> Seminars:	Sat 1/7/12
199		<input type="checkbox"/> Spring 2012	Sat 1/7/12
200		The First Monday Meeting of Feb 2012 (Ben Newton's Group)	Mon 2/6/12
201		The First Monday Meeting of March 2012 (Paul Minor's Group)	Mon 3/5/12
202		The First Monday Meeting of Apr 2012 (Matthew Young's Group)	Mon 4/2/12
203		The First Monday Meeting of May 2012 (Vishal Sahore's Group)	Mon 5/7/12
204		First Small Group Meeting of Spring 2012 Matthew Young	Sat 1/7/12
205		Second Small Group Meeting of Spring 2012 Matthew Young	Wed 1/25/12
206		Third Small Group Meeting of Spring 2012 Matthew Young	Wed 4/25/12
207		Fourth Group Meeting of Spring 2012 Mathew Young	Thu 4/26/12

		Task Mode	Task Name	Start
208	✓		Fall 2012	Sat 9/1/12
209	✓		First Monday of September Meeting 2012	Sat 9/1/12
210	✓		First Monday of October Meeting 2012	Mon 10/1/12
211	✓		First Monday November Meeting 2012	Mon 11/5/12
212	✓		First Monday December Meeting 2012	Mon 12/3/12
213	✓		First Small Group Meeting of Fall 2012	Fri 9/14/12
214	✓		Second Small Group Meeting of Fall 2012	Fri 9/28/12
215	✓		Third Small Group Meeting of Fall 2012	Fri 10/12/12
216	✓		Fourth Small Group Meeting of Fall 2012	Fri 10/26/12
217	✓		Fifth Small Group Meeting of Fall 2012	Fri 11/9/12
218	✓		Sixth Small Group Meeting of Fall 2012	Wed 12/5/12
219	✓		Spring 2013	Sat 2/4/12
220	✓		First Monday Meeting in February 2013	Sat 2/4/12
221	✓		Second Monday Meeting in March 2013	Mon 3/5/12
222	✓		Third Monday Meeting in April 2013	Mon 4/2/12
223	✓		Fourth Monday Meeting in May 2013	Mon 5/7/12
224	✓		First Small Group Meeting	Wed 2/8/12
225	✓		Second Small Group Meeting	Fri 4/13/12
226	✓		Third Small Group Meeting	Thu 3/1/12
227	✓		Fourth Small Group Meeting	Fri 3/2/12
228	✓		Fifth Small Group Meeting	Mon 3/5/12
229	✓		Sixth Small Group Meeting	Tue 3/6/12
230			Dr. Salamo's Group Meeting	Tue 3/13/12
328	✓		Presenting about Hall Effect	Thu 5/3/12
329	✓		Presenting about How to Measure Hall Effect	Thu 6/7/12
330			Individual meeting with Pro, Salamo once a week	Mon 7/2/12

		Task Mode	Task Name	Start
330			Individual meeting with Pro, Salamo once a week	Mon 7/2/12
331			Publication and presentation of results:	Mon 9/2/13
332			Presenting at VICTER Conference in Little Rock, AR	Wed 7/24/13
333			Thesis Public Presentation	Fri 11/14/14
334			Defense	Fri 11/21/14
335			Deliver all materials to Grad School	Tue 12/2/14
336			Saudi Arabia arrests me for taking too long	Wed 12/31/14



Appendix F: Identification of All Software Used in Research and Thesis Generation

Computer #1:

Model Number: Dell Latitude E6520

Serial Number: 3THSBS1

Location: Nano Building (Innovation Lab, Room 112), University of Arkansas

Purchased by: Microelectronics-Photonics, University of Arkansas

Computer #2:

Model Number: Dell Optiplex Gn

Serial Number: DRXMS

Location: Nano Building (Electrical Characterization Lab), University of Arkansas

Purchased by: Dr. Gregory Salamo

Computer #3:

Model Number: GARWAY 2000,INC, LPMIN-TOWER

Serial Number: 0009936078

Location: Nano Building (Electrical Characterization Lab), University of Arkansas

Purchased by: Dr. Gregory Salamo

Computer #4:

Model Number: Dell Dimension 8400

Serial Number: 11PXM51

Location: Nano Building (Electrical Characterization Lab), University of Arkansas

Purchased by: Dr. Gregory Salamo

Computer #5:

Model Number: Dell Dimension C521

Serial Number: 52DHPC1

Location: Physics building (Nano-Fabrication Lab), University of Arkansas

Purchased by: Dr. Gregory Salamo

Computer #6:

Model Number: Dell Dimension 8400

Serial Number: X1060256

Location: Nano building (Optical Characterization Lab), University of Arkansas

Purchased by: Dr. Gregory Salamo

Software #1:

Name: Metrics

Purchased by: Dr. Gregory Salamo

Software #2:

Name: K-20 Temperature Controller

Purchased by: Dr. Gregory Salamo

Software #3:

Name: Origin Pro 8.0.6.3.988 SR6

Purchased by: Dr. Gregory Salamo

Software #4:

Name: Microsoft Office 2010

Version: 14.0.7128.5000 (32-bit)

Product ID: 02260-018-0000106-48586

Purchased by: Microelectronics-Photonics, University of Arkansas

Software #5:

Name: MS Project

Purchased by: Micro EP

Software #6:

Name: Digital MicroGraph

Purchased by: Dr. Gregory Salamo

Software #7:

Name: WinSpec/32

Purchased by: Gregory Salamo

Software #8:

Name: Photoshop 13

Purchased by: Mourad Benamara

Software #9:

Name: ImageJ

Purchased by: Free

Appendix G: All Publications Published, Submitted and Planned

Vas. P. Kunets, N. A. Alnami, M. E. Ware, X. Hu, Y. Hirono, C. S. Furrow, V. G. Dorogan, M. Benamara, Yu. I. Mazur, M. Mortazavi, and G. J. Salamo, Dependence of Open Circuit Voltage on Quantum Dot Size in Quantum Dot Solar Cells, Appl. Phys. Lett. (2014). *pending submission